Pontifícia Universidade Católica
do Rio de Janeiro

Tiago de Magalhães Correia

Analytical solution for the propagation of guided acoustic waves in multilayered cylinders applied to through-tubing cement bond logging in oil wells

Dissertação de Mestrado

Dissertation presented to the Programa de Pós-graduação em Engenharia Mecânica of PUC-Rio in partial fulfillment of the requirements for the degree of Mestre em Engenharia Mecânica.

Advisor: Prof. Arthur Martins Barbosa Braga
Co-advisor: Prof. Alan Conci Kubrusly

Rio de Janeiro
June 2020

Pontifícia Universidade Católica
do Rio de Janeiro

Tiago de Magalhães Correia

Analytical solution for the propagation of guided acoustic waves in multilayered cylinders applied to through-tubing cement bond logging in oil wells

Dissertation presented to the Programa de Pós-Graduação em Engenharia Mecânica of PUC-Rio in partial fulfillment of the requirements for the degree of Mestre em Engenharia Mecânica. Approved by the Examination Committee.

Prof. Arthur Martins Barbosa Braga
Advisor
Departamento de Engenharia Mecânica – PUC-Rio

Prof. Alan Conci Kubrusly
Co-advisor
Centro de Estudos em Telecomunicações (CETUC) – PUC-Rio

Prof. Helon Vicente Hultmann Ayala
Departamento de Engenharia Mecânica – PUC-Rio

Prof. Julio Cezar Adamowski
Departamento de Engenharia Mecatrônica – EPUSP

Dr. Roberth Wado Angulo Llerena
Ouro Negro

Rio de Janeiro, June 25th, 2020

Tiago de Magalhães Correia

The author graduated in Mechanical Engineering from Pontifícia Universidade Católica do Rio de Janeiro in 2017.

Bibliographic data

Correia, Tiago de Magalhães

Analytical solution for the propagation of guided acoustic waves in multilayered cylinders applied to through-tubing cement bond logging in oil wells / Tiago de Magalhães Correia ; advisor: Arthur Martins Barbosa Braga ; co-advisor: Alan Conci Kubrusly. – 2020.
118 f. : il. color. ; 30 cm

Dissertação (mestrado) – Pontifícia Universidade Católica do Rio de Janeiro, Departamento de Engenharia Mecânica, 2020.
Inclui bibliografia

1. Engenharia Mecânica – Teses. 2. Guided Acoustic Waves. 3. Cement Bond Logging. 4. Through-Tubing Acoustic Logging. I. Braga, Arthur Martins Barbosa. II. Kubrusly, Alan Conci. III. Pontifícia Universidade Católica do Rio de Janeiro. Departamento de Engenharia Mecânica. IV. Título.

CDD: 621

Acknowledgments

I would like to express my special thanks of gratitude to my adviser, Prof. Arthur Martins Barbosa Braga for the support provided during these years, for the incentive and opportunity.

To my Co-Adviser, Prof. Alan Conci Kubrusly for dedication, patience and attention in recent years.

To CAPES for the financial assistance granted, without which this work could not be carried out.

To REPSOL for investments in the research.

To Prof. Helon Vicente Hultmann Ayala for support and assistance in the search patents and articles.

To LSFO simulation team: Luis Paulo Brasil, Juan Andrés Hidalgo, Mateus Gheorge e Isabel Camerini for their advices and friendship.

To PUC and all employees of LSFO.

And a special thanks to my family for their understanding and support to date. Being them fundamental to this achievement in my life.

This study was financed in part by the Coordenação de Aperfeiçoamento de Pessoal de Nível Superior – Brasil (CAPES) - Finance Code 001

Abstract

Correia, Tiago de Magalhães; Braga, Arthur Martins Barbosa (Advisor); Kubrusly, Alan Conci (Co-Advisor). **Analytical solution for the propagation of guided acoustic waves in multilayered cylinders applied to through-tubing cement bond logging in oil wells.** Rio de Janeiro, 2020. 118p. Dissertação de Mestrado — Departamento de Engenharia Mecânica, Pontifícia Universidade Católica do Rio de Janeiro.

In oil wells, a good cementation is essential to guarantee the structural support of the casing and isolate the well from groundwater. The variations in the material properties and the presence of defects in the cement can lead to leaks and environmental damage. During the deactivation and abandonment of the well in P&A operations (Plug & Abandonment), it is necessary to evaluate the cement condition as well as investigate possible defects.

Since 50's, cement bond logging tools capable of analyzing the cement condition have been developed and improved. The most famous tools were Cement Bond Logging Tools (CBT), based on CBL (Cement Bond Logging) and VDL (Variable Density Logging) operation technique and the Cement Evaluation Tools (CET). However, these tools were designed to operate only in single-casing set, without the tubing. Remove the tubing is an expensive process, so a challenge in the industry that remains open is the creation of a tool capable of operating in wells with tubing in order to reduce process costs or in wells that have multiple casings.

In recent years, many patents and scientific paper have been published on the same topic. This work analyzes the effectiveness of the use of guided ultrasonic waves in multilayer wells to detect defects present in the cement layer. To this end, a vast bibliographic search was first carried out in order to identify the most frequent types of existing defects, the principle of operation of the main commercial tools and the advances in research on this subject.

The well studied was modelled from analytical equations of the elastic wave theory, aiming at the dispersion equations that govern the problem. An analytical-numerical code was developed capable of solving these equations and obtaining the dispersion curves.

Furthermore, it was analyzed how the defects and their variations affect the dispersion curves, identifying the characteristic behaviours for each case. Subsequently, the energy distribution, obtained by the Poynting vector, in the well was used in order to investigate the modes that concentrate the energy in the cement layer. For the single-casing, it was concluded that the best excitation modes were those with high frequency, because the energy is concentrated in cement. For through-tubing case, it was found that at a frequency of 30.13 kHz and a slowness of 726.5 us/m, the energy is virtually completely concentrated in cement, which is interesting to analyze defects present only in cement layer and that at 39.17 kHz and 507 us/m the energy is distributed between cement and tubing, being interesting to analyze defects that involve both layers.

Keywords

Guided Acoustic Waves; Cement Bond Logging; Through-Tubing Acoustic Logging.

Resumo

Correia, Tiago de Magalhães; Braga, Arthur Martins Barbosa; Kubrusly, Alan Conci. **Solução analítica para a propagação de ondas guiadas em cilindros com múltiplas camadas aplicada à perfilagem do cimento através da coluna de produção em poços de petróleo.** Rio de Janeiro, 2020. 118p. Dissertação de Mestrado — Departamento de Engenharia Mecânica, Pontifícia Universidade Católica do Rio de Janeiro.

Em poços de petróleo, uma boa cimentação é fundamental para garantir o suporte estrutural do revestimento e isolar o poço de águas subterrâneas. A alteração das propriedades e o surgimento de defeitos no cimento podem levar a vazamentos e danos ambientais. Durante a desativação e o abandono do poço em operações conhecidas como P&A (Plug & Abandonment), é necessário avaliar a condição do cimento assim como a identificação de possíveis defeitos.

Desde 1950, ferramentas de perfilagem acústica capazes de analisar a condição do cimento vem sendo desenvolvidas e aprimoradas. As ferramentas mais famosas foram a “Cement Bond logging Tools” (CBT), baseada na técnica de operação CBL (Cement Bond Logging) e VDL (Variable Density Logging), e a “Cement Evaluation Tools” (CET). Contudo, essas ferramentas foram projetadas para operar somente em configurações com um único revestimento e sem a coluna de produção. Remover a coluna de produção é um processo caro, por isso, um desafio na indústria que permanece até os dias atuais é a criação de uma ferramenta capaz de operar em poços sem a necessidade de se remover a coluna de produção visando a redução dos custos do processo, ou em poços que possuem múltiplos revestimentos.

Nos últimos anos muitas patentes e artigos tem sido publicados abordando esse mesmo tema. Este trabalho possui como motivação analisar a eficiência da utilização de ondas ultrassônicas guiadas em poços com multicamadas para detecção de defeitos presentes na camada de cimento. Para isso, primeiramente se realizou uma vasta pesquisa bibliográfica buscando identificar os tipos mais frequentes de defeitos existentes, o princípio de funcionamento das principais ferramentas comerciais existentes e os avanços das pesquisas na fronteira do conhecimento desse assunto.

Modelou-se a partir da teoria de ondas e de suas equações analíticas o poço estudado, encontrando as equações de dispersão que regem o problema. Desenvolveu-se um código analítico-numérico capaz de resolver essas equações e de obter as curvas de dispersão.

Além disso, analisou-se como os defeitos e suas variações afetam as curvas de dispersão, identificando os comportamentos característicos para cada caso. Posteriormente, a distribuição da energia, obtida a partir do vetor de Poynting no poço, foi usado afim de se investigar os modos que concentram a energia na camada de cimento. Para o caso sem a coluna de produção, concluiu-

se que os melhores modos de excitação estão em alta frequência, pois a energia se concentra no cimento. Já para o caso com a coluna de produção, encontrou-se que na frequência de 30,13 kHz a uma vagarosidade de 726,5 us/m a energia está praticamente toda concentrada no cimento o que é interessante para se analisar defeitos apenas no cimento e que em 39,17 kHz e 507 us/m a energia está distribuída entre o cimento e a coluna de produção, sendo interessante para analisar defeitos que envolvam ambos.

Palavras-chave

Ondas Acústicas Guiadas; Perfilagem Acústica do Cimento; Perfilagem Acústica Através da Coluna de Produção.

Table of contents

1 Introduction 17
1.1 Contribution for the scientific community 19
1.2 Organization of the thesis 19

2 State of the Art Review 20
2.1 Background on Cement Integrity Logging 20
2.1.1 Cement Bond Logging (CBL) 22
2.1.2 Variable Density Logging (VDL) 23
2.1.3 Transit Time (TT) 25
2.1.4 Cement Evaluation Tools (CET) 25
2.1.5 Multi-strings Cement Bond Logging 26
2.2 Typical Cement Bonding Defects 31
2.2.1 Microannulus 32
2.2.2 Free Pipe 33
2.2.3 Inner and Outer Debonding 33
2.2.4 Casing Eccentricity 34
2.2.5 Tubing Eccentricity 34
2.2.6 Cement Channeling 35
2.2.7 Tool Eccentricity 36
2.2.8 Low Impedance Cement 36
2.3 Stoneley (ST), Scholte and Rayleigh waves 37

3 Analytical Modeling Methods 38
3.1 Analytical solution of the problem of guided waves propagation in cylindrical layers 38
3.1.1 Linear Elastodynamics 38
3.1.2 Strain and Stress Fields 45
3.1.3 Superficial Impedance of a Cylindrical Layer 51
3.1.4 Solid/Fluid Interface on the Internal Surface 54
3.1.5 Superficial Impedance of a Multilayer Cylinder 59
3.1.5.1 Elastic Solid Layers 60
3.1.5.2 Acoustic Fluid Layers 61
3.1.6 Dispersion Equations 63
3.1.6.1 External Medium Composed of Elastic Solid 63
3.1.6.2 External Medium Composed of Acoustic Fluid 65
3.1.7 Determination of Displacement and Stress Vectors 67
3.2 Circumferential Modes 68
3.3 Power Flow (Poynting Vector) 69
3.4 Group Velocity 69

4 Algorithm for the General Case 72
4.1 Input Data 73

4.2 Inner Superficial Impedance Tensor G_0 74
4.3 Superficial Impedance Tensor for the Cylindrical Multilayer G_n 75
4.4 Determination of Dispersion Curves 76
4.5 Power Flux Algorithm 77

5 Results 79
5.1 Validation Cases 79
5.2 Well Configuration 84
5.3 Case Studies: Description 85
5.3.1 Non-Defective Cement 86
5.3.2 Channeling (CH) 86
5.3.3 Cement Quality (CQ) 87
5.3.4 Inner/Outer Debonding (SC/CR) 88
5.4 Results 88
5.4.1 Case 1: Non-Defective Cement 89
5.4.1.1 Single Casing (No Tubing) 89
5.4.1.2 Through-Tubing 90
5.4.2 Case 2: Channeling (CH) 91
5.4.2.1 CH - Single Casing (No Tubing) 91
5.4.2.2 CH – Through-Tubing 92
5.4.3 Case 3: Low Quality (Degraded) Cement (CQ) 93
5.4.3.1 CQ – Single-Casing (No Tubing) 93
5.4.3.2 CQ – Through-Tubing 94
5.4.4 Case 4a: Inner Debonding (SC) 94
5.4.4.1 SC – Single-Casing (No Tubing) 95
5.4.4.2 SC – Through-Tubing 95
5.4.5 Case 4b: Outer Debonding (CR) 96
5.4.5.1 CR – Single-Casing (No Tubing) 96
5.4.5.2 CR – Through-Tubing 97
5.4.6 Axial Power Flow Density Distribution 97
5.4.6.1 Power Flow – Single-Casing (No Tubing) 97
5.4.6.2 Power Flow – Through-Tubing 102

6 Conclusion 107
6.1 Future works 108

7 Bibliography 110

8 Appendix A 117

9 Appendix B 118

List of Figures

1.1 Oil well structure with each layer is indicated. The blue color represents the inner mud present in the well. 17

2.1 The transducer emitting the acoustic signal. The first signal received is the one that is reflected in casing interface. In each layer the transmitted signal reverberates and transmits this information to transducer. 21
2.2 Cement bond logging with the pulse-echo technique. The blue area represents the mud inside the well, the casing indicated is composed by a metal pipe and the formation is composed basically by rocks. 21
2.3 Pitch-catch technique for cement bong Logging. The transmitter (T) generates an acoustic wave that interacts with the interfaces producing a guided wave propagating along the cylindrical layers (casing-cement-formation) and leaks energy into the fluid-filled wellbore. The receivers (R) catch the leaked acoustic signals which are dependent on the characteristics of the layers' interfaces. 22
2.4 Representation of the signal that propagate though the casing in an oil well. 23
2.5 The figure present the full signal obtained. Each part of this signal is a signal that propagate though a different layer as indicated. 24
2.6 The first band group of VDL are the signals that propagate though the casing and indicate how good is the cement bond in interface I. The second group indicate the signals that propagate though the cement indicating how good is the bond between cement and formation in interface II. 24
2.7 Well configuration with tubing, casing, cement and the formation layers. 26
2.8 Representation of TIE and FIE echos in a though-tubing well. The blue area represents the mud inside the well, the casing indicated is composed by a metal pipe and the formation is composed basically by rocks 27
2.9 Transverse cross-section of though-tubing well geometry (Left) and sagittal cross-section with pitch-catch setup (right) (Viggen, et al. 2016). 28
2.10 Representation of Microannulus. The red regions represent the defect. 32
2.11 Representation of Thin Cement Sheath. The blue region represents the defect. 33
2.12 Representation of an Eccentric Casing 34
2.13 Representation of Tubing Eccentricity. 35
2.14 Representation of Channeling. The blue regions represent the defect. 35
2.15 Path of acoustic wave. The distance y between the tool and the coating varies little, but as the tool eccentricity is bigger on the bottom, the distance x varies even more. 36
2.16 Representation of interface waves. One can observe the type of interface waves between the respective media. The maximum energy is concentrated at the interface and decay exponentially. 37

3.1 Coordinate System in a Hollow Cylindrical Layer 36

3.2 Homogeneous and isotropic cylindrical body with internal and external surface characterized by impedance tensors $G0$ e $G1$, respectively. 52
3.3 Elastic cylindrical body with internal surface in contact with acoustic fluid 55
3.4 Cylindrical body composed of isotropic and homogeneous solid multilayers interspersed with acoustic fluid. 60
3.5 Acoustic fluid layer between solid multilayers. 61
3.6 Cylindrical body with external surface in contact with certain medium 63
3.7 Circumferential distribution for cylindrical harmonics. 68

4.1 Scheme of the numerical approach 72
4.2 Pseudocode used in the numerical program 73

5.1 Representation of the case. A single cylinder layer with a dipole excitation source. 79
5.2 (a) Frequency by dimensionless wavelength obtained using the analytical code proposed in this work, where h is the thickness of the cylindrical layer and λ is the wavelength. (b) Frequency by the dimensionless wavelength obtained in (Braga A. M., 2005) the article. The analytical solution is presented in continuous curves (Braga A. M., 2005). 80
5.3 Representation of the problem involving a sigle cylindrical layer with vacuum outside and water inside for a monopole excitation source. 80
5.4 (a) Phase velocity by frequency obtained by the analytical model proposed in this work. The colored curves represent the body waves velocities in each means presents in the well. (b) Phase velocity by frequency used to validate the analytical model presented in (Li, Jing, Murch, 2017) 81
5.5 Representation of the case involving a single cylindrical layer with vacuum in the inner media, water in the outer media and for a dipole excitation source. 81
5.6 (a) Plot of the dimensionless frequency by the dimensionless wave number obtained by the analytical model developed in this work. Each colored curve is for a given ratio between the outer radius, R, and the thickness, d, of the cylindrical layer. (b) Plot of the dimensionless frequency by the dimensionless wave number used to validate the analytical model (Braga, Barbone, Herrmann, 1990). 82
5.7 Representation of the problem of a single cylindrical layer with water in the inside and outside media for a dipole excitation source. 82
5.8 (a) Slowness curve obtained by the analytical model. The magenta line represents the slowness of the body wave that propagates in water. (b) Slowness curve from literature (Liu, D'Angelo, Sinha, Zeroung, 2017). 83
5.9 Representation of a multiple cylindrical layers case, with vacuum inside and outside. 83
5.10 (a) Frequency by the dimensionless wavelength obtained by the analytical model developed in this work, where h represents the thickness of the inner cylindrical layer. (b) Frequency by the dimensionless wavelength used for model validation The blue lines present the exact solution (Braga A. M., 2005). 84
5.11 Well representation for the case studies. 85
5.12 Non-defective configuration. 86

5.13 Channeling in the cement layer (CH). 87
5.14 Low-quality, degraded, cement layer (CQ). 88
5.15 Inner (SC) and outer (CR) debonding. 88
5.16 Dispersion spectrum of subsonic waves for the single-casing well (no tubing) with non-defective cement: (a) frequency vs. wavenumber; (b) wavelength vs. frequency; (c) phase velocity vs. frequency; and (d) slowness vs. frequency. The blue line represents the P wave velocity in water while the red line represents the shear wave velocity in the outer solid media. 90
5.17 Dispersion spectrum of subsonic waves for the through-tubing configuration with non-defective cement: (a) frequency vs. wavenumber; (b) wavelength vs. frequency; (c) phase velocity vs. frequency; and (d) slowness vs. frequency. 91
5.18 Subsonic, frequency vs. wave number plot obtained by the analytical model for the channeling case (CH) without the tubing. The blue straight line corresponds to the S-wave in the rock formation. 92
5.19 Slowness plots obtained by for the channeling case (CH) without the tubing. (a) Slowness vs. frequency for the channeling defect of thickness 1%, 5% and 10% of the original cement layer. (b) Slowness vs. frequency for the channeling defect of thickness 20%, 40% and 60% of the original cement layer. 92
5.20 Subsonic, frequency vs. wave number plot obtained for the channeling case (CH) in the through-tubing configuration. The blue straight line corresponds to the S-wave in the rock formation. 93
5.21 Slowness plots obtained for the channeling case (CH) with the tubing. (a) Slowness vs. frequency for the channeling defect of thickness 1%, 5% and 10% of the original cement layer. (b) Slowness vs. frequency for the channeling defect of thickness 20%, 40% and 60% of the original cement layer. 93
5.22 Dispersion spectra obtained by the analytical model for the degraded cement case (CQ) in the single-casing (no tubing) configuration: (a) frequency vs. wavenumber; and (b) slowness vs. frequency. 94
5.23 Dispersion spectra obtained by the analytical model for the degraded cement case (CQ) in the through-tubing configuration: (a) frequency vs. wavenumber; and (b) slowness vs. frequency. 94
5.24 Dispersion spectra obtained by the analytical model for the inner debonding (SC) in the single-casing (no tubing) configuration: (a) frequency vs. wavenumber; and (b) slowness vs. frequency. 95
5.25 Dispersion spectra obtained by the analytical model for the inner debonding (SC) in the through-tubing configuration: (a) frequency vs. wavenumber; and (b) slowness vs. frequency. 96
5.26 Dispersion spectra obtained by the analytical model for the outer debonding (CR) in the single-casing (no tubing) configuration: (a) frequency vs. wavenumber; and (b) slowness vs. frequency. 96
5.27 Dispersion spectra obtained by the analytical model for the outer debonding (CR) in the through-tubing configuration: (a) frequency vs. wavenumber; and (b) slowness vs. frequency. 97
5.28 Slowness curves for the single-casing configuration and non-defective cement. The blue, red, and green dots are the guided wave modes for which the radial power flow is presented in the sequence. 98

5.29 Axial power flow density for the modes indicated by the blue dots in the slowness diagram for the single-casing well with non-defective cement (see 5.28). 98
5.30 Axial power flow density for the modes indicated by the red dots in the slowness diagram for the single-casing well with non-defective cement (see Figure 5.28). 98
5.31 Axial power flow density for the modes indicated by the green dots in the slowness diagram for the single-casing well with non-defective cement (see Figure 5.28). 100
5.32 Slowness curves for the through-tubing configuration and non-defective cement. The blue, red, and green dots are the guided wave modes for which the radial power flow is presented in the sequence. 102
5.33 Axial power flow density for the modes indicated by the blue dots in the slowness diagram for the through-tubing well configuration with non-defective cement (see Figure 5.32). 103
5.34 Axial power flow density for the modes indicated by the red dots in the slowness diagram for the through-tubing well configuration with non-defective cement (see Figure 5.32). 104
5.35 Axial power flow density for the modes indicated by the green dots in the slowness diagram for the through-tubing well configuration with non-defective cement (see Figure 5.32). 104

List of Tables

2.1 Summary of principle articles related in the topic of multi-string cement evaluation. 30
2.2 Assignees and total number of their relevant patens in the topic of multi-string cement evaluation. 31

5.1 Reference model of well used in North Sea (Zhang J. 2019) 85
5.2 Acoustic Properties for the case Studies (non-defective cement layer) 85
5.3 Base Geometry for the case Studies (non-defective cement layer) 85
5.4 Simulated defects for single-casing and through-tubing configurations 86
5.5 The axial Power flow distribution for each dot. 101
5.6 The variation of this dots with presence of each defect. 101
5.7 Energy distribution for each point. 105
5.8 The variation of this dots with presence of each defect. 105

Summary of Notations

λ, μ	Lamé Constants
ρ	Density
c_L	Acustic velocity of longitudinal wave
c_T	Acustic velocity of shear wave
u	Displacement
φ, χ, η	Scalar potentials
ψ	Vector potential
u_r	Displacement in radial direction
u_θ	Displacement in circumferential direction
u_z	Displacement in axial direction
t	Stress vector
ϕ	Vector of scalar potential
i	Imaginary Number
ν	Circumferential mode
A, L	Differential matrix operator
Φ	Diagonal matrix with Hankel function elements
c_p	Phase velocity
c_g	Group velocity
k_L	Longitudinal wave number
k_T	Shear wave number

1
Introduction

During the life of an oil well, some properties of the well vary over the time such as pressure and temperature [1] [2]. These factors may cause changes in the properties and conditions of the cement, resulting in leakage of the formation or casing fluids through the cement [2] [3]. The casing is a metal structure used to prevent that fluids in the well leak to the formation. It is fixed in the formation from a cementation that works as a structural support for the well. The tubing is an inner pipe that aims to transport oil to the surface. Figure 1.1 shows a representation of an oil well with each layer indicated.

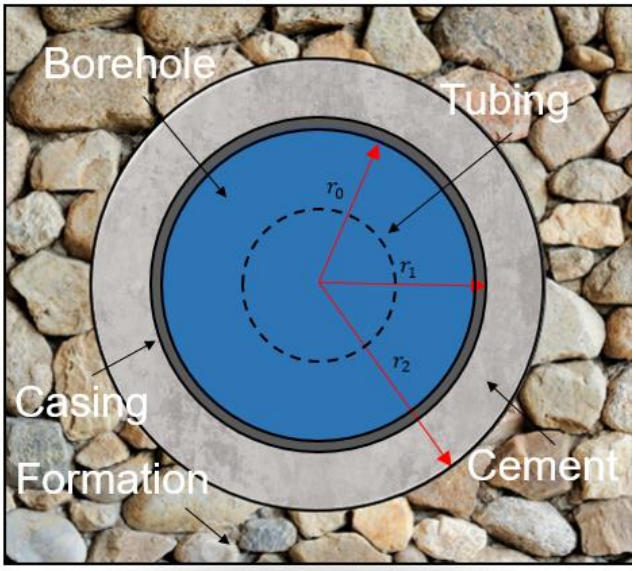

Figure 1.1 – Oil well structure with each layer is indicated. The blue color represents the inner mud present in the well.

At the end of the useful life of a well, it is deactivated. This operation is known as plug and abandonment (P&A) [4]. To ensure that the abandoned well does not cause future risks to the environment, the cement layer must usually go through an inspection process [5].

There are several methods to evaluate the quality of the cement sheath, such as hydraulic tests [6], positive and negative differential pressure tests [6], using temperature data [6], radioactive procedure [6] or through sonic and ultrasonic inspection [6]. Among the cement evaluation methods, the most used is the one based on sonic and ultrasonic inspection because they allow one to evaluate effectively the cementation quality and the possibility of the fluid leakage [7]. Tools

based on this method, known as cement bond log tools, have been developed and refined since the late 1950s [7].

The first tools developed used the cement bond logging (CBL) [8] [9] and the variable density logging (VDL) [7] [9] sonic profiles to directly measure cement quality between the casing and the formation, these tools became known as Cement Bond Logging Tools (CBT) [2] [7]. Conventional CBT tools are not able to inspect a well through the tubing, which has to be removed prior to the inspection [7]. This operation increases the costs of P&A operations [4] [10]. Also since these tools have a lot of limitations, for example in radial scan resolution, new tools started to be developed.

Conventional CBL/VDL tools consist primarily of one transmitter and two receivers located three and five feet from the transmitter [3] [8]. The set also needs centralizers to avoid eccentricity during its operation [1] [3]. Its principle of operation consists of the emission of an acoustic pulse that propagates to the multiple layers of the well and the recording of the propagated signal by the receivers [11] . In the ultrasound jargon, this is called pitch-catch technique [12]. At interfaces in which there is a transition of acoustic impedances, part of the signal reflects reaching the receivers.

Recently, there has been a lot of interest by companies as Schlumberger, Well Guard, REPSOL and Halliburton in the development of a tool capable of analyzing the condition of the Cement layer and identifying possible defects present in through-tubing wells and multiple casing [13] [14] [15]. Also, many techniques and methods involving acoustic waves capable of analyzing defects in a well have been published [16] [17]. However, studies carried out in this area demonstrate how the introduction of another layer (tubing) can hinder this analysis [12] [18] [19] [16]. Recently, the use of the guided waves technique to analyze the cement condition has been studied and good results have been obtained [20] [21] [16] [12].

Elastic guided waves are mechanical stress waves that propagate within structural boundaries of structures such as pipes, with wavelengths that are comparable to the thickness dimension of the waveguide. It is commonly used in rapid testing tools to detect, locate and classify corrosion defects. When using guided waves for non-destructive testing or evaluation applications, the interpretation of the resulting information must be carried out by suitably qualified and experienced engineers working to validate produce.

In this scenario, this thesis investigates an analytical-numerical model that solves the propagation characteristics of the guided waves in a multi-layered cylinder, which can be used to model a wellbore. Additionally, defects were introduced in this model in order to simulate how its presence interferes in the obtained plots. The validation of this model was carried out based on the literature either reporting experimental or theoretical results for similar cases to the one studied in this work.

From the reproduction of the defects and variation of some of their parameters, it was possible to understand how each type of defect influences the dispersion curves and how the guided modes vary with the defect. This identification is carried out observing the changes that occur in dispersion curves from a case without the defect to a case with the defect.

It was also studied which modes concentrates more energy in the cement layer, where defects are located. In these modes there is less energy leakage to the others layers, it makes the variations promoted by defects in dispersion curves more intense.

1.1 Contribution for the scientific community

The main contribution of this thesis for the scientific community are:

1. Develop a numerical code to solve dispersion equations.
2. Comparison of the results present in the literature with those obtained by the code developed.
3. Present analytical dispersion charts for the elastic guided wave propagation in oil wells in order to be used as validation model in numerical simulations.
4. Analyze the variation that defects present in cement can cause in the dispersion curves.
5. Analyze the best guided wave modes and frequency in order to reduce the energy loss and improve the defects identification in cement.
6. Promote an analytical background for building a tool capable to identify possible defects in though tubing oil wells.
7. Based on this thesis, the article *Analytical and numerical modeling of through-tubing acoustic logging* was written for *Rio Oil & Gas 2020* (IBP) conference comparing some of these results with FEM simulation realized [81].

1.2 Organization of the thesis

This dissertation is organized as follow:

Chapter 1 introduces the problem, present the objectives and contribution of this work.

Chapter 2 promotes a review of the main methods used to identify defects in the single casing case and the main conclusions from the literature. This chapter also review the main acoustic techniques used by commercial tools. A deep search was made enumerating the most relevant defects in the cement layer present in literature and patents about analysis of through-tubing wells.

Chapter 3 presents the theory, the equations that govern the problem of elastic guided waves through multiple layered cylinders and their boundary conditions.

Chapter 4 presents a numerical routine developed to solve the dispersion equations found.

Chapter 5 shows the results obtained by the numeric routine applied for the single casing and through tubing scenarios for the main defects found in literature by means of dispersion curves and energy flux charts.

Chapter 6 Concludes this work.

2
State of the Art Review

Plugging & Abandonment (P&A) operations present enormous technical and economic challenges to the oil & gas industry [4]. In order to be permanently abandoned, the well must be hydraulically sealed to isolate the reservoir and other fluid-bearing formations, preventing any spills to the surrounding soil, aquifers, and strata, which could result in potentially large-scale environmental disasters carrying substantial costs to the people and liable parties. The Well Integrity Management System (SGIP) instituted in Brazil by ANP through its Resolution nº46/2016 of November 1st, 2016, establishes the concept of a Barrier Integrated Set (BIS; CSB in Portuguese) as a set of at least one element capable of preventing the unintentional flow of fluids from the formation into the wellbore, into another formation, or to the external environment, covering all possible leaking paths [5] [22]. ANP's SGIP requires that at least two BIS be set in order to permanently abandon a well, and one of the elements in the barriers is the cement-casing interface [5] [22].

An important step in P&A operations is to assess the integrity of the cement bond and its sealing capability. Among typical defects found when evaluating the cement quality are poor bond to pipe, formation, or both, as well as channeled cement, voids, or wet microannulus [23] [24]. Acoustic logging methods based on the propagation of sonic or ultrasonic waves have been extensively applied in the industry to qualify the bond between casing, cement and formation [23] [7] [25] [26] [27].

2.1
Background on Cement Integrity Logging

Of the acoustic logging methods, Cement Bond Logging (CBL) was the first to reach the market in the late nineteen-fifties [8] [9] and still remains one of the most widely employed in the industry. Earlier versions of CBL relied on the pulse-echo technique where a single transducer acts as both transmitter and receiver of acoustic waves [8] (Figure 2.2). A short pulse is emitted by the transducer and converted into acoustic waves — sonic or ultrasonic depending on the frequency — which propagate through the liquid medium reaching the internal wall of the casing. The waves are partially reflected by the metallic wall and transmitted to the casing, cement and formation. Reverberations of the acoustic signals reflected by the interfaces are then picked up by the transducer as can be seen in Figure 2.1 [28] [29] [30] [31] [32] [33].

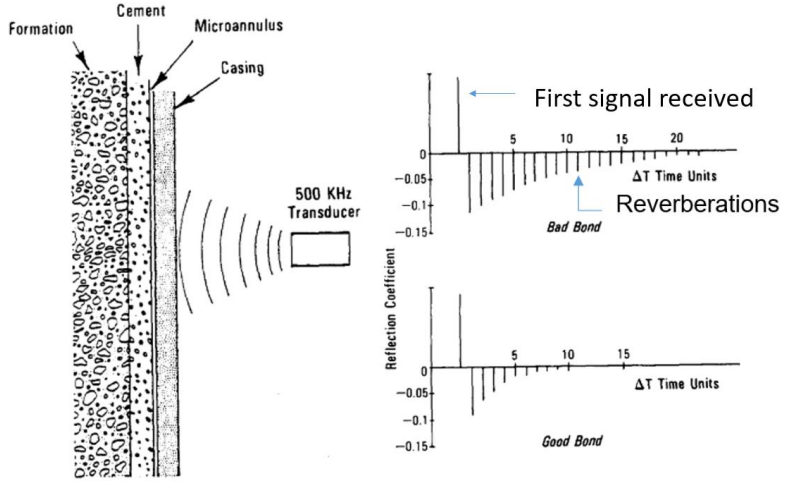

Figure 2.1 – The transducer emitting the acoustic signal. The first signal received is the one that is reflected in casing interface. In each layer the transmitted signal reverberates and transmits this information to transducer.

The rate of reverberation decay can be, in principle, associated with the quality of the bonds between casing, cement and formation [8] [34].The pulse-echo CBL method, despite being extensively employed in the industry, has several limitations. Among them, one may cite a strong dependence on calibration, difficulty to differentiate between low density cements and other fluids with similar acoustic impedances or to assess the cement's quality away from its interface with the casing thus failing, for instance, to detect the presence of internal voids [8].

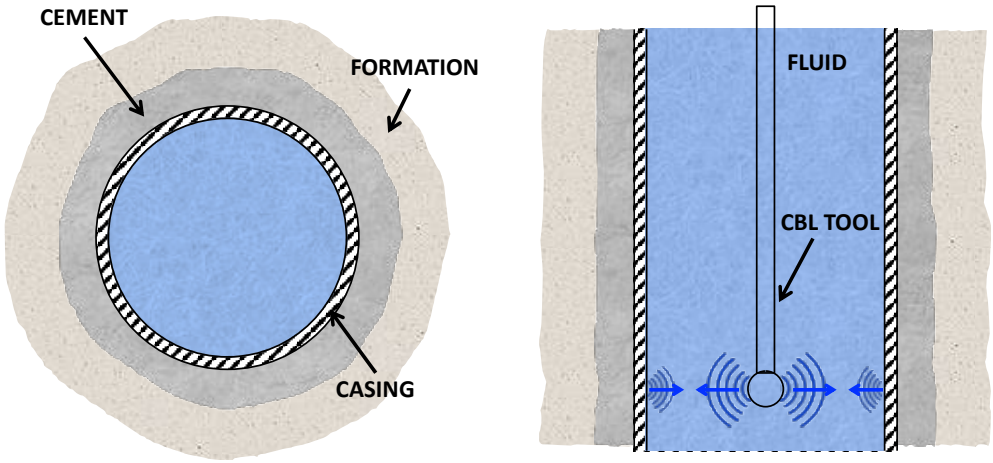

Figure 2.2 - Cement bond logging with the pulse-echo technique. The blue area represents the mud inside the well, the casing indicated is composed by a metal pipe and the formation is composed basically by rocks.

More advanced versions of CBL operate under the pitch-catch principle of guided waves [7] [20] [21] that propagate axially through the multiple cylindrical layers inside the well, namely the fluid-filled wellbore (without the production tubing), the casing, the cement layer and the surrounding rock formation. A typical CBL tool operating in the pitch-catch mode employs one or more transmitters and at least two receivers displaced along its length. The acoustic wave generated by the transmitters inside the fluid-filled wellbore impinges obliquely upon the internal wall of the casing at a defined angle to generate a specific guided mode in the multilayered, cylindrical structure formed by the casing wall, cement layer and rock

formation [11]. The guided wave propagates axially but its energy leaks into the fluid inside the wellbore. This leaky wave mode is detected by the set of receivers disposed along the logging tool. Figure 2.3 schematically illustrates the pitch-catch principle of acoustic logging. The coupling between casing and cement as well as cement and rock formation have an effect on the signals picked up by the receivers, thus providing more detailed information than by the pulse-echo method of earlier CBL versions [25]. The more discernible features of the signal are on the amplitudes of the detected waves [25], which, being related to the loss of energy through the interface, are greatly affected by the quality of the cement as well as by its bond to the casing. Other features are the time of flight and the entire waveform, which supply information regarding the cement density. This type of profile is known as variable density log (VDL) [2] [7].

Currently, the acoustic logging tools are only able to perform successfully in wells without the production tubing and with a single casing string [35] [36] [37]. Consequently, the use of CBL or VDL tools in P&A operations requires prior removal of the tubing string [18], an operation that is costly and time consuming — particularly for subsea wells. But in spite of a great demand, there are presently no acoustic logging tools in the market capable of performing cement integrity evaluation through the tubing string as illustrated in Figure 2.3, or able to inspect wells with multistring casings [38] [39] [40] [41] [42] [43].

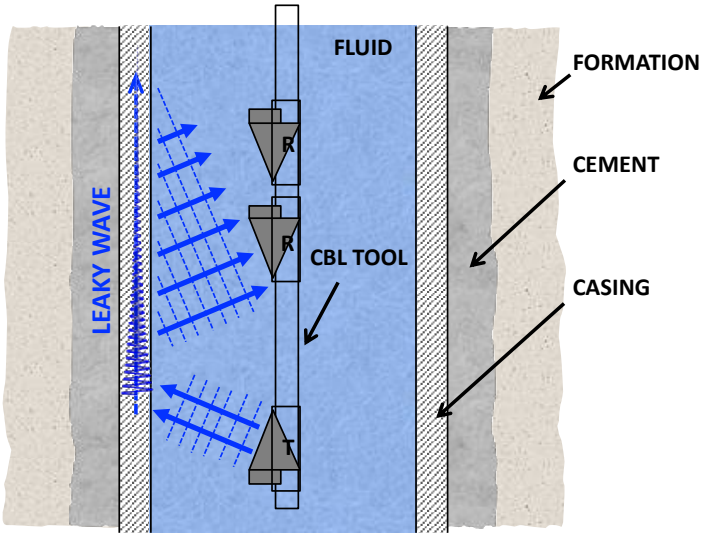

Figure 2.3 - Pitch-catch technique for cement bong Logging. The transmitter (T) generates an acoustic wave that interacts with the interfaces producing a guided wave propagating along the cylindrical layers (casing-cement-formation) and leaks energy into the fluid-filled wellbore. The receivers (R) catch the leaked acoustic signals which are dependent on the characteristics of the layers' interfaces.

2.1.1
Cement Bond Logging (CBL)

CBL is the continuous record of the amplitude, in mV, of the signal that travels through the casing and reaches the receiver located 3 ft from the transmitter as demonstrated in Figure 2.4. The first signal that arrives at the receiver is the one that propagate through the casing, the second is the signal that propagate though the cement and the last is the one that propagate though the fluid.

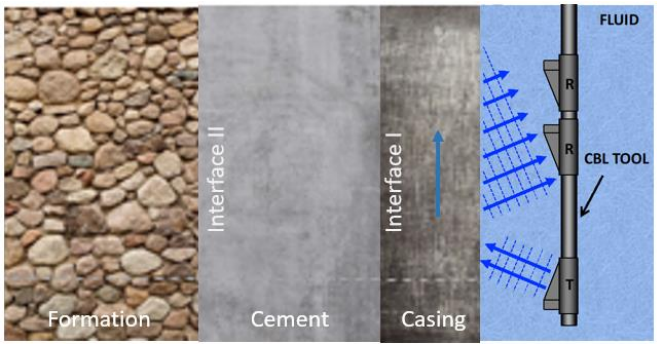

Figure 2.4 – Representation of the signal that propagate though the casing in an oil well.

CBL analysis is based on the principle that if the casing is completely disbonded from cement, a condition known as free pipe [3], the signal received by the receiver will be attenuated because the propagating wave energy of the propagating wave will not leak to the cement and formation. In a less extreme case, where the casing is partially disbonded from the cement, the signal received by the receiver would be more attenuated, but not enough to ensure good bond condition [3].

CBL can rely on the amplitude in mV of the signal received as a reference for cement quality, with amplitudes greater than 10 mV indicative of poor adherence and amplitudes less than 10 mV indicative of good adherence [1] [3].

The CBL can also be used for analysis of the relative amplitude between a zone of interest and a known fully disbonded zone (free pipe) [44]. The calculation of relative amplitude can be seen in Equation (2.1)

$$\text{Relative Amplitude } (l_a) = \frac{\text{Amplitude of studied zone}}{\text{Amplitude of free zone}} \times 100\% \qquad (2.1)$$

The quality of the cement coupling with the casing can be estimated from the calculated parameter l_a. If l_a is less than 20%, there is an indication of good bond. Bad bond is indicated when l_a has values greater than 40%. For intermediate values, there is an acceptable bonding indicative [3].

2.1.2 *Variable Density Logging (VDL)*

The full signal, with its amplitude in mV, is stored by the transducer located five feet from the source. The 5 ft distance is set to obtain better spacing between the waves that propagate in different paths and are received by the transducer [45]. The registration of this full signal is called VDL or microseismogram [45] and allows one to analyze not only the quality of the cement bonding with casing but also the cement with the formation, being essential as it provides a better overall view of the well that CBL. The representation of the VDL is obtained from the oscilloscope conversion of the full signal obtained by receiver in light bands with variable light intensity as a function of the magnitude of its amplitude [1]. Figure 2.5 present the full signal obtained by receiver until 1200 µs from emission.

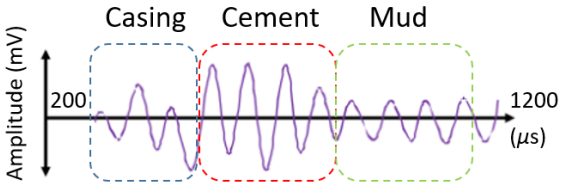

Figure 2.5 – The figure present the full signal obtained. Each part of this signal is a signal that propagate though a different layer as indicated.

While the tools scan the well, a full signal is obtained for each position. So, a conversion is done representing these signals as a function of depth being the light intensity of bands depending on the amplitude of each part of signal. Figure 2.6 represent the VDL signal.

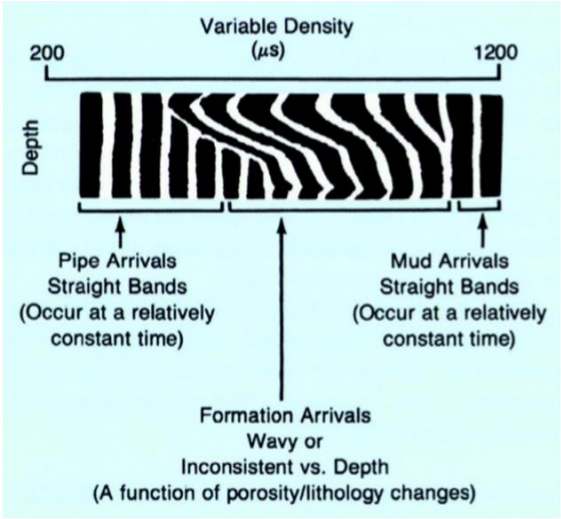

Figure 2.6 – The first band group of VDL are the signals that propagate though the casing and indicate how good is the cement bond in interface I. The second group indicate the signals that propagate though the cement indicating how good is the bond between cement and formation in interface II [15].

The acoustic pulses emitted by the transducer to obtain the CBL/VDL vary from 10 to 60 pulses per second during 50 microseconds and are usually generated with 20 to 30 kHz of frequency, varying with the diameter of the tool used [1] [3] [6]. For large diameters above three inches the frequency of 20 kHz is used and for smaller diameters below two inches the frequency of 30 kHz is used [1].

The first signal to arrive at the transducer is the longitudinal wave that propagates directly through the casing, because the velocity of sound propagation in the steel is higher than in the other media of the well, combined with a shorter distance. Then the wave signals from the formation, the cement and those propagating through the fluid arrive at the receiver. The vast majority of signals reach the receiver until 2000 μs, however it is usually only the range of 200 to 1200 μs is considered sufficient for the complete analysis of the cement condition [6] [44].

2.1.3 Transit Time (TT)

Another parameter used by conventional CBL/VDL tools to ensure signal quality and accuracy is the transit time (TT) [6]. This parameter is basically the time taken to the acoustic signal to travel through the fluid inside the well until the receiver located at 3 ft (0.9144 m).

The main objective of the TT is to verify if the tool is centralized, being an essential information to validate the signals obtained by CBL and VDL [1] [3]. In addition, the transit time helps to confirm which part of signal has propagated through the formation and which part has propagated through the fluid, identifying the fast and slow formation cases.

The fast formation case occurs when the speed of the wave coming from the cement reaches the receiver faster that the signal propagated by the fluid, while slow formation case occurs when the signal that propagates through the fluid arrives first.

To eliminate the possibility of using the arrival time of formation signal instead of the fluid signal during analysis, one uses for comparison values of TT previously calculated for the same well configuration in a case of free pipe, where there are no incoming waves from formation. This allows the signal from the fluid to be properly identified and compared [6]. Deviations greater than 4 μs indicate decentralization, making the CBL/VDL data invalid [6].

Moreover, the conventional tools are also enhanced with mechanisms that help during analysis, help to reduce existing ambiguities. Among them, we can highlight the casing collar locator (CCL) that provides a depth indicator and the gamma ray (GR) that detects formation defects from readings of its radiation [1] [3].

2.1.4 Cement Evaluation Tools (CET)

Conventional CBL/VDL tools have limitations, such as the difficulty of identifying fluid channels inside the cement, a defect known as channeling [15]. This is because the transducers of these tools are omnidirectional, making partial azimuth defects impossible to be identified [8]

To improve the cement quality investigation, Havira et al [8] proposed a tool based on the pulse echo principle. In this tool a transducer positioned perpendicular to the inner wall of the casing transmits and receives the acoustic signal [8]. Cement quality analysis was performed based on the amplitude of the reverberations of the acoustic signal received. If the attenuation of signal reverberations increases, resulting in a greater loss of signal amplitude, better will be the bond between cement and casing.

Although the proposed tool improved the vertical and azimuth resolution compared to conventional tools, it was found that the tool had no information about cement thickness, no information about channeling radial extension, no microannulus influence on interfaces, which resulted in the ineffectiveness of proposed tool.

In order to eliminate the azimuth limitation of conventional tools, Baker Hughes developed the segmented bond tool (SBT) [3]. This type of tool has six to eight pads helically arranged in different azimuths, each one evaluating 45° to 60° of circumference, varying with the diameter of the well. Each pad has a transmitter and a receiver spaced by 1 ft (0.3048 m) and are coupled to the inner surface of the casing. The pads are organized so that the acoustic signal transmitted by each transmitter propagates through the casing and arrive at the respective receiver. The SBT can also operate coupled with a CBL/VDL arrangement, similar to conventional tools, for better analysis of the well conditions.

This type of tool has demonstrated effectiveness in detecting channels, microannulus, cement bond quality and other possible defects. Moreover, this tool has shown many other advantages compared to CBL/VDL conventional tools and the based in pulse echo, such as not being sensitive to variations in fluid density, the presence of gas in fluid, variations in pressure, temperature and the eccentricity of the tool [1] [3] [46] [47] [48].

2.1.5
Multi-strings Cement Bond Logging

Today, CETs are limited to characterization of cement and identification of defects in single-string wells, without the tubing. For this reason, recently, great attention has been drawn to study and analysis of guided wave propagation in multi-strings wells as a way to determine the cement quality and investigate possible defects [12] [17] [18] [49]. Figure 2.7 shows the layout of a through-tubing well.

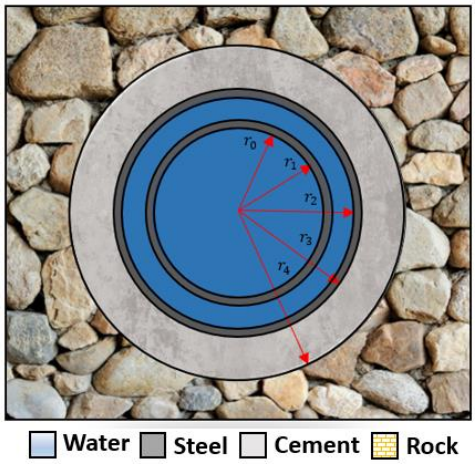

Figure 2.7 - Well configuration with tubing, casing, cement and the formation layers.

Recent studies show the efficiency of using guide wave dispersion curves, more specific the slowness plot, for the different source excitation modes (monopole, dipole, quadrupole) as a way to identify possible well defects [17] [45] [49]. In addition, in recent years, tool and methods capable of analyzing wells with multi strings have been patented and published.

The slowness curves are usually used in literature to represent the acoustic guided-waves modes. The slowness is defined as the inverse of phase velocity,

that is $s = 1/c_p$. The excitation of modes due to their circumferential order (i.e., monopole, dipole, quadrupole) is better explained in Chapter 3.

Investigation on through-tubing acoustic logging techniques is a fairly recent trend [12] [18] [19] [50]. Viggen *et al*. applied the finite element method to numerically simulate the pulse-echo technique when logging a cased wellbore through the production tubing but greatly simplified by resorting to a two-dimensional (plane) model and thus taking out the effects of curvature in the multiple interfaces [18]. In this setting, the first (FIE) and third (TIE) interface echoes were found to be the more relevant ones. The first, FIE, are those associated with interactions of the acoustic pulses with the internal wall of the production tubing which reverberate within the fluid filling the tubing. TIE are associated with reflections at the internal casing wall and reverberations within the fluid in the A-annulus. Figure 2.8 represent the FIE and TIE in a though-tubing well.

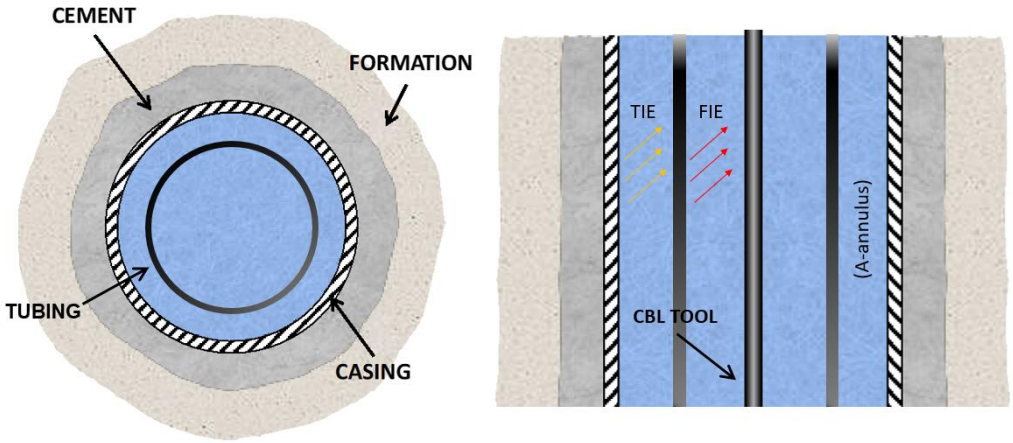

Figure 2.8 –Representation of TIE and FIE echos in a though-tubing well. The blue area represents the mud inside the well, the casing indicated is composed by a metal pipe and the formation is composed basically by rocks

The authors in [18] assumed that the material in the cemented annulus between the casing and formation affects the reverberating echoes present in the TIE acoustic signal, thus allowing, in principle, the assessment of the cement bond quality. They analysed several changes in different parameters such as the thickness of the cement layer as well as its eccentricity and acoustic impedance, the latter ranging from that of a liquid medium to of a rock formation, which are respectively lower and higher than of typical cements. Results presented by Viggen *et al*. have shown, however, that even though TIE are sensitive to the acoustic properties of the material in the cement annulus, between casing and formation, the changes are too weak in order to yield reliable assessments in real cases [18].Their results also demonstrated that annulus eccentricity greatly affects TIE, showing in particular that for severe eccentricities, depending on the azimuth angle of the acoustic transducer, the TIE are almost totally suppressed making the technique of pulse-echo ineffective.

The pitch-catch method shows more promising perspectives for application in through-tubing acoustic logging. Viggen *et al*. also investigated through numerical simulations the generation and propagation of guided, leaky Lamb waves in the production tubing [12]. More precisely, they simulated the application

of the of the pitch-catch technique by exploring the leaky A0 Lamb-like guided wave mode (first-axisymmetric) propagating in the production tubing wall. The wave fronts that leak to the interior of the production tubing in a double-cased well are recorded by two acoustic receivers at 250 and 350 mm away from the transmitter. Differently than for the case of the single casing, the guided Lamb waves leak energy into the tubing and also to the A-annulus. Results of the simulation indicated that trains of Lamb waves are generated in both pipe walls and affected by the boundary conditions in the external wall of the outer casing. Figure 2.9 present the pitch-catch method.

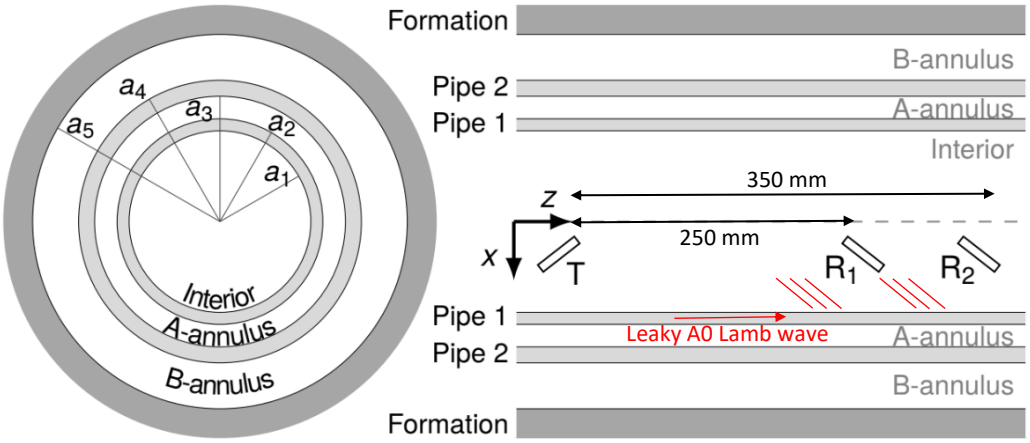

Figure 2.9 – Transverse cross-section of though-tubing well geometry (Left) and sagittal cross-section with pitch-catch setup (right) [12].

By looking into the multiple groups of signals associated with different wave packets, the authors demonstrated that it is possible to assess the material present in the cement layer between the outer casing and the rock formation. However, it must be pointed out that in their simulation they did not consider the curvatures of the interfaces, but rather simplified the geometry by considering a plane, two-dimensional, problem. On the same topic, [19] reported results of experiments conducted in scaled model with plates that partially demonstrated the findings of [12] regarding the generation of guided, leaky Lamb waves in the two walls and the possibility of identifying the wave packets associated with the propagation along the outer wall.

Haldorsen *et al*. [51] established whether sonic data acquired in a cased hole can be used to estimate the material behind a second casing when the annulus between the two sets of casings is fluid-filled. The paper analyses plane waves, and identifies subtle but distinct changes in the waveforms that appear to be dependent on the material filling the outer annulus, allowing for the determination of the fill material. Zeroug *et al.* [52] focuses on low and high frequency ultrasonic measurements techniques that are currently used for cement evaluation. It also presents an understanding of the physics related to the measurements, the development of effective modelling, signal processing and interpretation of methodology. The measurements are performed by guided waves excited in the casing string, which propagate axially along the pipe. Signal processing and interpretation rely on information obtained from dispersion spectrum, as well as

time-of-flight and amplitude variations across receivers, to provide a diagnosis of cement quality and an estimation of the material properties of interest.

Liu *et al.* [49] presents numerical and experimental analysis of the propagated guided waves modes in a geometry composed by two concentrating casing immersed in fluid. The slowness in frequency domain was obtained and analyzed for monopole and dipole sources. Comparisons between experimental and modeled results show excellent agreement for both axisymmetric and asymmetric modes. Liu *et al.* [16] development experimental techniques and a theoretical model to investigates the acoustic guided wave propagation in a borehole composed by two or more casing strings and a cement layer. The article also presents the capacity of guided wave modes to provide diagnostics of the cement condition behind the second casing. For a free and cemented condition, the main slowness differences occur at the Stoneley modes for a monopole excitation. This variation is more sensitive to the cement annulus within the frequency range from 10 to 70 kHz. The maximum slowness variation occurs at 21 kHz. The most evident slowness variation occurs at quadripole mode with the frequency range from 5 to 80 kHz.

Zeroug and Bose [53] reviews a few recent advances in oil and gas applications related to image the earth subsurface hydrocarbon reservoir and to probe rock mechanical properties, spanning measurements concepts and processing and inversion approaches. They focused on the interpretation of a sonic response in a well cased with double steel strings cement to rock formation for evaluating the integrity of the cement. Machine learning algorithms were employed on experimental datasets to develop diagnostic techniques for the cement condition

Liu and Choi [54] analyzed, from experiments and analytical models, several excited guided wave modes that propagate in complex structures involving two casing and eccentricity. It presented four degrees of freedom that control the eccentricity of the double strings and analyzed the influence of inner casing eccentricity in slowness curves. They concluded that Stoneley mode becomes faster with increasing eccentricity of the casing and the most evident slowness variations occur at the frequency range from around 2 kHz to 12 kHz.

Liu and Choi [17] described an experimental study to characterize the sonic response in conjunction with a theoretical modeling. The modeling approach was developed to predict the guided modal characteristics of axially-propagating waves in concentric and non-concentric cylindrical structures immersed in fluid. Experimental investigation was conducted regarding the acoustic features associated with various cement damages.

Zhang et al. [10] describes a novel methodology and an associated logging apparatus, leading to a new technique that can evaluate cement bond or isolation around the casing through the production tubing. The acoustic energy emitted and received by a logging tool inside the production tubing travels through tubing and the surrounding annulus to determine the attenuation caused by the material behind the outer casing. They concluded that the low-amplitude bonding signal, overwhelmed by the dominating signal from the tubing wall, is successfully identified through a unique frequency domain signal processing. Field tests demonstrated that the proposed multi-string logging technology is applicable to all

typical casing and tubing weight or size combinations and provides quantitative assessments on isolation conditions of wells through the production tubing.

Table 2.1 highlights the most relevant information in the reviewed articles.

Table 2.1 – Summary of principle articles related in the topic of multi-string cement evaluation.

Article	Summary
Haldorsen et al. (2016) [51]	The paper analyzes plane waves and identify subtle but distinct changes in the waveforms that appear to be dependent on the material filling the outer annulus, allowing for the determination of the fill material
Viggen et al. (2016a) [12]	Presents a 2D FEM simulation realized in COMSOL using the pulse-echo technique in two deferens models. One that involves two casing and a formation and another without outer casing and the formation
Viggen et al. (2016b) [18]	The paper present a finite elements simulation with commercial software in the time domain using the pitch-catch method to analyze the second received signal (TIE)
Zeroug et al. (2016) [52]	Cement evaluation throw sonic and ultrasonic measurements
Liu et al. (2017a) [49]	Numerical and experimental analysis of the propagated guided waves modes in a geometry composed by two concentrating casing immersed in fluid.
Liu et al. (2017b) [16]	Diagnosis of the cement condition behind the second casing
Zeroug and Bose (2018) [53]	Interpretation of a sonic response for evaluating the integrity of the cement. Machine learning are employed with training on simulated and experimental datasets to develop cement diagnosis
Liu et al. (2018) [54]	This paper analyzes from experiments and analytical models several excited guided waves that propagate in complex structures involving two casing and eccentricity
Liu et al. (2019) [17]	Theoretical modelling of propagating waves in a non-concentric cylindrical structure immersed in fluid
Zhang et al. (2019) [10]	Novel methodology and an associated logging apparatus, leading to a new technique that can evaluate cement bond or isolation

As for the scientific and technical literature, recent patent trends are also indicates that there is a current and growing trend to employ the concept of guided waves in the cased wellbore to improve acoustic logging techniques, particularly for inspecting the quality or integrity of the cement sheath without removing the production tubing. Patent applications (US Patent No. 15/575,168, 2015), (US Patent No. 15/575,108, 2016), (US Patent No. 15/575,024, 2015), (WIPO Patent No. WO2019084219A1, 2018), (WIPO Patent No. 2017048862A1, 2015), and (US Patent No. 16/258,070, 2018), all rely on the dispersion spectrum of guided waves propagating in the multistring wellbore. The first four of these applications are assigned to Schlumberger, the other two to Halliburton and Wellguard, respectively. In a few of these patent applications, one may also highlight the proposed use of machine learning techniques to improve the interpretation of the data generated by through-tubing, acoustic logging tools.

Table 2.2 summarizes which companies were assigned the more relevant patents founded in the intellectual property search related to this topic.

Table 2.2 – Assignees and total number of their relevant patens in the topic of multi-string cement evaluation.

Assignee	Patent no.	Summary
Schlumberger Technology Corporation	WO2016 187 239A1 [55]	Proposed tool: Sonic Scanner Sclumberger Measured dispersion and slowness data are matched to a database to quantify the shear modulus of the cement.
Schlumberger Technology Corporation	WO2016 187 240A1 [56]	Proposed tool: Isolation Scanner Sclumberger; Considering eccentricity; Measured dispersion and slowness are matched to a database.
Schlumberger Technology Corporation	US2018 0149 019A1 [57]	Classification executed by machine learning classifier; Features considered: slowness and attenuation characteristics; Quadripole source considered
Schlumberger Technology Corporation	WO2019 084 219A1 [14]	Machine learning using SVM, CNN and Auto Encoders Slowness images fed as input for the classifier
Halliburton Energy Services, Inc.	WO2017 048 862A1 [13]	Uses acoustic wave form features and well completion data; To determine material properties for various stages of casings.
Wellguard AS	US2019 0226 319A1 [15]	Contact with inner casing Eigenfrequencies as the main measurement Digital signal processing

From this review and staying abreast of the excellent results found in the application of guided waves, specifically the Stoneley waves, in the analysis of defects, it was decided to analyze the behavior of these waves in presence of defects through the tubing layer.

2.2
Typical Cement Bonding Defects

The verification of cement quality and thickness in oil wells is of great importance, since cement in addition to contributing to the insulation of groundwater promotes structural support [3] [58] [59] [60] [61]**.** Among the most common defects in wells and existing conditions that hinder their identification, one can mention the following, microannulus, free pipe, inner or outer debonding, casing eccentricity, tubing eccentricity, eccentric tool, low impedance cement. These are explained bellow [62] [63] [64] [65].

2.2.1
Microannulus

Microannulus is a partial uncoupling defect in the order of thousandth of an inch present between cement and casing or forming or between the cement and the formation, and can often be approximated by losing only the "shear" coupling between layers. This defect is so small that cement prevents its filling with any fluid. It is important to highlight that if this defect is of a larger order, its reading can range from a partial uncoupling to the condition of free pipe, which is a total uncoupling [2] [3].

Figure 2.10 shows a representation of microannulus in an oil well.

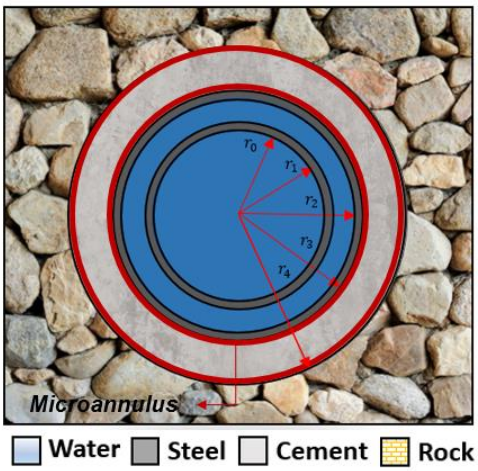

Figure 2.10– Representation of Microannulus. The red regions represent the defect.

There are several scenarios that promote the appearance of microannulus. After the cement curing, the heat lost in this process can shrink the cement, therefore producing a microannulus [1] [2]. Moreover, during well operation, low pressures can occur inside the well causing the casing uncouple and again producing the microannulus. If the fluid inside the well is replaced by a lighter fluid, the variation of hydrostatic pressure can also facilitate the appearance of microannulus [1] [2].

Another common cause for the occurrence of this defect is due to varnishing layer at the casing surface that protects steel against oxidation. Since heat from the hydration process and the alkalinity of the "slurry" dissolve the varnish, and thus generates a gap [1]**.** This phenomenon is commonly observed during well cementation, however, this type of defect can be eliminated with a subsequent pressurization treatment.

2.2.2
Free Pipe

This type of defect is a total uncoupling that exists between casing and cement. This causes the acoustic signal generated by the logging tool to not be able to propagate to the outer layers of the casing and fully reflect. This prevents the possibility of identifying other intrinsic defects in cement and its interface with

formation. This defect can also be represented by Figure 2.10, but the red regions, in this case, represent a full uncoupling.

In conventional acoustic logging tools, this defect causes the received CBL signal to present high amplitude, while in VDL it presents parallel vertical lines with high contrast, being indicative of the absence of signals that comes from the cement [1] [2].

The reflections on the casing collars in a free pipe condition can be observed on the VDL chart as visual effects known as “Chevrons”. It may also result from decreased amplitude of formation signals and increased transit time (TT) signal amplitude. The amplitude of CBL signal, in this case, is maximum because no waves leak to formation and cement layer.

2.2.3
Inner and Outer Debonding

The reduction of cement thickness is a defect that deserves attention because it compromises the structure of the well [3]. Figure 2.11 shows a representation of a thin cement sheath caused by debonding in cased wellbore.

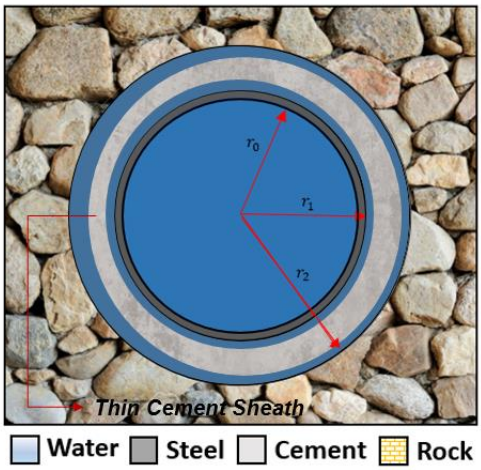

Figure 2.11 – Representation of Thin Cement Sheath. The blue region represents the defect.

This defect reduces signal attenuation and can be misinterpreted as a poor cement bonding condition. Besides, in ultrasonic tools, the reduction in cement thickness would result in a phenomenon in the VDL graphic known as "Cat Eyes" [3].

This defect arises as a result of the existence of fluids present in the interfaces cement/casing and cement/formation. This leads to cement corrosion, usually also resulting in a thick defect in a given azimuth. This may favor the appearance of another defect, which is the decentralization of the casing, which is more common in horizontal wells where gravity contributed to this effect.

2.2.4
Casing Eccentricity

Figure 2.12 shows a representation of an eccentric casing in a cased wellbore. As started above, casing eccentricity is more common in horizontal wells due to the gravity effect. However, even with the existence of centralizers on the casing, this eccentricity in vertical wells can still appear [54].

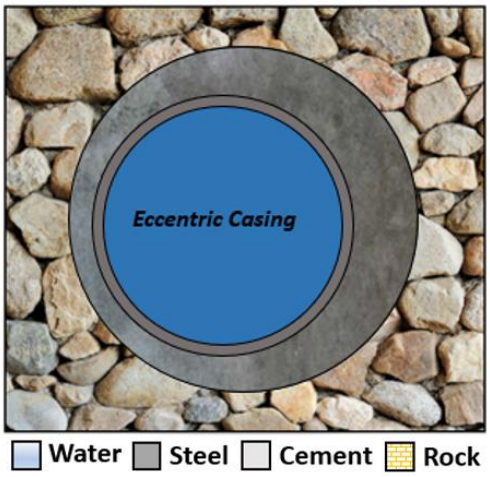

Figure 2.12 - Representation of an Eccentric Casing

This defect, besides being hardly detected by tools that do not have azimuthal resolution, compromises the structure of the well because most of the time it is associated with the wear and partial corrosion of cement.

2.2.5
Tubing Eccentricity

Analogous to the defect of coating eccentricity, there is the eccentricity of the production column, which, by contrast, is extremely common in vertical wells [54]. Strictly speaking, it is not a defect, but rather a condition that must be taken into account when the well scan is done without the removal of the production tubing because its results in an apparently reduction of the thickness of the annulus in a given azimuth due to the variation of the signal intensity. Figure 2.13 shows a representation of tubing eccentricity.

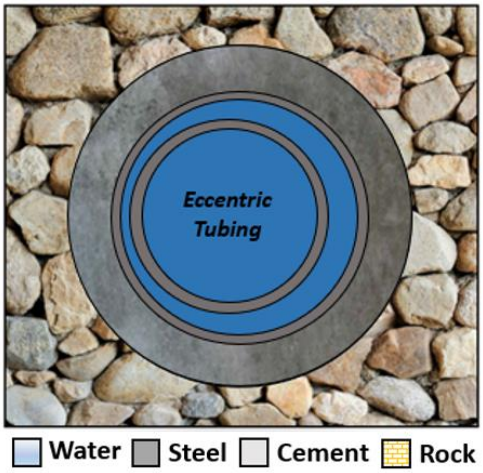

Figure 2.13 – Representation of Tubing Eccentricity.

2.2.6
Cement Channeling

Channeling consists of one or several fluid channels present within the cement layer [8] [23] [44]. This defect can arise in different ways. It could be due to small faults present in the casing that allows the fluid inside the well to leak to the cement, or to the fluids present in the formation that come in contact with the cement [8]. Figure 2.14 shows a representation of channeling in an oil well.

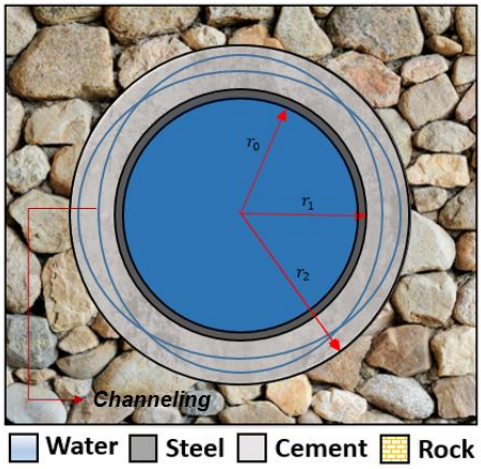

Figure 2.14 – Representation of Channeling. The blue regions represent the defect.

Like microannulus, channeling affects the signal acquired by conventional tools resulting in a moderate increase in CBL amplitude and casing signals presented in the VDL microseismogram [1] [66]. This defect may appear in only a few regions of cement or axissymmetrically, similar to rings inside the cement. Moreover, ultrasonic tools based on the pulse echo are more effective than conventional ones in detecting this defect because they measure cement quality in different azimuths.

If this defect is not identified and properly treated, the fluid present in channeling may come in direct contact with the surface of the casing and cause

issues, ranging from corrosion to major damage, thus compromising the structure of the well [1].

2.2.7
Tool Eccentricity

Eccentricity in a conventional sonic tool decreases the accuracy when interpreting logging charts [2] [3]. The most modern ultrasonic tools, such as Segmented Bond Tools (SBT) [3], are not affected by this defect because, in addition to shorter distances between the emitters and receivers, the transducers are in direct contact with the inner wall of the casing.

In the case of the CBL signal obtained by conventional tools, eccentricity will provide a decrease in amplitude and an increase in attenuation and may lead to false conclusions about the actual condition of the well [2] [3]. Another common effect due to the eccentricity of the eccentricity of the tool is the reduction of the transit time (TT) due to the acoustic path becoming smaller, however the latter ends up being beneficial because together with the other signals obtained it is possible to identify when there is no eccentricity validated the results [2] [3]**.** Figure 2.15 shows a representation of an eccentric tool and how it influences the acoustic way.

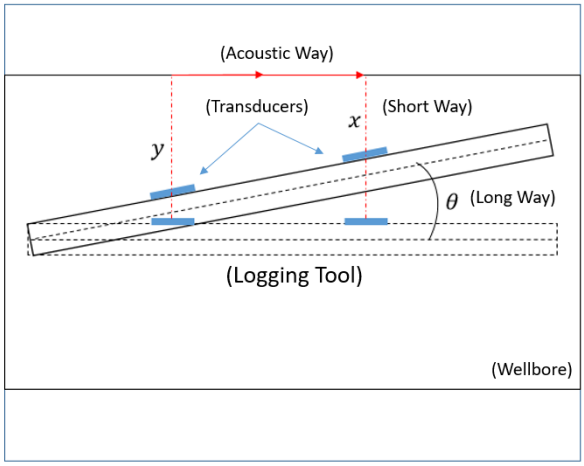

Figure 2.15 – Path of acoustic wave. The distance y between the tool and the coating varies little, but as the tool eccentricity is bigger on the bottom, the distance x varies even more.

2.2.8
Low Impedance Cement

Some types of complex cements have impedance values that may be lower than the impedance of the water, even approaching the impedances of the air [3] [44]. This can compromise the identification of possible defects, such as thin cement sheath or debonding, rendering to ambiguity in the interpretation of CBL/VDL tools charts [3] [44].

This happens because the order that the echoes arrive from the several layers in the well, are altered, hindering identification of the pulse of interest and

analysis of the signal intensity [3]. This actually happens due to the propagation speed which is a function of the material acoustic impedance.

2.3
Stoneley (ST), Scholte and Rayleigh waves

The Stoneley wave (ST) is a type of guided wave that propagates in the interface of two media [2]. STs are generated by sonic tools in wellbores. The Stoneley waves propagate between two solid media, thus occur along the walls of a well. Analysis of Stoneley waves can allow estimation of the locations of fracture and permeability of the formation [67] and investigate the cement condition.

Rayleigh's wave is another type of interface waves, which travel in vacuum-solid surfaces [68]. Rayleigh's wave is very often used in non-destructive testing for detecting defects [68]. As well as Stoneley's waves, Rayleigh wave present most of its energy close to the interface and shows an exponential decay away from the interface's as presented in Figure 2.16.

Scholte's waves are presented at a fluid-solid interface. Similarly, most of the energy in this type of wave is presented in the interface and shows an exponential decay away from the interface. Furthermore, the velocity of this interface waves is less than compressional and shear waves propagating in the same media.

Figure 2.16 shows a resume of interface waves presented.

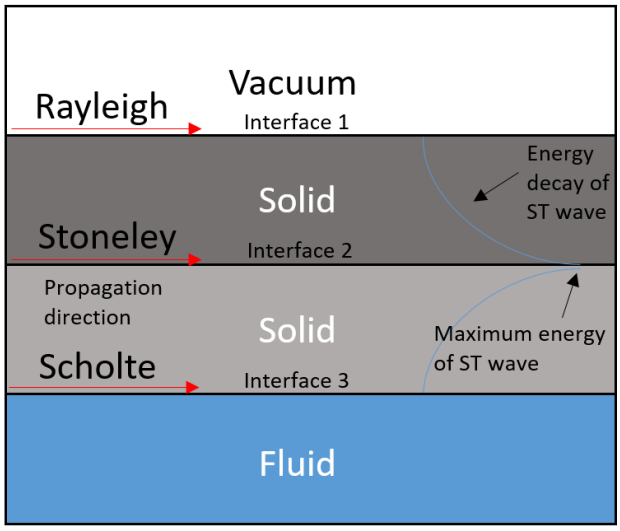

Figure 2.16 – Representation of interface waves. One can observe the type of interface waves between the respective media. The maximum energy is concentrated at the interface and decay exponentially.

3
Analytical Modeling Methods

In this Chapter, analytic equations present in literature are used to model the propagation of guided waves in multilayered cylinders. The Section 3.1 use the Elastodynamic to obtain the displacement, stress and strain equations. The superficial impedance tensor is calculated for all interfaces of the cylinder and depending on the external media a specific dispersion equation is found. The Section 3.2 approach the circumferential mode used in harmonic functions. The Section 3.3 present the Poynting vector equation applied in a solid and a fluid layer and the Section 3.4 present a brief explanation about group velocity.

3.1
Analytical solution of the problem of guided waves propagation in cylindrical layers

3.1.1
Linear Elastodynamics

The Figure 3.1 represents a hollow, homogeneous, isotropic and elastic cylindrical layer.

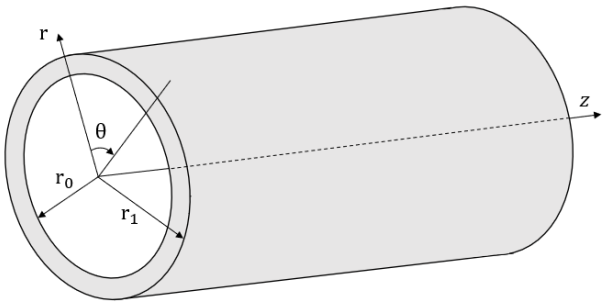

Figure 3.1 – Coordinate System in a Hollow Cylindrical Layer

From elastodynamic, can be written to this layer, the equations that govern the behaviour of the strain, stress, displacement and velocity fields [20]. This behaviour is obtained by the motion equation, the definition of strain as a function of displacement and the constitutive relationship that are presented, respectively, by Equation (3.1), (3.2) and (3.3) below [69].

$$\sigma_{ij,j} + \rho f_i = \rho \ddot{u}_i \tag{3.1}$$

$$\varepsilon_{ij} = \frac{1}{2}\left(u_{i,j} + u_{j,i}\right) \tag{3.2}$$

$$\sigma_{ij} = \lambda \varepsilon_{kk} \delta_{ij} + 2\mu \varepsilon_{ij} \tag{3.3}$$

where σ represents the stress tensor, ε the strain tensor, u the displacement field, f the external forces, ρ the density and λ and μ the lame constants.

Equations (3.1) and (3.2) are valid for any continuous medium, and Equation (3.3) for isotropic media. Replacing the constitutive relationship and strain as a function of displacement in the motion equation, the Navier equation is obtained for an isotropic medium presented by Equation (3.4).

$$\mu u_{i,jj} + (\lambda + \mu) u_{j,ji} + \rho f_i = \rho \ddot{u}_i \tag{3.4}$$

If the isotropic and elastic cylinder does not have body forces ($f = 0$). The Navier equation [20] [69] [70] can also be written in vector notation presented in Equation (3.5).

$$(\lambda + \mu)\nabla(\nabla \cdot u) + \mu \nabla^2 u = \rho \frac{\partial^2 u}{\partial t^2} \tag{3.5}$$

The dilatation of the material, Δ, is given by:

$$\Delta = \nabla \cdot u \tag{3.6}$$

and the rotation vector, ω, is given by:

$$\omega = \frac{1}{2}\nabla \times u \tag{3.7}$$

The Navier equation can be rewritten using these parameters as shown in Equation (3.8).

$$(\lambda + 2\mu)\nabla\Delta - 2\mu\nabla \times \omega = \rho \frac{\partial^2 u}{\partial t^2} \tag{3.8}$$

From the density and Lamé constants, the velocity of the bulk waves in the material are determined: c_L indicate the velocity of longitudinal waves and c_T indicate the shear wave velocity and can be calculated by Equations (3.9) and (3.10) [69].

$$c_L = \sqrt{\frac{\lambda + 2\mu}{\rho}} \tag{3.9}$$

$$c_T = \sqrt{\frac{\mu}{\rho}} \tag{3.10}$$

The displacement field of the isotropic and homogeneous cylindrical layer presented can be represented by vector:

$$u(r, \theta, z, t) = \begin{Bmatrix} u_r \\ u_\theta \\ u_z \end{Bmatrix} \tag{3.11}$$

Where r, θ and z are the main directions of the cylindrical system adopted. This system was adopted due to the convenience of describing a cylindrical body in it.

The displacement can be represented by the harmonic function in Equation (3.12).

$$u = \bar{u}(r) e^{i(\upsilon\theta + k_z z - \omega t)} \tag{3.12}$$

Which υ is the index of the circumferential mode, k_z the wave number in the z direction and ω the angular frequency.

Since the cylindrical body is isotropic, the displacement field can be expressed by a sum of potentials, a dilatational scalar potential φ and an equivoluminal vector potential ψ, from Helmholtz decomposition [69], i.e.:

$$u = \nabla\varphi + \nabla \times \psi \tag{3.13}$$

In cylindrical coordinates the vector potential, ψ, is expressed according to two other scalar potentials, namely χ and η, as can be seen in Equation (3.14).

$$\psi = \chi e_z + \nabla \times (\eta e_z) \tag{3.14}$$

Therefore, the displacement field can be rewritten according to the three scalar potentials presented, i.e.:

$$\mathrm{u} = \nabla\varphi + \nabla \times (\chi e_z) + \nabla \times \nabla \times (\eta e_z) \tag{3.15}$$

It is necessary to use the boundary conditions to solve the equation that governs the displacement field throughout the cross section of the cylindrical body. To simplify the problem, it is assumed that the cylindrical layer is infinitely long, which makes its volume infinite. This condition causes the invariant volume condition, also known as “Gauge Condition” [70] and presented in Equation (3.16).

$$\nabla \cdot \psi = 0 \tag{3.16}$$

Applying this condition allows one to solve the problem without the need for addressing boundary conditions at both ends of the cylindrical body.

From Equation (3.13) and (3.8), wave equations are obtained for the potentials φ and ψ, presented in Equation (3.17) and (3.18).

$$\nabla^2\varphi = \frac{1}{c_L^2}\frac{\partial^2\varphi}{\partial t^2} \tag{3.17}$$

$$\nabla^2\psi = \frac{1}{c_T^2}\frac{\partial^2\psi}{\partial t^2} \tag{3.18}$$

Remembering that the potential ψ is replaced by two scalar potentials, Equation (3.14), the wave equation can also be written as:

$$\left[\nabla^2 - \frac{1}{c_L^2}\frac{\partial^2}{\partial t^2}\right]\varphi = 0 \tag{3.19}$$

$$\left[\nabla^2 - \frac{1}{c_T^2}\frac{\partial^2}{\partial t^2}\right]\begin{Bmatrix}\chi\\ \eta\end{Bmatrix} = 0 \tag{3.20}$$

Computing the gradient and rotational operations of the potentials in the Equation (3.15), in cylindrical coordinates, the relationship between the displacement field and the potentials can be written as:

$$\mathrm{u_r} = \frac{\partial\varphi}{\partial r} + \frac{1}{r}\frac{\partial\chi}{\partial\theta} + \frac{\partial^2\eta}{\partial z\partial r} \tag{3.21}$$

$$\mathrm{u_\theta} = \frac{1}{r}\frac{\partial\varphi}{\partial\theta} - \frac{\partial\chi}{\partial r} + \frac{1}{r}\frac{\partial^2\eta}{\partial z\partial\theta} \tag{3.22}$$

$$u_z = \frac{\partial \varphi}{\partial z} + \frac{\partial^2 \eta}{\partial z^2} - \frac{1}{c_T^2}\frac{\partial^2 \eta}{\partial t^2} \tag{3.23}$$

Replacing the Equation (3.20) in Equation (3.23), the displacement u_z can be written as:

$$u_z = \frac{\partial \varphi}{\partial z} - \frac{\partial}{r\partial r}\left(r\frac{\partial \eta}{\partial r}\right) - \frac{\partial^2 \eta}{r^2 \partial \theta^2} \tag{24}$$

Consider now ϕ a vector composed by scalar potentials φ, χ and η as presented in Equation (3.25).

$$\phi = \begin{Bmatrix} \varphi \\ \chi \\ \eta \end{Bmatrix} \tag{3.25}$$

The displacement field can be express by the multiplication of a differential matrix operator, A with the scalar potential vector ϕ as shown in Equation (3.26) below.

$$u = A\,\phi \tag{3.26}$$

From Equations (3.21) and (3.24), the differential matrix operator A can be written as:

$$A = \begin{bmatrix} \frac{\partial}{\partial r} & \frac{1}{r}\frac{\partial}{\partial \theta} & \frac{\partial^2}{\partial z \partial r} \\ \frac{1}{r}\frac{\partial}{\partial \theta} & -\frac{\partial}{\partial r} & \frac{1}{r}\frac{\partial^2}{\partial z \partial \theta} \\ \frac{\partial}{\partial z} & 0 & \left(\frac{\partial^2}{\partial z^2} - \frac{1}{c_T^2}\frac{\partial^2}{\partial t^2}\right) \end{bmatrix} \tag{3.27}$$

Considering that the scalar potentials vector ϕ, can be represent by the harmonic function below:

$$\phi = \bar{\phi}\,(r) e^{i(v\theta + k_z z - \omega t)} \tag{3.28}$$

and applying the derivations of the differential matrix operator in harmonic function ϕ, the expression to the amplitude of displacement field, $\bar{u}$, in function of potentials amplitude $\bar{\phi}$ can be founded.

$$\bar{\mathrm{u}} = \bar{A}\,\bar{\phi} \tag{3.29}$$

Where $\bar{A}$ can be defined as:

$$\bar{A} = \begin{bmatrix} \dfrac{d}{dr} & i\dfrac{\nu}{r} & ik_z\dfrac{d}{dr} \\ i\dfrac{\nu}{r} & -\dfrac{d}{dr} & -k_z\dfrac{\nu}{r} \\ ik_z & 0 & \left(\dfrac{\omega^2}{c_T^2} - k_z^2\right) \end{bmatrix} \tag{3.30}$$

Replacing the harmonic function ϕ in wave equations for potentials, Equation (3.19) and (3.20), and applying the laplacian in cylindrical coordinates, the follow expressions can be founded:

$$\left[\frac{d^2}{dr^2} + \frac{1}{r}\frac{d}{dr} + \left(\frac{\omega^2}{c_L^2} - k_z^2\right) - \frac{v^2}{r^2}\right]\bar{\varphi} = 0 \tag{3.31}$$

$$\left[\frac{d^2}{dr^2} + \frac{1}{r}\frac{d}{dr} + \left(\frac{\omega^2}{c_T^2} - k_z^2\right) - \frac{v^2}{r^2}\right]\begin{Bmatrix}\bar{\chi}\\ \bar{\eta}\end{Bmatrix} = 0 \tag{3.32}$$

Or using a simplified form:

$$\left[\frac{d^2}{dr^2} + \frac{1}{r}\frac{d}{dr} + k_j^2 - \frac{v^2}{r^2}\right]\bar{\phi} = 0 \tag{3.33}$$

where

$$k_j = \begin{cases} \left(\dfrac{\omega^2}{c_j^2} - {k_z}^2\right)^{\frac{1}{2}}, & \text{se } \dfrac{\omega}{c_j} \geq k_z \\ i\left({k_z}^2 - \dfrac{\omega^2}{c_j^2}\right)^{\frac{1}{2}}, & \text{otherwise} \end{cases} \tag{3.34}$$

and

$$j = L, T \tag{3.35}$$

The Equation (3.33) is a second order ordinary differential equation and can be solved using Bessel and Hankel Functions, as shown in appendix A.

Considering that in the cylindrical layer the displacement field, $\mathrm{u}(r)$, is composed of the sum of a wave that propagates in the increasing radial direction, called outgoing wave, $\mathrm{u}_1(r)$, and a wave that propagates in the decreasing radial direction, called incoming waves, $\mathrm{u}_2(r)$, [21] the solution of Equation 33 can be presented by Equations (3.36), (3.37) and (3.38).

$$\bar{\varphi}(r) = \alpha_1 H_\upsilon^1(k_L r) + \alpha_2 H_\upsilon^2(k_L r) \tag{3.36}$$

$$\bar{\chi}(r) = \beta_1 H_\upsilon^1(k_T r) + \beta_2 H_\upsilon^2(k_T r) \tag{3.37}$$

$$\bar{\eta}(r) = \gamma_1 H_\upsilon^1(k_T r) + \gamma_2 H_\upsilon^2(k_T r) \tag{3.38}$$

where H_υ^1 e H_υ^2 are Hankel functions.

The Equations (3.36), (3.37) and (3.38) can be concisely represented in Equation (3.39).

$$\bar{\phi}(r) = \sum_{\alpha=1}^{2} \Phi_a(r) c_a \tag{3.39}$$

Where the matrix $\Phi_a(r)$ is composed by Hankel function as described below:

$$\Phi_a(r) = \begin{bmatrix} H_\upsilon^\alpha(k_L r) & 0 & 0 \\ 0 & H_\upsilon^\alpha(k_T r) & 0 \\ 0 & 0 & H_\upsilon^\alpha(k_T r) \end{bmatrix} \tag{3.40}$$

and c_a is a vector of constants defined as:

$$c_a = \begin{pmatrix} \alpha_a \\ \beta_a \\ \gamma_a \end{pmatrix} \tag{3.41}$$

Applying the Equation (3.39) in Equation (3.29), one can obtain:

$$\bar{\mathrm{u}}(r) = \sum_{\alpha=1}^{2} \bar{\mathrm{u}}_a(r) = \sum_{\alpha=1}^{2} \bar{A}\, \Phi_a(r) c_a \tag{3.42}$$

The derivation of Hankel's functions with respect to radius in matrix equation (3.42), can be consulted in appendix A.

So $\bar{\mathrm{u}}_a(r)$ can be written as:

$$\bar{\mathrm{u}}_a(r) = A_\alpha(r)\tau_a(r)c_a \tag{3.43}$$

where the matrix $A_\alpha(r)$ can be seen in appendix B and the tensor $\tau_a(r)$ is the matrix composed by exponential functions resulting from change of scale of the Hankel functions.

$$\tau_1(r) = \begin{bmatrix} e^{ik_L r} & 0 & 0 \\ 0 & e^{ik_T r} & 0 \\ 0 & 0 & e^{ik_T r} \end{bmatrix} \tag{3.44}$$

One can also see that:

$$\tau_2(r) = {\tau_1}^{-1}(r) \tag{3.45}$$

3.1.2
Strain and Stress Fields

From the Equation (3.2), the strain as a function of displacement can be written in cylindrical coordinates, as shown in Equation (3.46) to (3.51).

$$\varepsilon_{rr} = \frac{\partial u_r}{\partial r} \tag{3.46}$$

$$\varepsilon_{\theta\theta} = \frac{1}{r}\left(\frac{\partial u_\theta}{\partial \theta} + u_r\right) \tag{3.47}$$

$$\varepsilon_{zz} = \frac{\partial u_z}{\partial z} \tag{3.48}$$

$$\varepsilon_{r\theta} = \frac{\partial u_r}{r\partial \theta} + r\frac{\partial}{\partial r}\left(\frac{u_\theta}{r}\right) \tag{3.49}$$

$$\varepsilon_{z\theta} = \frac{\partial u_z}{r\partial\theta} + \frac{\partial u_\theta}{\partial z} \tag{3.50}$$

$$\varepsilon_{rz} = \frac{\partial u_r}{\partial z} + \frac{\partial u_z}{\partial r} \tag{3.51}$$

Expanding the constitutive relationship in cylindrical coordinates, the expressions for the normal and shear stress components are expressed according to the strain field:

$$\sigma_{rr} = \lambda(\nabla \cdot u) + 2\mu\varepsilon_{rr} \tag{3.52}$$

$$\sigma_{\theta\theta} = \lambda(\nabla \cdot u) + 2\mu\varepsilon_{\theta\theta} \tag{3.53}$$

$$\sigma_{zz} = \lambda(\nabla \cdot u) + 2\mu\varepsilon_{zz} \tag{3.54}$$

$$\sigma_{r\theta} = \mu\varepsilon_{r\theta} \tag{3.55}$$

$$\sigma_{z\theta} = \mu\varepsilon_{z\theta} \tag{3.56}$$

$$\sigma_{rz} = \mu\varepsilon_{rz} \tag{3.57}$$

From Equations (3.44) to (3.55), the stress field in function of displacement are written as:

$$\sigma_{rr} = \left[(2\mu + \lambda)\frac{\partial}{\partial r} + \frac{\lambda}{r}\right]u_r + \lambda\frac{1}{r}\frac{\partial}{\partial\theta}u_\theta + \lambda\frac{\partial}{\partial z}u_z \tag{3.58}$$

$$\sigma_{\theta\theta} = \left[(2\mu + \lambda)\frac{1}{r} + \lambda\frac{\partial}{\partial r}\right]u_r + (2\mu + \lambda)\frac{1}{r}\frac{\partial}{\partial\theta}u_\theta + \lambda\frac{\partial}{\partial z}u_z \tag{3.59}$$

$$\sigma_{zz} = \lambda\left(\frac{\partial}{\partial r} + \frac{1}{r}\right)u_r + \lambda\frac{1}{r}\frac{\partial}{\partial\theta}u_\theta + (2\mu + \lambda)\frac{\partial}{\partial z}u_z \tag{3.60}$$

$$\sigma_{r\theta} = \mu\frac{1}{r}\frac{\partial}{\partial\theta}u_r + \mu\left(\frac{\partial}{\partial r} - \frac{1}{r}\right)u_\theta \tag{3.61}$$

$$\sigma_{z\theta} = \frac{\mu}{r}\frac{\partial}{\partial\theta}u_z + \mu\frac{\partial}{\partial z}u_\theta \tag{3.62}$$

$$\sigma_{rz} = \mu \frac{\partial}{\partial z} u_r + \mu \frac{\partial}{\partial r} u_z \tag{3.63}$$

Let

$$\mathrm{t}^{(r)}(r,\theta,z,t) = \begin{Bmatrix} \sigma_{rr} \\ \sigma_{r\theta} \\ \sigma_{rz} \end{Bmatrix} \tag{3.64}$$

be the stress vector acting on the normal surface to the radial direction, ω, where this vector can be represented by the harmonic function:

$$\mathrm{t}^{(r)} = \bar{\mathrm{t}}^{(r)}(r) e^{i(\upsilon\theta + k_z z - \omega t)} \tag{3.65}$$

From the Equations that relate strain and stress, one can write it in matrix form:

$$\bar{\mathrm{t}}^{(r)} = \bar{B}\bar{u} \tag{3.66}$$

From Equations (3.58) to (3.63), the differential operator B is given by:

$$\bar{B} = \begin{bmatrix} 2\mu\frac{d}{dr} + \lambda\left(\frac{d}{dr} + \frac{1}{r}\right) & i\lambda\frac{\nu}{r} & i\lambda k_z \\ i\mu\frac{\nu}{r} & \mu\left(\frac{d}{dr} - \frac{1}{r}\right) & 0 \\ i\mu k_z & 0 & \mu\frac{d}{dr} \end{bmatrix} \tag{3.67}$$

From equations (3.29) and (3.66), it is found that:

$$\bar{\mathrm{t}}^{(r)} = \bar{B}\,\bar{A}\,\bar{\phi} = \bar{L}\,\bar{\phi} \tag{3.68}$$

where a new matrix differential operator $\bar{L}$ is given by:

$$\bar{L} = \begin{bmatrix} 2\mu\dfrac{d^2}{dr^2} - \lambda\dfrac{\omega^2}{c_L^2} & i2\mu\dfrac{\nu}{r}\left(\dfrac{d}{dr} - \dfrac{1}{r}\right) & i2\mu k_z\dfrac{d^2}{dr^2} \\ i2\mu\dfrac{\nu}{r}\left(\dfrac{d}{dr} - \dfrac{1}{r}\right) & -\mu\dfrac{\nu^2}{r^2} - \mu\left(\dfrac{d}{dr} - \dfrac{1}{r}\right)\dfrac{d}{dr} & -2\mu k_z\dfrac{\nu}{r}\left(\dfrac{d}{dr} - \dfrac{1}{r}\right) \\ i2\mu k_z\dfrac{d}{dr} & -\mu k_z\dfrac{\nu}{r} & \mu(k_T^2 - k_z^2)\dfrac{d}{dr} \end{bmatrix} \quad (3.69)$$

From Equation (3.40), of the potential field, and Equation (3.68), the stress vector can be written as:

$$\bar{\mathrm{t}}^{(r)}(r) = \sum_{\alpha=1}^{2} \bar{\mathrm{t}}_{\alpha}^{(r)}(r) \quad (70)$$

Applying the operations of matrix operator $\bar{L}$ in vector $\bar{\phi}$, one can write:

$$\bar{\mathrm{t}}_{\alpha}^{(r)}(r) = L_{\alpha}(r)\tau_a(r)c_a \quad (71)$$

where the matrix $L_{\alpha}(r)$ can be seen on appendix B and $\tau_a(r)$ was defined in Equation (3.44).

It is observed that to eliminate the vector of constants c_a in equations related to the stress tensor and displacement vector, first the displacement field is written at the inner radius of the cylindrical layer as shown in Equation (3.72).

$$\bar{\mathrm{u}}_a(r_0) = A_{\alpha}(r_0)\tau_a(r_0)c_a \quad (3.72)$$

Isolating the vector c_a in expression (3.72) above, one can write:

$$c_a = \tau_a^{-1}(r_0)A_{\alpha}^{-1}(r_0)\bar{\mathrm{u}}_a(r_0) \quad (3.73)$$

then, replacing Equation (3.73) in (3.43):

$$\bar{\mathrm{u}}_a(r) = A_{\alpha}(r)\tau_a(r)\tau_a^{-1}(r_0)A_{\alpha}^{-1}(r_0)\bar{\mathrm{u}}_a(r_0) \quad (3.74)$$

One can find the equation to the displacement field in radial position r as a function of the displacement field in r_0.

$$\bar{\mathrm{u}}_a(r) = A_{\alpha}(r)\tau_a(r - r_0)A_{\alpha}^{-1}(r_0)\bar{\mathrm{u}}_a(r_0) \quad (3.75)$$

The matrix operation that relates the displacement in position r, with the displacement at the inner radius r_0 of cylindrical body, can be defined as the matrix of propagation $M(r, r_0)$:

$$\bar{\mathrm{u}}_a(r) = M_a(r, r_0)\bar{\mathrm{u}}_a(r_0) \tag{3.76}$$

and its inverse is:

$$M_a^{-1}(r, r_0) = M_a(r_0, r) \tag{3.77}$$

Note that:

$$M_a(r_0, r_0) = I \tag{3.78}$$

Besides that, rewriting Equation (3.43) as:

$$\tau_a(r)c_a = A_\alpha^{-1}(r)\bar{\mathrm{u}}_a(r) \tag{3.79}$$

and replacing the stress vector, Equation (3.71), one can be eliminate the vector of constants c_a

$$\bar{\mathrm{t}}_\alpha^{(r)}(r) = L_\alpha(r)A_\alpha^{-1}(r)\bar{\mathrm{u}}_a(r) \tag{3.80}$$

The local impedance matrix in the radial direction of the homogeneous cylinder is defined as:

$$Z_\alpha(r) = \frac{i}{\omega}L_\alpha(r)A_\alpha^{-1}(r) \tag{3.81}$$

and the Equation (3.80) can be rewritten as:

$$\bar{\mathrm{t}}_\alpha^{(r)}(r) = -i\omega Z_\alpha(r)\bar{\mathrm{u}}_a(r) \tag{3.82}$$

Let

$$\mathrm{t}^{(z)}(r,\theta,z,t) = \begin{Bmatrix} \sigma_{rz} \\ \sigma_{z\theta} \\ \sigma_{zz} \end{Bmatrix} \tag{3.83}$$

be the stress vector acting on the normal surface to the longitudinal direction, where this vector can be expressed by the following harmonic function:

$$\mathrm{t}^{(z)} = \bar{\mathrm{t}}^{(z)}(r)e^{i(v\theta + k_z z - \omega t)} \tag{3.84}$$

again, from the equations that relate the stress and the displacement, one can write it in matrix form the Equation (3.85), below.

$$\bar{\mathrm{t}}^{(z)} = \bar{C}\bar{u} \tag{85}$$

From equations (3.58) to (3.63), it is concluded that the matrix differential operator $\bar{C}$ is given by:

$$\bar{C} = \begin{bmatrix} i\mu k_z & 0 & \mu\dfrac{d}{dr} \\ 0 & i\mu k_z & i\mu\dfrac{v}{r} \\ \lambda\left(\dfrac{d}{dr} + \dfrac{1}{r}\right) & 0 & i(\lambda + 2\mu)k_z \end{bmatrix} \tag{3.86}$$

From matrix equation that relate the displacement field with the potential vector, Equation (3.29), one can get:

$$\bar{\mathrm{t}}^{(z)} = \bar{C}\,\bar{A}\,\bar{\phi} = \bar{S}\,\bar{\phi} \tag{3.87}$$

where $\bar{S}$ is given by:

$$\bar{S} = \begin{bmatrix} i2\mu k_z\dfrac{d}{dr} & -\mu k_z\dfrac{v}{r} & \mu(k_T^2 - k_z^2)\dfrac{d}{dr} \\ -2\mu k_z\dfrac{v}{r} & -i\mu k_z\dfrac{d}{dr} & i\mu(k_T^2 - k_z^2)\dfrac{v}{r} \\ 2\mu k_L^2 - (\lambda + 2\mu)\dfrac{\omega^2}{c_L^2} & 0 & i2\mu k_z k_T^2 \end{bmatrix} \tag{3.88}$$

From the sum presented in Equation (3.39), one can write the stress vector as:

$$\bar{\mathrm{t}}^{(z)}(r) = \sum_{\alpha=1}^{2} \bar{\mathrm{t}}_{\alpha}^{(r)}(r) \tag{3.89}$$

Applying the operations of Equation (3.87), it is written:

$$\bar{\mathrm{t}}_{\alpha}^{(z)}(r) = S_{\alpha}(r)\tau_{a}(r)c_{a} \tag{3.90}$$

where the matrix $S_{\alpha}(r)$ can be seen on appendix B.

Performing the same procedure presented previously to eliminate the vector of constants c_a, the following expression is obtained:

$$\bar{\mathrm{t}}_{\alpha}^{(z)}(r) = S_{\alpha}(r)A_{\alpha}^{-1}(r)\bar{\mathrm{u}}_{a}(r) \tag{3.91}$$

Defining the local Impedance matrix in the longitudinal direction of the homogeneous cylinder as:

$$Y_{\alpha}(r) = \frac{i}{\omega}S_{\alpha}(r)A_{\alpha}^{-1}(r) \tag{3.92}$$

the stress vector acting on the normal surface to the longitudinal direction is rewritten as:

$$\bar{\mathrm{t}}_{\alpha}^{(z)}(r) = -i\omega Y_{\alpha}(r)\bar{\mathrm{u}}_{a}(r) \tag{3.93}$$

3.1.3
Superficial Impedance of a Cylindrical Layer

Figure 3.2 presents a section of the homogeneous and isotropic cylindrical body analyzed. On its inner surface, the surface Impedance tensor, represented by G_0, is defined as:

$$\bar{\mathrm{t}}^{(r)}(r_0) = -i\omega G_0\bar{\mathrm{u}}(r_0) \tag{3.94}$$

If the inner surface is in contact with the vacuum, the surface Impedance G_0 is zero because the surface is free of stresses. Similarly, on the outer surface, the surface Impedance tensor, represented by G_1, is defined.

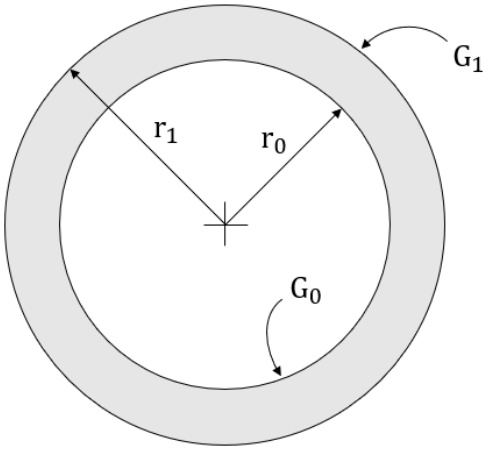

Figure 3.2 - Homogeneous and isotropic cylindrical body with internal and external surface characterized by impedance tensors G_0 e G_1, respectively.

An important parameter to calculate surface impedance is the generalized reflection tensor $H(r)$, which relates incoming waves with outgoing waves at a given radial position as shown in Equation (3.95).

$$\bar{u}_1(r) = H(r)\bar{u}_2(r) \tag{3.95}$$

At the Inner surface of the cylindrical body the reflection tensor is given by R_0, note that in this case:

$$\bar{\mathrm{u}}_1(r_0) = \mathrm{R}_0\, \bar{\mathrm{u}}_2(r_0) \tag{3.96}$$

From the displacement wave Equation (3.42) and Equation (3.94) above, one can write:

$$\bar{\mathrm{u}}_2(r_0) = (\mathrm{R}_0 + \mathrm{I})^{-1}\bar{\mathrm{u}}(r_0) \tag{3.97}$$

From Equation (3.82) for the stress vector and applying it at the Inner surface of the cylindrical body, it is written:

$$\bar{\mathrm{t}}^{(r)}(r_0) = -i\omega\big(Z_1(r_0)\bar{\mathrm{u}}_1(r_0) + Z_2(r_0)\bar{\mathrm{u}}_2(r_0)\big) \tag{3.98}$$

Replacing Equation (3.96) into Equation (3.98), gives:

$$\bar{\mathrm{t}}^{(r)}(r_0) = -i\omega\big(Z_1(r_0)\mathrm{R}_0 + Z_2(r_0)\big)\,\bar{\mathrm{u}}_2(r_0) \tag{3.99}$$

and matching with the Equation (3.97), it can be written:

$$\bar{\mathrm{t}}^{(r)}(r_0) = -i\omega\big(Z_1(r_0)\mathrm{R}_0 + Z_2(r_0)\big)(\mathrm{R}_0 + \mathrm{I})^{-1}\bar{\mathrm{u}}(r_0) \quad (100)$$

From Equations (94) and (100), the reflection tensor can be obtain by:

$$\mathrm{R}_0 = [Z_1(r_0) - G_0]^{-1}\,[G_0 - Z_2(r_0)] \quad (3.101)$$

The outgoing displacement wave can be write from Equation (3.76) as:

$$\bar{u}_1(r) = M_1(r, r_0)\bar{u}_1(r_0) \quad (3.102)$$

and the incoming displacement wave as:

$$\bar{u}_2(r) = M_2(r, r_0)\bar{u}_2(r_0) \quad (3.103)$$

From Equation (3.101), (3.102) and (3.103), one finds:

$$M_1(r, r_0)\bar{u}_1(r_0) = H(r)M_2(r, r_0)\bar{u}_2(r_0) \quad (3.104)$$

and applying the Equation (3.94) in (3.104):

$$M_1(r, r_0)\mathrm{R}_0\,\bar{\mathrm{u}}_2(r_0) = H(r)M_2(r, r_0)\bar{u}_2(r_0) \quad (3.105)$$

From the Equation (3.105) above, the reflection tensor can be calculated by:

$$H(r) = M_1(r, r_0)\mathrm{R}_0 M_2^{-1}(r, r_0) \quad (3.106)$$

or then, know the property presented on Equation (3.77), one can write:

$$H(r) = M_1(r, r_0)\,\mathrm{R}_0 M_2(r_0, r) \quad (3.107)$$

From the same procedure used to arrive at Equation (3.98), the expression to the stress vector on outer surface of cylindrical body can be found as:

$$\bar{\mathrm{t}}^{(r)}(r_1) = -i\omega\left(Z_1(r_1)\bar{\mathrm{u}}_1(r_1) + Z_2(r_1)\bar{\mathrm{u}}_2(r_1)\right) \quad (3.108)$$

Using the expression of the generalized reflection tensor presented in Equation (3.95), one can obtain:

$$\bar{\mathrm{t}}^{(r)}(r_1) = -i\omega\left(Z_1(r_1)H(r_1)\bar{u}_2(r_1) + Z_2(r_1)\bar{\mathrm{u}}_2(r_1)\right) \quad (3.109)$$

Similarly, Equation (3.97), on outer surface, the outgoing and incoming displacement waves can be related on internal surface as:

$$\bar{\mathrm{u}}_2(r_1) = (H(r_1) + \mathrm{I})^{-1}\bar{\mathrm{u}}(r_1) \quad (3.110)$$

which makes the Equation (3.109) of stress vector on outer surface of cylindrical body can be written as:

$$\bar{\mathrm{t}}^{(r)}(r_1) = -i\omega\left(Z_1(r_1)H(r_1) + Z_2(r_1)\right)(H(r_1) + \mathrm{I})^{-1}\bar{\mathrm{u}}(r_1) \quad (3.111)$$

It is known that at the outer surface, the stress vector can be written in function of the surface impedance tensor, G_1, as:

$$\bar{\mathrm{t}}^{(r)}(r_1) = -i\omega G_1\bar{\mathrm{u}}(r_1) \quad (3.112)$$

and relating Equations (3.111) and (3.112), the follow expression to G_1 can be found.

$$G_1 = \left(Z_1(r_1)H(r_1) + Z_2(r_1)\right)(H(r_1) + \mathrm{I})^{-1} \quad (3.113)$$

3.1.4
Solid/Fluid Interface on the Internal Surface

The Figure 3.3 below shows a section of the studied cylindrical body containing fluid inside. In this case, the impedance tensor on the inner surface G_0 will be different as it depends on the acoustic properties of the fluid. The value of G_0 is derived as follow:

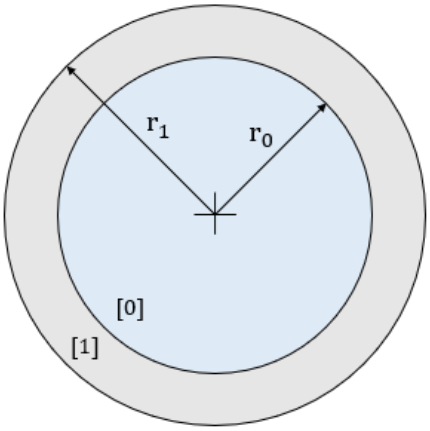

Figure 3.3 – Elastic cylindrical body with internal surface in contact with acoustic fluid

To obtain G_0, the pressure field in fluid is considered as a harmonic function:

$$p(r,\theta,z,t) = \bar{p}(r)e^{i(v\theta+k_z z-\omega t)} \tag{3.114}$$

'The wave equation to the pressure field is:

$$\left[\nabla^2 - \frac{1}{c_f}\frac{\partial^2}{\partial t^2}\right]p(r) = 0 \tag{3.115}$$

where c_f is the wave velocity in the fluid.

Applying the Equation (3.114) in the wave Equation (3.115), one can obtain in cylindrical coordinates:

$$\left[\frac{1}{r}\frac{d}{dr}\left(r\frac{d}{dr}\right) + \left(\frac{\omega^2}{c_f^2} - k_z^2\right) - \frac{v^2}{r^2}\right]\bar{p}(r) = 0 \tag{3.116}$$

or simply:

$$\left[\frac{d^2}{dr^2} + \frac{1}{r}\frac{d}{dr} + k_f^2 - \frac{v^2}{r^2}\right]\bar{p}(r) = 0 \tag{3.117}$$

where k_f is defined as:

$$k_f = \begin{cases} \left(\frac{\omega^2}{c_f^2} - {k_z}^2\right)^{\frac{1}{2}}, & \text{se } \frac{\omega}{c_f} \geq k_z \\ i\left({k_z}^2 - \frac{\omega^2}{c_f^2}\right)^{\frac{1}{2}}, & \text{otherwise} \end{cases} \tag{3.118}$$

Equation (3.117) as already seen is solved using the Bessel and Hankel functions. In this case, there is only the outgoing pressure wave, so the solution is a function of the Bessel functions.

$$\bar{p}(r) = c_1 J_v(k_f r) + c_2 Y_v(k_f r) \tag{3.119}$$

Be v the velocity vector in fluid:

$$\mathrm{v}(r,\theta,z,t) = \begin{Bmatrix} \mathrm{v_r} \\ \mathrm{v_\theta} \\ \mathrm{v_z} \end{Bmatrix} \tag{3.120}$$

which is a harmonic function represented by:

$$\mathrm{v}(r,\theta,z,t) = \bar{\mathrm{v}}(r) e^{i(v\theta + k_z z - \omega t)} \tag{3.121}$$

The relation between the velocity vector and the pressure field is given by Equation (3.122),

$$\frac{\partial \mathrm{v}}{\partial t} = -\frac{1}{\rho_f} \nabla p \tag{3.122}$$

and can be expanded in cylindrical coordinates as:

$$\frac{\partial \bar{\mathrm{v}}_r}{\partial t} = -\frac{1}{\rho_f} \frac{d\bar{p}(r)}{dr} \tag{3.123}$$

$$\frac{\partial \bar{\mathrm{v}}_\theta}{\partial t} = -\frac{iv}{\rho_f} \bar{p}(r) \tag{3.124}$$

$$\frac{\partial \bar{\mathrm{v}}_z}{\partial t} = -\frac{ik_z}{\rho_f} \bar{p}(r) \tag{3.125}$$

Let be ξ the multiplication between wave number and radius:

$$\xi = k_f r \tag{3.126}$$

so Equation (3.119) can be written as:

$$\bar{p}(r) = J_v(\xi)c_1 + Y_v(\xi)c_2 \tag{3.127}$$

Applying the property of the Bessel function presented in Equation (3.128), one can conclude that c_2 is zero, i.e.:

$$\lim_{\xi \to 0} Y_v(\xi) = -\infty \implies c_2 = 0 \tag{3.128}$$

Using the scale change of Bessel function, Equation (127) can be written as:

$$\bar{p}(r) = J_v(\xi)c_1 = e^{i\xi} j_v(\xi)c_1 \tag{3.129}$$

Applying Equations (3.114), (3.121), (3.128) and (3.129) in Equations (3.123) to (3.125), that relate the velocity and the pressure, one can write:

$$\bar{\mathrm{v}}_r(r) = -i\frac{k_f}{\rho_f \omega}\frac{d\bar{p}(\xi)}{d\xi} \tag{3.130}$$

$$\bar{\mathrm{v}}_\theta(r) = \frac{k_f v}{\rho_f \omega}\frac{\bar{p}(\xi)}{\xi} \tag{3.131}$$

$$\bar{\mathrm{v}}_z(r) = i\frac{k_z}{\rho_f \omega}\bar{p}(\xi) \tag{3.132}$$

Similarly, Equation (3.129) in (3.130), yield:

$$\bar{\mathrm{v}}(r) \cdot e_r = \bar{\mathrm{v}}_r(r) = -i\frac{k_f}{\rho_f \omega}\left(\frac{dJ_v(\xi)}{d\xi}\right)c_1 \tag{3.133}$$

where e_r unit vector in radial direction.

Isolating the constant c_1 in the Equation (3.133)

$$c_1 = i\frac{\rho_f \omega}{k_f}\left(\frac{dJ_v(\xi)}{d\xi}\right)^{-1}\bar{\mathrm{v}}(r)\cdot e_r \tag{3.134}$$

and applying the Equation (3.129) to eliminate c_1, one can find:

$$\bar{p}(r) = i\frac{\rho_f \omega}{k_f}\frac{J_v(\xi)}{\frac{dJ_v(\xi)}{d\xi}}\bar{\mathrm{v}}(r)\cdot e_r \tag{3.135}$$

Considering that the pressure field can be written as a function of the velocity vector:

$$\bar{p}(r) = \mathcal{Z}_f^{[0]}(r)\bar{\mathrm{v}}(r)\cdot e_r \tag{3.136}$$

where $\mathcal{Z}_f^{[0]}$ is the local impedance in fluid, and from Equation (3.135) and (3.136), it can be calculated by Equation (3.137) below.

$$\mathcal{Z}_f^{[0]}(r) = i\frac{\rho_f \omega}{k_f}\frac{J_v(k_f r)}{J_{v-1}(k_f r) - \frac{v}{k_f r}J_v(k_f r)} \tag{3.137}$$

or by:

$$\mathcal{Z}_f^{[0]}(r) = i\frac{\rho_f \omega}{k_f}\frac{j_v(k_f r)}{j_{v-1}(k_f r) - \frac{v}{k_f r}j_v(k_f r)} \tag{3.138}$$

Considering that the radial component of particle velocity at the interface is continuous, i.e.:

$$\bar{\mathrm{v}}(r_0^+)\cdot e_r = \bar{\mathrm{v}}(r_0^-)\cdot e_r \tag{3.139}$$

and deriving the velocity wave that propagates in the cylindrical layer with respect to time, one can obtain:

$$-i\omega\bar{u}(r_0^+)\cdot e_r = \bar{\mathrm{v}}(r_0^-)\cdot e_r \tag{3.140}$$

It is also considered that the stress vector is continuous. Thus, the stress acting on the surface normal to the radial direction is equal to with the radial component of the pressure field at the interface, i.e.:

$$\bar{\mathrm{t}}^{(r)}(r_0^+) = -\bar{p}(r_0^-) \cdot e_r \qquad (3.141)$$

Applying Equation (3.137) in (3.141), one can write:

$$\bar{\mathrm{t}}^{(r)}(r_0^+) = -\left[\mathcal{Z}_f^{[0]}(r_0^-)\bar{\mathrm{v}}(r_0^-) \cdot e_r\right] \cdot e_r \qquad (3.142)$$

that can be rewritten in function of displacement field, as:

$$\bar{\mathrm{t}}^{(r)}(r_0^+) = -i\omega\left[-\mathcal{Z}_f^{[0]}(r_0^-)\, e_r \otimes e_r\right]\, \bar{u}(r_0^+) \qquad (3.143)$$

where the operator $\otimes$ is the cross product.

Remembering the Equation (3.100), and from Equation (3.143), it is concluded that:

$$G_0 = -\mathcal{Z}_f^{[0]}(r_0)\, e_r \otimes e_r \qquad (3.144)$$

It is observed that if the internal medium is vacuum, $\mathcal{Z}_f^{[0]}(r_0) = 0$, the $G_0 = 0$.

3.1.5
Superficial Impedance of a Multilayer Cylinder

If the cylindrical body has other outer layers, as represented in Figure 3.4, it is possible to determine the outer impedance tensor of nth layer, G_n, from tensor G_0 obtained. To this purpose, it is necessary, firstly, to analyze if the layers are only formed by homogeneous and isotropic elastic solids or there are layers composed by acoustic fluids, known as annuli, between the solid layers.

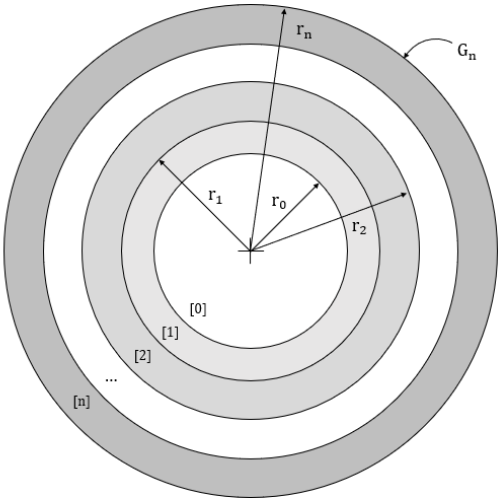

Figure 3.4 – Cylindrical body composed of isotropic and homogeneous solid multilayers interspersed with acoustic fluid.

3.1.5.1
Elastic Solid Layers

From surface impedance tensor of the cylindrical body, G_1, the reflection tensor at radius r_1 is calculated, which is obtained for the second layer similar to the first layer expressed in Equation (3.102).

$$\mathrm{R}_1 = \left[Z_1^{[2]}(r_1) - G_1\right]^{-1} \left[G_1 - Z_2^{[2]}(r_1)\right] \tag{3.145}$$

Similarly, the generalized reflection tensor for radius r_2 is calculated.

$$H(r_2) = M_1^{[2]}(r_2, r_1) R_1 M_2^{[2]}(r_1, r_2) \tag{3.146}$$

remembering that for a single layer is obtained by Equation (3.108).

Similarly, the surface impedance tensor, G_2, is calculated from Equation (3.147) below.

$$G_2 = \left(Z_1^{[2]}(r_2) H(r_2) + Z_2^{[2]}(r_2)\right) (H(r_2) + \mathrm{I})^{-1} \tag{3.147}$$

remembering that for a single layer, it is obtained by Equation (3.114).

This sequence of calculation can be repeated as a loop to the nth solid layer, finding the impedance tensor G_n.

3.1.5.2
Acoustic Fluid Layers

Figure 3.5 shows a layer composed of acoustic fluid present between the solid multilayers.

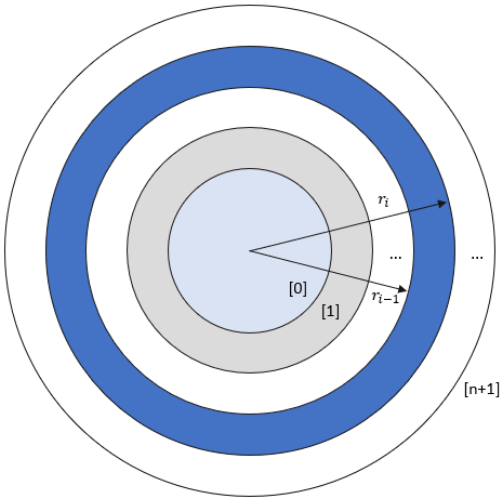

Figure 3.5 – Acoustic fluid layer between solid multilayers.

In this case, first, it is found the surface impedance tensor at the inner radius of annulus, after, it is reduced the impedance tensor to local impedance, that is a scalar, obtained by Equation (3.148).

$$\mathcal{G}_{i-1}^{-1} = (\, e_r \cdot G_{i-1}^{-1} \cdot \, e_r) \tag{3.148}$$

Known the expression that relate pressure and velocity in fluid, Equation (3.137), one can write:

$$\bar{p}(r_{i-1}) = \mathcal{G}_{i-1} \cdot \bar{\mathrm{v}}(r_{i-1}) \cdot e_r \tag{3.149}$$

Considering in this case, the outgoing and incoming wave, the velocity in radial direction can be written as:

$$\bar{\mathrm{v}}(r_{i-1}) \cdot e_r = \bar{\mathrm{v}}_1(r_{i-1}) \cdot e_r + \bar{\mathrm{v}}_2(r_{i-1}) \cdot e_r \tag{3.150}$$

Replacing the Equation (3.150) in Equation (3.149):

$$\bar{p}(r_{i-1}) = \mathcal{Z}_1^{[i]}(r_{i-1})\bar{\mathrm{v}}_1(r_{i-1}) \cdot e_r + \mathcal{Z}_2^{[i]}(r_{i-1})\bar{\mathrm{v}}_2(r_{i-1}) \cdot e_r \tag{3.151}$$

Analogous to the generalized reflection tensor, the generalized reflection scalar $\mathcal{H}(r)$ can be defined. It relates the incoming and outgoing waves at a given radial position. From the reflection scalar $\mathcal{R}_1$, one can write for the velocity in radial direction:

$$\bar{\mathrm{v}}_1(r_{i-1}) \cdot e_r = \mathcal{R}_{i-1}(r_{i-1})\bar{\mathrm{v}}_2(r_{i-1}) \cdot e_r \tag{3.152}$$

From Equations (3.149) and (3.152), it comes to:

$$\mathcal{G}_{i-1}(1 + \mathcal{R}_{i-1}) = \mathcal{Z}_1^{[i]}(r_{i-1})\mathcal{R}_{i-1}(r_{i-1}) + \mathcal{Z}_2^{[i]}(r_{i-1}) \tag{3.153}$$

so, the reflection scalar can be calculated by:

$$\mathcal{R}_{i-1} = \frac{\mathcal{G}_{i-1} - \mathcal{Z}_2^{[i]}(r_{i-1})}{\mathcal{Z}_1^{[i]} - \mathcal{G}_{i-1}} \tag{3.154}$$

and the generalized reflection scalar is calculated by:

$$\mathcal{H}(r_i) = \mathcal{M}_1^{[i]}(r_i, r_{i-1})\mathcal{R}_{i-1}(r_{i-1})\mathcal{M}_2^{[i]}(r_{i-1}, r_i) \tag{3.155}$$

Analogous to Equations (3.149), (3.151) and (3.152), one can write at the outer radius:

$$\bar{p}(r_i) = \mathcal{G}_i(r_i)\bar{\mathrm{v}}(r_i) \cdot e_r \tag{3.156}$$

$$\bar{p}(r_i) = \mathcal{Z}_1^{[i]}(r_i)\bar{\mathrm{v}}_1(r_i) \cdot e_r + \mathcal{Z}_2^{[i]}(r_i)\bar{\mathrm{v}}_2(r_i) \cdot e_r \tag{3.157}$$

$$\bar{\mathrm{v}}_1(r_i) \cdot e_r = \mathcal{H}(r_i)\bar{\mathrm{v}}_2(r_i) \cdot e_r \tag{3.158}$$

Manipulating the Equations (3.156), (3.157) and (3.158), it comes:

$$\mathcal{G}_i = \frac{\mathcal{Z}_1^{[i]}(r_i)\mathcal{H}(r_i) + \mathcal{Z}_2^{[i]}(r_i)}{1 + \mathcal{H}(r_i)} \tag{3.159}$$

and it is used in calculation of impedance tensor G_i :

$$G_i = -\mathcal{G}_i \, e_r \otimes e_r \tag{3.160}$$

3.1.6 Dispersion Equations

The wave number k_z, the frequency ω and the circumferential mode order ν are implicitly related in the dispersion equation of the problem. From this set of equations, it is possible to determine the guided waves that can propagate in the set. The circumferential mode order ν must be integer so there is no discontinuities in the displacement along the circumferential direction.

Given a value for the circumferential mode order, the dispersion diagram is defined as the set of curves formed by the pairs (ω, k_z) that represent the guided wave modes that exist in the configuration and are obtained by solving the dispersion equation.

The dispersion equation is determined from the conditions at the interface of nth layer with the external semi-infinite medium. Thus, depending on whether the external medium is a solid or a fluid, the dispersion equation differs. This setting can be seen in Figure 3.6.

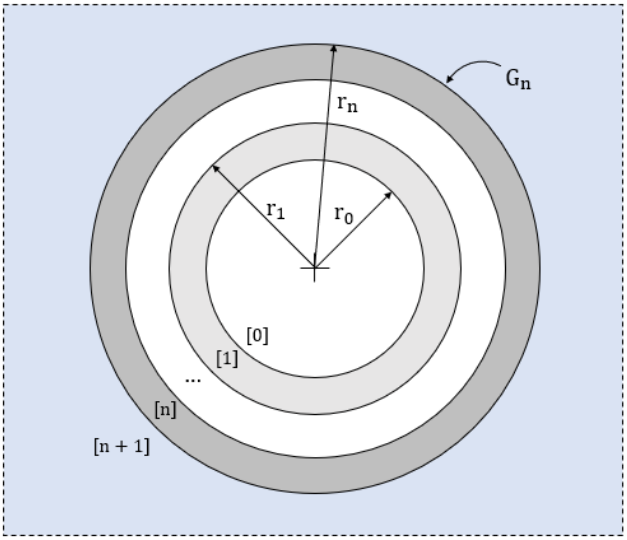

Figure 3.6 – Cylindrical body with external surface in contact with certain medium

3.1.6.1 External Medium Composed of Elastic Solid

Considerer the stress vector in radial direction as continuous, i.e.:

$$\bar{t}^{(r)}(r_n^-) = \bar{t}^{(r)}(r_n^+) \tag{3.161}$$

and the continuity of displacement at interface of the cylindrical layer with the outer medium, i.e.:

$$\bar{\mathrm{u}}(r_n^-) = \bar{\mathrm{u}}(r_n^+) \tag{3.162}$$

From the Equation (3.113), one can write to the last layer:

$$\bar{t}^{(r)}(r_n^-) = -i\omega G_n \bar{\mathrm{u}}(r_n^-) \tag{3.163}$$

Knowing that the outer medium is semi-infinite, there is only outgoing waves. The stress vector can be write as:

$$\bar{t}^{(r)}(r_n^+) = -i\omega Z_1^{[n+1]}(r_n^+)\bar{\mathrm{u}}(r_n^+) \tag{3.164}$$

From the Equations (3.163) and (3.164), it comes:

$$-i\omega \left[Z_1^{[n+1]}(r_n) - G_n \right] \bar{\mathrm{u}}(r_n) = 0 \tag{3.165}$$

Observe that the condition presented in Equation (3.165) is an eigenvalue problem, that can be solved by:

$$\det\left(Z_1^{[n+1]}(r_n) - G_n \right) = 0 \tag{3.166}$$

where det means the determinant. Equation (3.166) is the dispersion equation.

If the outer medium is vacuum, no wave will propagate on it, so:

$$Z_1^{[n+1]}(r_n) = 0 \tag{3.167}$$

In this case, the dispersion equation is:

$$\det G_n = 0 \tag{3.168}$$

3.1.6.2
External Medium Composed of Acoustic Fluid

Knowing that the pressure and the stress at a solid/fluid interface are related according to Equation (3.141), one can write:

$$\bar{\mathrm{t}}^{(r)}(r_n^-) = -\bar{p}(r_n^+) \cdot e_r \qquad (3.169)$$

From Equation (3.139), the pressure in fluid can be written as:

$$\bar{p}(r_n^+) = \mathcal{Z}_f^{[n+1]}(r_n^+)\bar{\mathrm{v}}(r_n^+) \cdot e_r \qquad (3.170)$$

and the pressure in nth layer as:

$$\bar{p}(r_n^-) = \mathcal{G}_n \cdot \bar{\mathrm{v}}(r_n^-) \cdot e_r \qquad (3.171)$$

where $\mathcal{G}_n$ can be calculate from G_n by Equation (3.148).

Replacing the equation (3.170) in (3.169), it comes:

$$\bar{\mathrm{t}}^{(r)}(r_n^-) = -\left(\mathcal{Z}_f^{[n+1]}(r_n^+)\bar{\mathrm{v}}(r_n^+) \cdot e_r\right) \cdot e_r \qquad (3.172)$$

Knowing that there is need for continuity in radial velocity component:

$$\bar{\mathrm{v}}(r_n^-) \cdot e_r = \bar{\mathrm{v}}(r_n^+) \cdot e_r \qquad (3.173)$$

Integrating the velocity, it can be written as a function of the displacement as presented in Equation (3.147).

$$-i\omega\bar{u}(r_n^-) \cdot e_r = \bar{\mathrm{v}}(r_n^+) \cdot e_r \qquad (3.174)$$

Applying the Equation (3.174) in (3.172), it is obtained:

$$\bar{\mathrm{t}}^{(r)}(r_n^-) = -i\omega\left[-\mathcal{Z}_f^{[n+1]}(r_n^+)\, e_r \otimes e_r\right] \bar{u}(r_n^-) \qquad (3.175)$$

From the Equation (3.113), one can write:

$$\bar{t}^{(r)}(r_n^-) = -i\omega G_n \bar{\mathrm{u}}(r_n^-) \tag{3.176}$$

Matching the equations (3.175) and (3.176), write the Equation (3.177).

$$-i\omega \left[\mathcal{Z}_f^{[n+1]}(r_n^+)\, e_r \otimes e_r + G_n\right] \bar{\mathrm{u}}(r_n) = 0 \tag{3.177}$$

Which can be written as:

$$-i\omega \left[\mathcal{Z}_f^{[n+1]}(r_n^+) + \mathcal{G}_n\right] \bar{\mathrm{u}}(r_n) = 0 \tag{3.178}$$

To find this condition, simply solve the dispersion equation:

$$\mathcal{Z}_1^{[n+1]}(r_n) + \mathcal{G}_n = 0 \tag{3.179}$$

Note that from Equation (3.179), for a given frequency ω and circumferential mode order ν, if the wave number k_z is real, then the fluid impedance, according to equation (3.118), occurs only when the ratio frequency ω and wave number k_z is less than the speed of sound in fluid c_f, which correspond to subsonic waves that propagate undetected along the solid/fluid interface [21].

The subsonic wave modes are acoustic guided-waves that propagate through the cylindrical layer configuration and whose velocity is lower than the external medium bulk shear velocity.

3.1.7
Determination of Displacement and Stress Vectors

From Equation (3.165), it is observed that the eigenvector associated with the null eigenvalue is the displacement $\bar{\mathrm{u}}(r_n)$. After calculating this eigenvector, it is known that it can also be written as:

$$\bar{\mathrm{u}}(r_n) = [1 + H(r_n)]\bar{\mathrm{u}}_2(r_n) \tag{3.180}$$

Inverting Equation (3.180), gives the value of the outgoing wave displacement at position r_n, presented in Equation (181).

$$\bar{\mathrm{u}}_2(r_n) = [1 + H(r_n)]^{-1}\, \bar{\mathrm{u}}(r_n) \tag{3.181}$$

From Equation (3.77), the displacement of outgoing wave, $\bar{u}_2(r_n)$, can also be written as:

$$\bar{u}_2(r_n) = M_2(r_n, r_{n-1})\bar{u}_2(r_{n-1}) \tag{3.182}$$

Known the property presented in Equation (3.78), one can write the value of $\bar{u}_2(r_{n-1})$ as:

$$\bar{u}_2(r_{n-1}) = M_2(r_{n-1}, r_n)\bar{u}_2(r_n) \tag{3.183}$$

From Equation (3.97), and from the value of $\bar{u}_2(r_{n-1})$ found in Equation (3.183), the displacement of incoming wave in position r_{n-1} can be written as:

$$\bar{u}_1(r_{n-1}) = R_{n-1}\,\bar{u}_2(r_{n-1}) \tag{3.184}$$

Knowing the displacement wave, $\bar{u}$, in position r_{n-1}, it can be calculated by the sum of incoming and outgoing waves found, as shown in Equation (3.185).

$$\bar{u}(r_{n-1}) = \bar{u}_1(r_{n-1}) + \bar{u}_2(r_{n-1}) \tag{3.185}$$

From the property presented in Equation (3.79), and from Equations (3.183) and (3.184), where it was determined the values of $\bar{u}_1(r_{n-1})$ and $\bar{u}_2(r_{n-1})$, one can write in Equation (3.186) the expression to $\bar{u}(r)$.

$$\bar{u}(r) = M_1(r, r_{n-1})u_1(r_{n-1}) + M_2(r, r_n)u_2(r_n) \tag{3.186}$$

where:

$$\bar{u}(r) = \bar{u}_1(r) + \bar{u}_2(r) \tag{3.187}$$

and r is defined in range of:

$$r_{n-1} < r < r_n \tag{3.188}$$

From the Equations (3.83) and (3.94) obtained, one can write the stress vectors $\bar{t}^{(r)}$ and $\bar{t}^{(z)}$ as:

$$\bar{t}^{(r)}(r) = -i\omega[Z_1(r)\bar{u}_1(r) + Z_2(r)\bar{u}_2(r)] \tag{3.189}$$

$$\bar{\mathrm{t}}^{(z)}(r) = -i\omega[Y_1(r)\bar{\mathrm{u}}_1(r) + Y_2(r)\bar{\mathrm{u}}_2(r)] \qquad (3.190)$$

Thus, by knowing the displacement expression as a function of the radial position only, $\bar{\mathrm{u}}(r)$, in Equation (3.187), it is possible to determine the stress vectors $\bar{\mathrm{t}}^{(r)}(r)$ and $\bar{\mathrm{t}}^{(z)}(r)$ also as a function of radial position only from Equations (3.189) and (3.190).

3.2
Circumferential Modes

The circumferential mode order, $\boldsymbol{\nu}$, presented in the harmonic functions of displacement, $\boldsymbol{u}$, stress tensor, $\boldsymbol{\sigma}$, pressure, $\boldsymbol{p}$, and particle velocity, $\mathbf{v}$, is an integer representing the cylindrical harmonics. In the case of a monopole circumferential distribution, $\nu = 0$, for a dipole, $\nu = 1$, for a quadrupole, $\nu = 2$, for a hexapole, $\nu = 3$, for a octupole, $\nu = 4$, for a decapole, $\nu = 5$, for a dodecapole (12-pole), $\nu = 6$. Thus, 2ν is the number of poles in a cylindrical multipole distribution – see, for instance, [71]. A monopole distribution is the typic axisymmetric excitation of the source, where the excitation energy is distributed equally in all directions. In this thesis only the axisymmetric approach will be considered in the analysis. Ideally, the circumferential order-mode is selected by the nature of the excitation source located in the center of wellbore. That is, if a source is axisymmetric, that is, a monopole, then ideally, only $\nu = 0$ modes exist; if the source is a dipole, then one, then ideally, only $\nu = 1$ modes exist, and so on.

Figure 3.7 shows the circumferential distribution for each cylindrical harmonic.

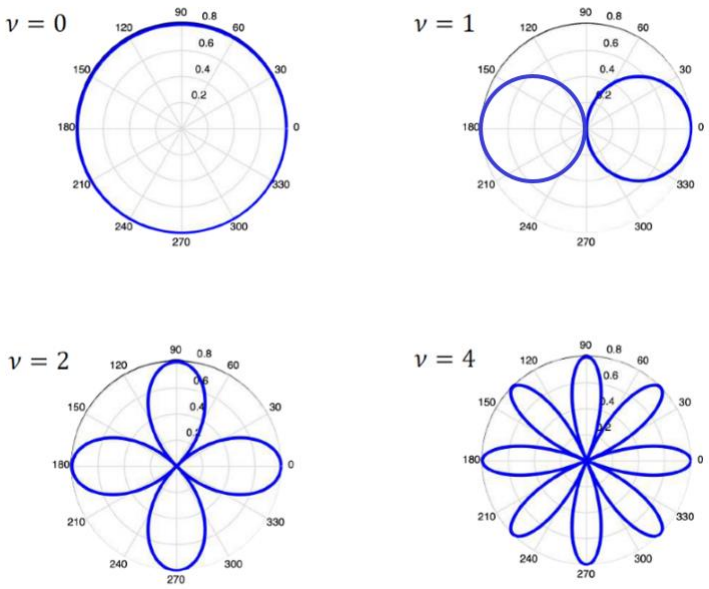

Figure 3.7 - Circumferential distribution for cylindrical harmonics.

3.3
Power Flow (Poynting Vector)

After the pairs (ω, k_z) that satisfy the dispersion equation are found, the elastic and acoustic fields within the layered cylinder are obtained for each pair and the axial distribution of acoustic intensity can be calculated. These results are often presented as an averaged value during one period $2\pi/\omega$. The averaged power flow in the axial direction corresponds to the averaged axial component of the Poynting Vector; see, for instance, [72] or [73].

The average axial component of the Poynting Vector is then written as [72]:

$$\langle \mathcal{P}_z(r) \rangle_T = \frac{1}{2} \mathrm{Re}\{-i\omega\, \hat{\boldsymbol{t}}(r) \cdot \hat{\boldsymbol{u}}^*(r)\} \qquad (3.191)$$

in the case of an elastic layer, or

$$\langle \mathcal{P}_z(r) \rangle_T = \frac{1}{2} \mathrm{Re}\{\hat{p}(r)\, \hat{v}_r^*(r)\} \qquad (3.192)$$

in a fluid layer, where the asterisk means the complex conjugate and $\hat{v}_r$ is the radial component of the particle velocity in the fluid.

Exact, analytical results obtained through the algorithm proposed by Braga et al, [21] for the different non-defective and cement-defective configurations, single-casing and through-tubing, are presented and discussed in Chapter 2. Typically, the dispersion spectrum may be plotted in four different ways, namely: (i) frequency (f) or angular frequency (ω) *vs*. the axial wavenumber (k_z); (ii) axial wavelength $(\lambda = 2\pi/k_z)$ *vs*. frequency $(f$ ou $\omega)$; (iii) axial phase velocity $(c = \omega/k_z)$ *vs.* frequency $(f$ ou $\omega)$; or (iv) slowness, which is the inverse of phase velocity $(s = k_z/\omega)$ *vs.* frequency $(f$ ou $\omega)$.

The dispersion spectrum, in its four different representations, is composed of multiple branches, each one being a curve corresponding to a specific wave-mode (subsonic or leaky modes) and have particular energy, or acoustic intensity distributions across the wellbore, being in different extent susceptible to defects present in the cement sheath as shall be discussed later.

3.4
Group Velocity

"Group velocity is associated with the propagation velocity of a group of waves of similar frequency" [69]. Another term used for group velocity is velocity of wave packets [74] because represent the velocity of wave packets, i.e., the energy propagation velocity.

The group velocity is given by the derivative of the frequency with respect to the wavenumber:

$$c_g = \frac{\Delta\omega}{\Delta k} \qquad (3.199)$$

From the Christoffel Equation, which v is the fase velocity defined by $v = \omega/k$ and c_{ijkl} is the stiffness matrix.

$$c_{ijkl}n_j n_l - \rho v^2 \delta_{ik} = 0 \tag{3.200}$$

Multiplying the determinant of the Equation (3.200) by k^2 gives:

$$\det\left(c_{ijkl}kn_j kn_l - \rho k^2 v^2 \delta_{ik}\right) = \det\left(c_{ijkl}k_j k_l - \rho\omega^2 \delta_{ik}\right) = 0 \tag{3.201}$$

from Equation (3.201), one can write:

$$\det\left(c_{ijkl}n_j n_l - \rho v^2 \delta_{ik}\right) = 0 \tag{3.202}$$

$$\det\left(c_{ijkl}k_j k_l - \rho\omega^2 \delta_{ik}\right) = 0 \tag{3.203}$$

one may conclude that ω varies with k_j in the same way that v varies with n.

$$c_g = \frac{\partial\omega}{\partial k_i} = \frac{\partial v}{\partial n_i} \tag{3.204}$$

Let the mechanical energy density be defined by the sum of the kinetic energy density $\langle k \rangle$ and the deformation energy density $\langle w \rangle$. The energy propagation velocity, c_E, is defined as the ratio of the average power flow density $\langle P \rangle$ to the average mechanical energy density, which can be expressed by the Equation (3.205):

$$c_E = \frac{c_{ijkl}n_j p_k p_i^*}{\rho v p_k p_k^*} \tag{3.205}$$

which p is the pressure vector and n the polarization.

Multiplying both sides of the Christoffel Equation by the pressure vector p_i^* and deriving in relation to the polarization n_i:

$$\frac{\partial}{\partial n_i}\left(c_{ijkl}n_j n_l p_k p_i^*\right) = \frac{\partial}{\partial n_i}\left(\rho v^2 p_i p_i^*\right) \tag{3.206}$$

$$2c_{ijkp}n_j p_k p_i^* = 2\rho v p_i p_i^* \frac{\partial v}{\partial n_i} \tag{3.207}$$

From Equation (3.204), the group velocity can be write as:

$$c_g = \frac{\partial v}{\partial n_i} = \frac{c_{ijkp}n_j p_k p_i^*}{\rho v p_i p_i^*} \tag{3.208}$$

Therefore, it is observed that the group velocity is the energy propagation velocity. In the presented case the group velocity is the velocity in which energy propagates through the pipe (waveguide).

$$c_g = c_E \tag{3.209}$$

4
Algorithm for the General Case

There is no analytical solution for the dispersion equations derived in Chapter 3. Therefore, a numerical approach is necessary. In this Chapter, a numerical procedure used to solve the dispersion equations and consequently to obtain the dispersion curves is discussed. Figure 4.1 shows a schematic of the numerical approach used.

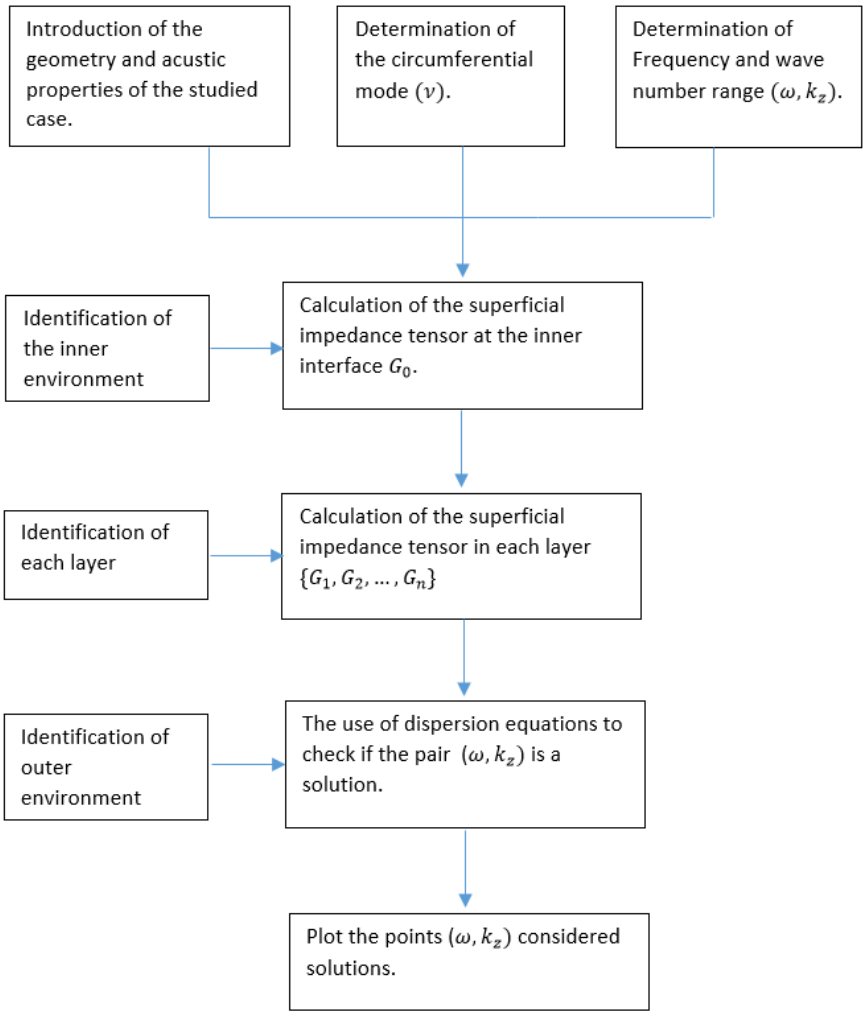

Figure 4.1 – Scheme of the numerical approach

It is possible to observe that the numerical program developed is based on the calculation of the surface Impedance tensor in the nth layer for various

frequency and wave numbers values previously stipulated. The program tests whether the impedance tensor calculated for each pair (ω, k_z) satisfies the dispersion equation (as seen in section 4.4) and if so, plots that point, thus obtaining the dispersion curves. Figure 4.2 shows the pseudocode used.

```
Coordinates of interfaces: r_0, r_1, r_2, ..., r_n
Definition of the layers and environments: 1 − Fluido, 2 − Sólido, 3 − Vácuo
Layers and environment properties:
      Fluid (ρ, c)
      Solid (λ, μ, ρ)
      Vacuum (ρ = 0)
Propagation parameters: (ω, k_z, ν)
Calculation of k_f, Z_f^[0](r_0) e G_0

For ω:A:B
For k_z:C:D

For i=1:n
If the layer is solid, calculate:
k_L, k_T, Z_1^[i], Z_2^[i]
R_{i−1}, M_1^[i] e M_2^[i]
H(r_i), G_i
If the layer is fluid, calculate:
k_f, G_{i−1}, Z_1^[i], Z_2^[i]
R_{i−1}, M_1^[i], M_2^[i]
H(r_i), G_i, G_i
end

Is the outer environment solid, fluid or vacuum?
If the corresponding dispersion equation is a solution,
store the pair (ω, k_z).

end
end
```

Figure 4.2 – Pseudocode used in the numerical program

Section 4.1 to 4.4 aim to explain each step of the presented pseudocode.

4.1
Input Data

In order to obtain the dispersion curves for the studied case, initially, the interface radii between the cylindrical layers $(r_0, r_1, r_2, \dots, r_n)$ are introduced as input data. For each layer, its composition is informed to the program, i.e., if the layer is an elastic solid or an acoustic fluid as well as its acoustics properties. If the layer is an annulus composed by an acoustic fluid the density, ρ_f, and the velocity, c_f,

is informed, but if the layer is an elastic solid, then Lamé constants, λ and μ, and the density, ρ, are needed.

Next, the acoustic properties of the inner and outer media are also informed. If the medium is vacuum only the density is informed and considered null, $\rho = 0$, as is further explained in Section 4.2. After this, the circumferential mode order, ν, is informed.

To be able to perform the proper calculation, two vectors are created, one for the frequency, ω, and other to the wave number, k_z. The range of these vectors determines the graphic window of the dispersion curves. The precision of curves is determined by the step of vectors. For each pair (ω, k_z), a certain value of G_0 and consequently of G_n is obtained as will presented in Sections 4.2 and 4.3, storing in a vector.

Table 4.1 – Input Parameters used to calculate the Impedance tensor and analyze the solution condition

Input Parameters
Introduction of geometry $(r_0, r_1, r_2, \dots, r_n)$
Identification of environment (1 - Fluido, 2 - Sólido, 3 - Vácuo)
Introduction of acoustic properties (λ, μ, ρ, c)
Determination of circumferential mode order (ν)
Determination of frequency and wave number range (ω, k_z)

4.2
Inner Superficial Impedance Tensor G_0

Before calculating the superficial impedance, G_0, the composition of the inner and outer media is identified, i.e., if it is an acoustic fluid, an elastic solid or vacuum. In both cases, it is used the same algorithm that consist of calculation of k_f from the input parameters, follow by the calculation of the local impedance in fluid, $Z_f^{[0]}(r_0)$ and the impedance tensor, G_0. However, if the inner medium is vacuum, k_f is not calculated and $\rho_f = 0$ is used so that the tensor G_0, in this case, is null as presented by Equations (4.1), (4.2) and (4.3), as follows:

- *Inner medium is a fluid:*

$$k_f = \begin{cases} \left(\frac{\omega^2}{c_f^2} - k_z^2\right)^{1/2}, & \frac{\omega}{c_f} \geq k_z \\ i\left(k_z^2 - \frac{\omega^2}{c_f^2}\right)^{1/2}, & \frac{\omega}{c_f} < k_z \end{cases} \tag{4.1}$$

- *Inner medium is vacuum,* $\rho_f = 0$

$$Z_f^{[0]}(r_0) = i\frac{\rho_f \omega}{k_f}\frac{j_\nu(k_f r)}{j_{\nu-1}(k_f r) - \frac{\nu}{k_f r} j_\nu(k_f r)} \tag{4.2}$$

$$G_0 = -Z_f^{[0]}(r_0) n \otimes n \tag{4.3}$$

4.3
Superficial Impedance Tensor for the Cylindrical Multilayer G_n

From G_0, the composition of the next layer is checked, i.e., whether it is a solid layer or an acoustic fluid annulus. If it is solid, k_L and k_T are calculated from the acoustic properties of the medium and the local impedance $Z_1(r)$ e $Z_2(r)$ from the matrices presented in the appendix. This calculates the reflection tensor R_0. Obtaining the propagation matrices M_1 and M_2, one can find the generalized reflection tensor $H(r)$, and finally the impedance tensor on the next surface, G_1.

If the layer is a fluid, k_f is calculated from the acoustic properties of the medium. The impedance tensor G_0 is converted into a scalar, obtaining $\mathcal{G}_0$. This value is used to find the reflection constant $\mathcal{R}_0$, and consequently the generalized reflection constant $\mathcal{H}(r)$. Based on the calculation of the local impedance $Z_1(r)$ and $Z_2(r)$, presented in Chapter 3, the surface impedance scalar $\mathcal{G}_1$ is found and finally converted to the surface impedance tensor G_1.

This same calculation is repeated in a loop for the next layers, always using the impedance tensor calculated on the inner surface, (G_{j-1}) to obtain impedance tensor calculated on the outer surface of the next layer (G_j). This algorithm is presented by the sequence of Equations (4.4) to (4.14).

Repet to $j = 1{:}\,n$

- *If the layer is an elastic solid:*

$$k_m = \begin{cases} \left(\frac{\omega^2}{c_m^2} - k_z^2\right)^{1/2}, & \frac{\omega}{c_m} \geq k_z \\ i\left(k_z^2 - \frac{\omega^2}{c_m^2}\right)^{1/2}, & \frac{\omega}{c_m} < k_z \end{cases} \quad m = L, T \tag{4.4}$$

$$Z_\alpha(r) = \frac{i}{\omega} L_\alpha(r) A_\alpha^{-1}(r) \tag{4.5}$$

$$R_{j-1} = \left[Z_1^{[j]}(r_{j-1}) - G_{j-1}\right]^{-1}\left[G_{j-1} - Z_2^{[j]}(r_{j-1})\right] \tag{4.6}$$

$$H(r_j) = M_1^{[j]}(r_j, r_{j-1}) R_{j-1} M_2^{[j]}(r_{j-1}, r_j) \tag{4.7}$$

$$G_j = \left[Z_1^{[j]}(r_j) H(r_j) + Z_2^{[j]}(r_j) \right] \left[I + H(r_j) \right]^{-1} \tag{4.8}$$

- *If the layer is an acustic fluid:*

$$k_f = \begin{cases} \left(\frac{\omega^2}{c_f^2} - k_z^2 \right)^{1/2}, & \frac{\omega}{c_f} \geq k_z \\ i \left(k_z^2 - \frac{\omega^2}{c_f^2} \right)^{1/2}, & \frac{\omega}{c_f} < k_z \end{cases} \tag{4.9}$$

$$\mathcal{G}_{i-1} = \left(n \cdot G_{j-1}^{-1} n \right)^{-1} \tag{4.10}$$

$$\mathcal{R}_{j-1} = \frac{\mathcal{G}_{j-1} - \mathcal{Z}_2^{[j]}(r_{j-1})}{\mathcal{Z}_1^{[j]} - \mathcal{G}_{j-1}} \tag{4.11}$$

$$\mathcal{H}(r_j) = \mathcal{M}_1^{[j]}(r_j, r_{j-1}) \mathcal{R}_{j-1}(r_{j-1}) \mathcal{M}_2^{[j]}(r_{j-1}, r_j) \tag{4.12}$$

$$\mathcal{G}_j = \frac{\mathcal{Z}_1^{[j]}(r_j) \mathcal{H}(r_j) + \mathcal{Z}_2^{[j]}(r_j)}{1 + \mathcal{H}(r_j)} \tag{4.13}$$

$$G_j = -\mathcal{G}_j n \otimes n \tag{4.14}$$

4.4 Determination of Dispersion Curves

From the impedance tensor, G_n, obtained for each pair (ω, k_z), the appropriate dispersion equation is used to verify if the pair (ω, k_z) is a solution. Depending on whether the outer medium is vacuum, fluid or solid, a specific dispersion equation is used.

- *If the outer medium is vacuum*

$$det(G_n) = 0 \tag{4.15}$$

- *If the outer medium is an elastic solid*

$$det\left(Z_1^{[n]} - G_n\right) = 0 \tag{4.16}$$

- *If the outer medium is an acoustic fluid*

$$\mathcal{G}_n = (n \cdot G_n^{-1} n)^{-1} \tag{4.17}$$

$$Z_1^{[n]}(r_n) + \mathcal{G}_n = 0 \tag{4.18}$$

With the *fzero* function of the *MATLAB*® software [75], it is seek the pairs (ω, k_z) are solutions, storing them. Finally, to obtain the dispersion curves, just plot the points (ω, k_z) identified as solutions. This part from algorithm is presented by the sequence of equations from (4.15) to (4.18).

4.5
Power Flux Algorithm

To obtain the energy distribution of the wave that propagates through the well, first of all, it is informed if the external media is fluid or solid. If it is solid, from the surface impedance tensor, G, found at the interfaces, it is possible to obtain the displacement of the outgoing wave by finding the eigenvalues of the matrix G_j. Thus using Equation 3.110, the displacement can be obtained. If the external media is a fluid, the tensor vector is stipulated considering the pressure as unitary value. In this case the displacement is obtained from this stipulated tensor vector. Knowing the displacement and the tensor vector at all radial positions, i.e., $r_0 < r < r_n$, the pointing vector can be calculated and plot.

Figure 4.3 present a pseudocode used in the numerical program.

```
If external medium is solid
Eigenvalues and Eigenvectors of G
[V,D] = eig(G)
V – matrix which columns are the eigenvectors
D – matrix which diagonal are the eigenvalues
[eig0,m] = min(abs(diag(D)));
Calculate the displacement of outgoing wave
u_r1= V(:,m);
Calculate the displacement from propagation matrix
u = M_r*u_r1;
Calculate the local impedance matrix in radial (Z_r) and
longitudinal (Y_r) direction
Calculate the tensor vector in both directions
t_r = -1i*w*Z_r*u;
t_z = -1i*w*Y_r*u;
Calculate the Poynting Vector
P_r = (1/2)*real(t_r'*conj(-1i*w*u));
P_z = (1/2)*real(t_z*conj(-1i*w*u));

If external medium is fluid
Calculate the displacement of outgoing wave
t_r1= -1*[1;0;0];
u_r1 = (1i/w) *invG*t_r1;
Calculate the velocity of outgoing wave:
vr_r1=-1i*w*(u_r1);
Calculate (vr_r) from (vr_r1) and local Impedance in
fluid (Zf_r)
Calculate the pressure:
p_r = Zf_r.*vr_r;
Calculate the velocity in Shear and longitudinal
direction, (vt_r) and  (vz_r)
Calculate the Poynting Vector
P_r = (1/2) *real (p_r.*conj (vr_r));
P_z = (1/2) *real (p_r.*conj (vz_r));

[R, T] = meshgrid (r, theta);
X = R.*cos (T) /pi;
Y = R.*sin (T) /pi;
Z = zeros(size (X));

for j = 1: size(theta,2)
    for i = 1: size(r,2)
        Z (j, i) = (P_z (i) /Pbar). *cos (2*nu*theta
(j));
    end
end
figure; surf (X*d, Y*d, -Z);
```

Figure 4.3 – Pseudocode used in the Power Flux Plot

5
Results

In this chapter, analytical results obtained with the methods discussed in Chapters 3 and 4 are presented. Section 5.1 validates the developed code with known results. Section 5.2 presents the well configuration studied. Section 5.3 briefly revisits the types of defective cement layers discussed in Chapter 2, describing in greater detail their main characteristics concerning the models of defects analysed. Then, for both the single-casing and through-tubing cases, results obtained through the analytical approach are presented in Section 5.4.

5.1
Validation Cases

To validate the developed analytic-numerical routine, it was used cases from the literature. The developed code was applied in these cases and consequently the obtained dispersion curves were compared with the ones presented in the literature.

The simplest case presented in the literature [20] is the analytical dispersion curves for a homogeneous cylindrical steel body with vacuum inside and outside. The order of circumferential mode used in this case is one, which may be generated by a dipole source excitation inside the pipe. Figure 5.1 shows the cylindrical body described above.

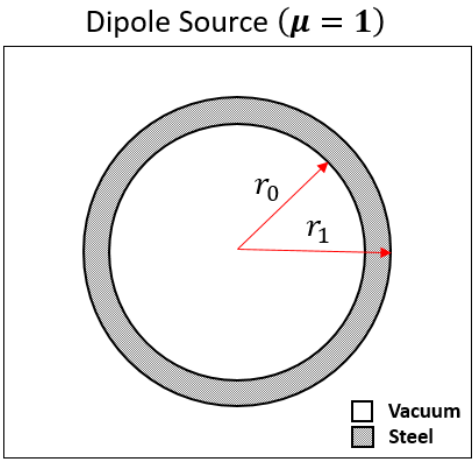

Figure 5.1 – Representation of the case. A single cylinder layer with a dipole excitation source.

The calculated dispersion curves for frequency versus dimensionless wavelength is shown in Figure 5.2(a). Figure 5.2(b) presents the reference

dispersion from [20] for comparison. The same Axis scale and the dimension of variable used in [20] was adopted in order to allow straightforward comparison of both curves' sets.

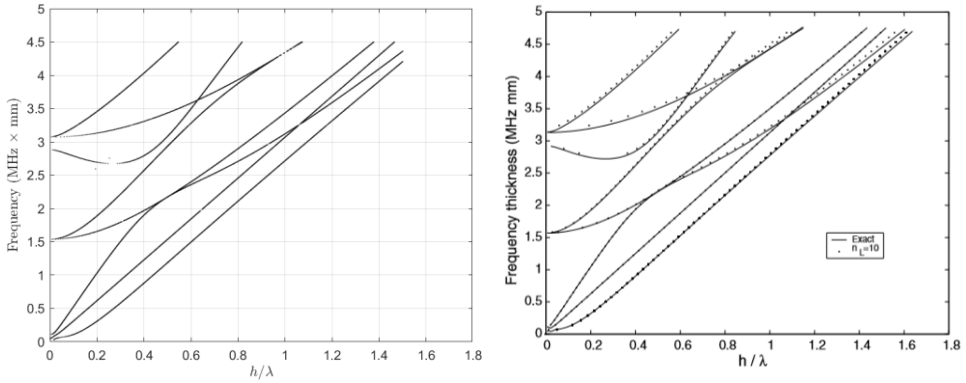

(a) (b)

Figure 5.2 (a) Frequency by dimensionless wavelength obtained using the analytical code proposed in this work, where h is the thickness of the cylindrical layer and λ is the wavelength. (b) Frequency by dimensionless wavelength obtained in [20] the article. The analytical solution is presented in continuous curves [20].

The analytical curves presented in Figure 5.2(b) showed great similarity with the dispersion curves obtained by the developed code. This proves the code's effectiveness to solve problems with this type of configuration, i.e., a single cylindrical body with vacuum inside and outside.

Similar to the previous case, Li et al. [76] also proposes the analytical solution for a case involving a single cylindrical layer, however composed by a high-density polyethylene (HDPE). Furthermore, in this case water is used as the inner medium. The order of circumferential mode used is zero, which represents a monopole excitation source. Figure 5.3 illustrates the described case.

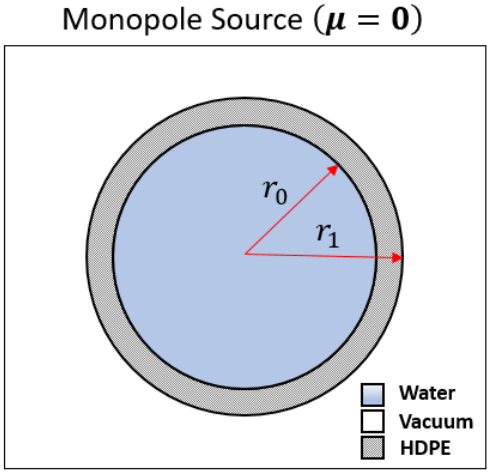

Figure 5.3 - Representation of the problem involving a sigle cylindrical layer with vacuum outside and water inside for a monopole excitation source.

The phase velocity dispersion curves were calculated and compared with the respective reference, as can be seen in Figure 5.4 (a) and (b). Moreover, in this same chart, the longitudinal wave velocities, i.e., the P wave velocity and the shear wave velocity for each media present in this configuration were plotted. Each mode is indicated by a pair of indexes referred to the circumferential mode order

and the group mode order, respectively. It is possible to verify that the developed analytical code was effective in obtaining the same dispersion curves, further validating the code.

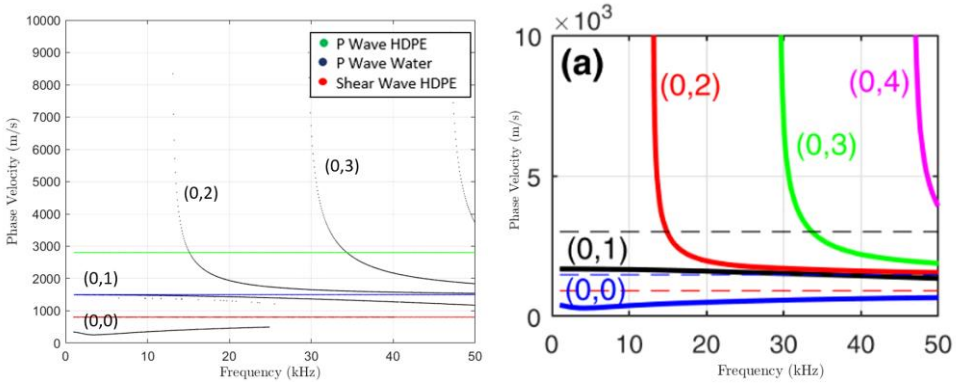

Figure 5.4 – (a) Phase velocity by frequency obtained by the analytical model proposed in this work. The colored curves represent the bulk waves velocities in each media presented in this configuration (b) Phase velocity by frequency used to validate the analytical model presented in [76]

Braga et al. [21] presented another similar case, however, with water as outside fluid. Figure 5.5 shows a representation of this case.

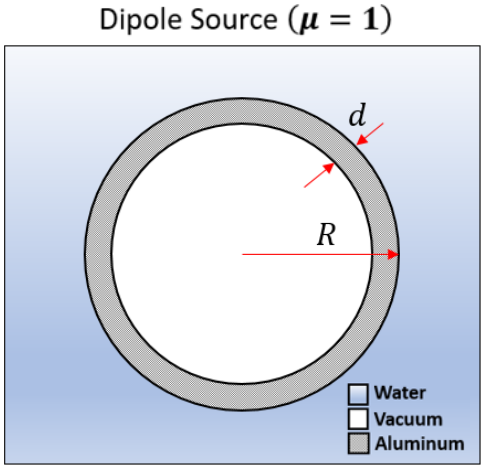

Figure 5.5 – Representation of the case involving a single cylindrical layer with vacuum in the inner media, water in the outer media and for a dipole excitation source.

The Figure 5.6 (a) and (b) shows the dispersion curves calculated here and from literature, respectively. The dimensionless wave number is used and the value of the external radius was varied. In Figure 5.6, *R/d* is a dimensionless parameter, where *R* is the outer radius and *d* is the thickness of layer.

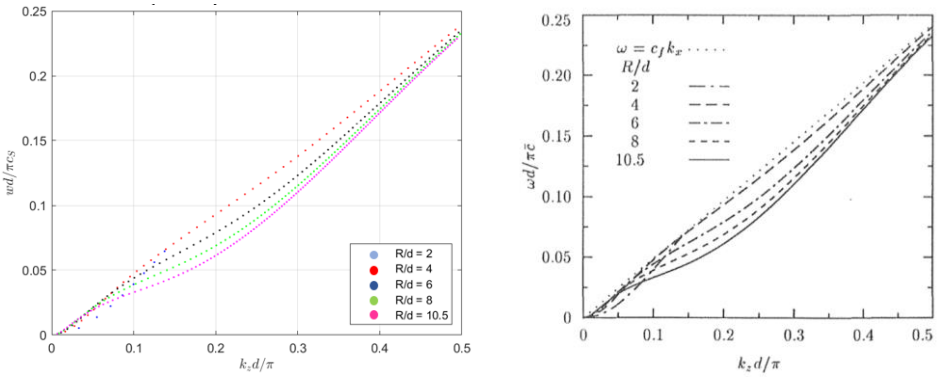

(a) (b)

Figure 5.6 – (a) Plot of the dimensionless frequency by the dimensionless wave number obtained by the analytical model developed in this work. Each colored curve stands for a given ratio between the outer radius, R, and the thickness, d, of the cylindrical layer. (b) Plot of the dimensionless frequency by the dimensionless wave number used to validate the analytical model extracted from [21].

Liu et al. [49], used either analytical or numerical solution, through finite element method to treat a cylindrical steel body with water in inner and outer media. Figure 5.7 shows the representation of this problem.

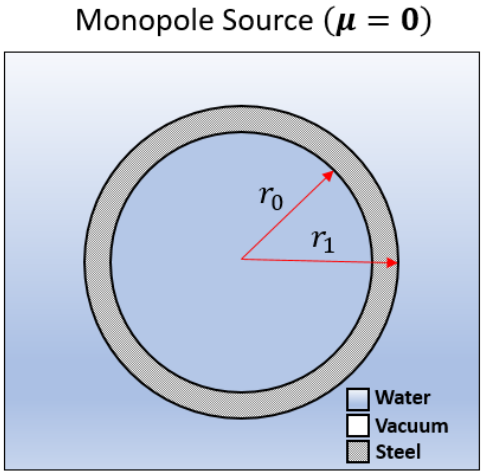

Figure 5.7 - Representation of the problem of a single cylindrical layer with water in the inside and outside media for a dipole excitation source.

Slowness curves obtained by the proposed method and from literature is shown in Figure 5.8 (a) and (b), respectively. One can observe that the developed code did not acquire all the curves obtained in literature. Only the top slowness curve, over 200 $\mu s/ft$ was obtained. This occurs because the program solves only the subsonic modes, considering only the Stoneley waves. However, the subsonic mode obtained by developed analytical program showed good agreement with results from literature, validating the problem for subsonic modes.

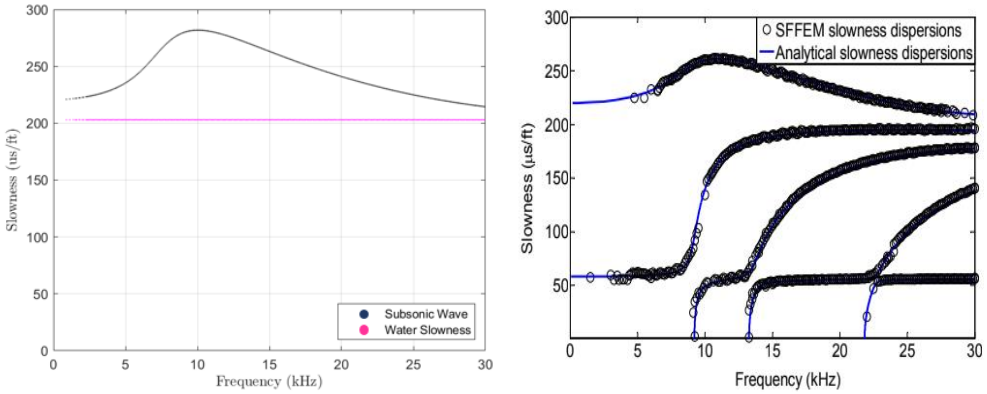

(a) (b)

Figure 5.8 – (a) Slowness curve obtained by the analytical model. The magenta line represents the slowness of the body wave that propagates in water. (b) Slowness curve from literature [49].

Braga et al. [20] present analytical results for a configuration involving three coupled cylindrical layers with the inner and the outer media being vacuum. Figure 5.9 shows a representation of this case indicating the materials used in each cylindrical layer. The materials used were aluminum, steel and cooper. Figure 5.10 (a) and (b) presents the plot for frequency versus dimensionless wavelength obtained by the developed analytical program and literature, respectively. Observing both charts present in Figure 5.10(a) and Figure 5.10(b), it is possible to identify great similarity between the results. This last case validates the code for multi-layered structures.

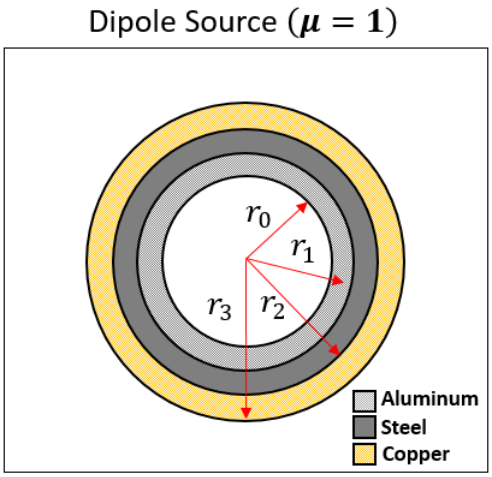

Figure 5.9 - Representation of a multiple cylindrical layers case, with vacuum inside and outside.

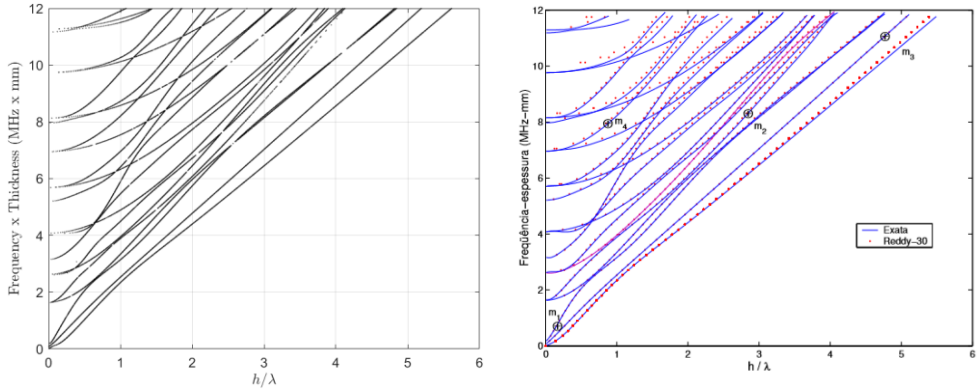

(a) (b)

Figure 5.10 – (a) Frequency by the dimensionless wavelength obtained by the analytical model developed in this work, where h represents the thickness of the inner cylindrical layer. (b) Frequency by the dimensionless wavelength used for model validation The blue lines present the exact solution while the red dots are an approximation, both extracted from [20].

Once the code was validated with several known results it was used to investigate the dispersion curve in the scenario of interest.

5.2
Well Configuration

All results presented in this chapter were obtained for a well completed with a 9 5/8” (0.244 m) casing and 4 ½” (0.102 m) tubing, both made of carbon steel and respectively with nominal weights of 53.5 lb/ft (7.40 kg/m) and 12.6 lb/ft (1.74 kg/m) and density 7800 kg/m³. Tubing and A-annulus are filled with water. Thickness of the cement layer was considered at 0.5” (12.7 mm). Properties of the surrounding rock formation were those for sandstone [77] [78] [79] [80]. Table 5.2 and 5.3 list geometries and acoustic properties for the modeled well with the non-defective cement layer. Changes in geometry and properties present in Table 5.2 to simulate defects in the cement layer are discussed in Section 5.2. In all cases, tubing, casing and cement layers are concentric and with uniform thicknesses. In this work, the analysis considered only monopole (axisymmetric) sources, i.e., $v = 0$.

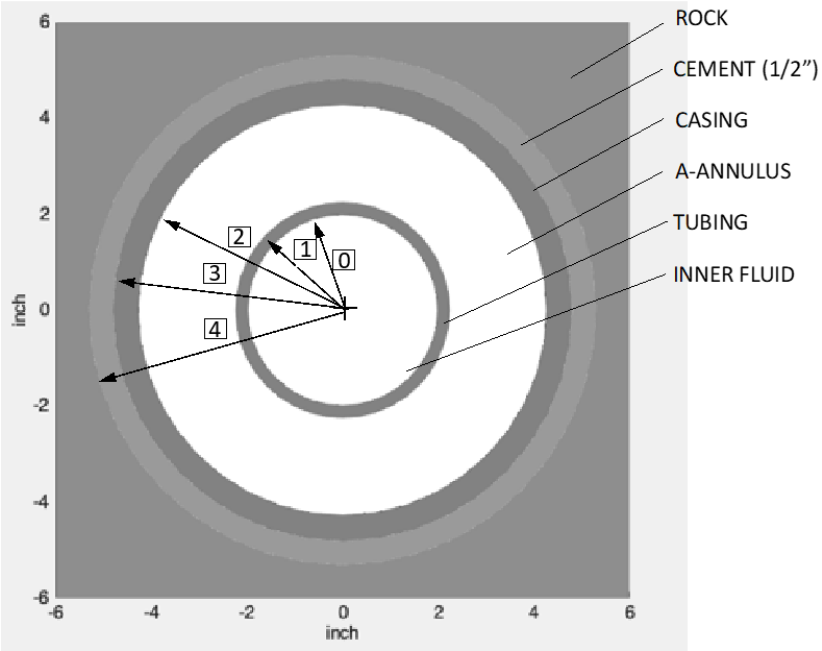

Figure 5.11 - Well representation for the case studies.

Table 5.1 – Reference model of well used in North Sea [10]

WELL	CASING OD	CASING WEIGHT	CASING ID	TUBING OD	TUBING WEIGHT	TUBING ID	CEMENT THICKNESS
	9.625''	53.5 lb/m	8.535''	4.500''	12.6 lb/m	3.958''	0.5''
	0.244 m	7.40 kg/m	0.217 m	0.102 m	1.74 kg/m	0.100 m	0.013 m

Table 5.2 – Acoustic Properties for the case Studies (non-defective cement layer)

LAYER	$\rho\ (kg/m^3)$	$\lambda\ (Pa)$	$\mu\ (Pa)$	cp (m/s)	cs (m/s)
Steel	7800	1.10×10^{11}	8.00×10^{10}	5883	3203
Water	1000	2.25×10^{9}	0.00	1500	0
Cement	1800	5.43×10^{9}	5.39×10^{9}	3000	1730
Rock	2300	1.43×10^{10}	1.62×10^{10}	4500	2650

Table 5.3 – Base Geometry for the case Studies (non-defective cement layer)

TUBING 4 1/2 - CASING 9 5/8			
INTERFACE	RADIUS (mm)	RADIUS (Inch)	DIAM. (Inch)
r_0	50.3	1.980	3.96
r_1	57.2	2.252	4.50
r_2	108.4	4.268	8.54
r_3	122.2	4.811	9.62
r_4	134.9	5.311	10.62

5.3
Case Studies: Description

A deffective cement layer was simulated by introducing a thin concentric cylindrical layer of water or by modifying the acoustic (acoustic impedance) of the cement layer. Different cases were investigated by changing thickness, position relative to the cement interfaces, or acoustic impedance of the defective layer. In all cases, the thickness of the cement layer, or rather the distance between the casing's outer surface to the inner surface of the rock formation, was kept fixed at

0.5” (0.013 m). Table 5.4 summarizes the defects that were simulated. The abbreviation in parentheses in the first column is used throughout this chapter to refer to the defects.

Table 5.4 – Simulated defects for single-casing and through-tubing configurations

Defect	Position within Cement Layer	Defective Layer Thickness	Number of Layers	Defective Layer Impedance
Channeling (CH)	Center	1%, 5%, 10%, 20%, 40%, 60%	Single	Fluid (Water)
Cement Quality (CQ)	Entire Cement Layer	0.5” (0.013 m)	Single	1.0 MRayl, 2.0 MRayl, 3.0 MRayl, 5.4 MRayl
Inner Debonding (SC)	Casing (Steel)/Cement Interface	20%, 40%, 60%	Single	Fluid (Water)
Outer Debonding (CR)	Cement/Rock Interface	20%, 40%, 60%	Single	Fluid (Water)

5.3.1 Non-Defective Cement

The first case modeled (Figure 5.12) is the non-defective cement layer, whose results are taken as reference to compare the effects of the several defective cement layers on the propagation characteristics of guided acoustic waves. The influence of a detective layer may be noticed in the dispersion curves of the guided waves in the wellbore.

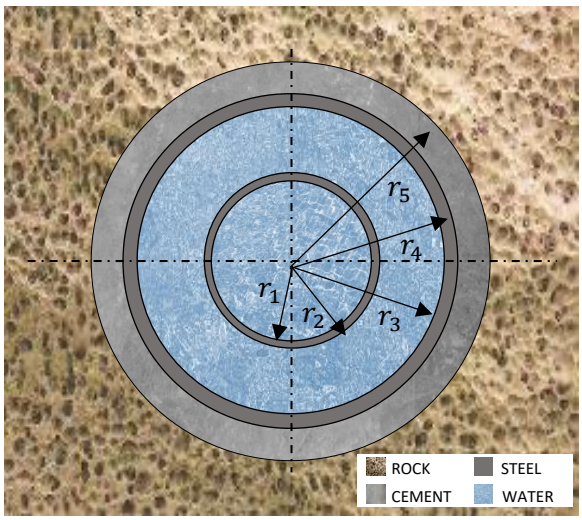

Figure 5.12 - Non-defective configuration.

5.3.2 Channeling (CH)

Channeling is modeled here by introducing a thin cylindrical layer with modified acoustic impedance within the cement layer (see Figure 5.13) whose thickness is kept unchanged at 0.5” (0.013 m). The acoustic properties of water were used in the channel modeling. The boundary conditions at the inner and outer

radius of the channeling are continuous radial component of the stress and particle velocity components. Also, at these interfaces, shear stresses vanish and axial and circumferential components of the particle velocity are allowed to be discontinuous. Six different cases were implemented, with the channel thickness varying from 1%, 5%, 10%, 20%, 40% and 60% of the cement layer thickness.

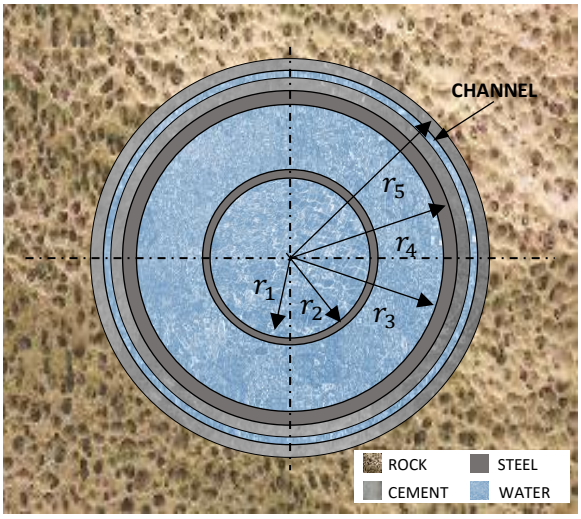

Figure 5.13 - Channeling in the cement layer (CH).

5.3.3
Cement Quality (CQ)

The model for low-quality (degraded) cement has been implemented by uniformly reducing the specific P-wave impedance of the cement layer (Figure 5.14). The P-wave impedance of an elastic medium is defined as the product of its density (ρ) and P-wave speed (c_P):

As reported in Table 5.2, for the non-defective cement, its density and P-wave speed are $\rho = 1{,}800$ kg/m^3 and $c_P = 3{,}000$ m/s. Therefore, its specific P-wave impedance is 5.4 MRayl. In order to simulate the defect, the impedance was reduced to 1.0 MRayl, 2.0 Mrayl and 3.0 Mrayl, by altering only its density. Hence, three cases were simulated.

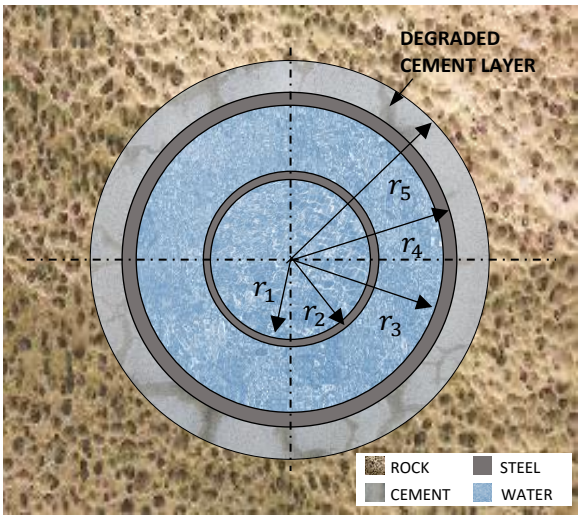

Figure 5.14 - Low-quality, degraded, cement layer (CQ).

5.3.4
Inner/Outer Debonding (SC/CR)

In order to model debonding of the cement sheath with the casing (inner debonding) or the rock formation (outer debonding), a thin fluid layer was inserted between the casing and cement or cement and rock interfaces (Figure 5.15). The acoustic properties of the concentric cylindrical fluid layer were taken as those of water. In both cases, inner and outer debonding, the distance from the outer radius of the casing to the inner radius of the rock interface was kept fixed at 0.5" (0.013 m), while the thickness of the debonding layer was varied from 20%, 40% and 60% of the original cement layer thickness (0.5"). The inner and outer debonding are labelled by interface media where it is positioned, i.e., SC stands for steel/casing interface and CR stands for cement/rock.

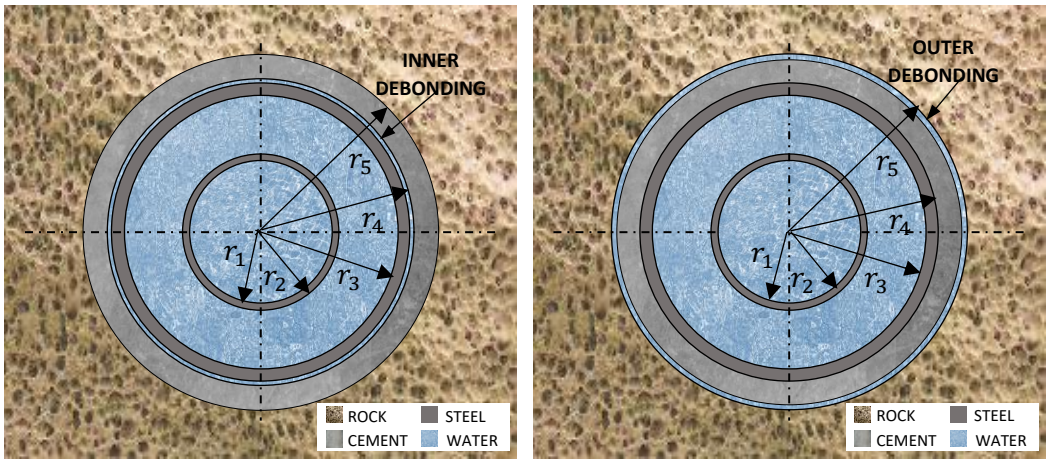

Figure 5.15 - Inner (SC) and outer (CR) debonding.

The eccentricity of layers and others defects, such like microannulus, is not analyzed in this. To investigate the microannulus, it is necessary change some restriction conditions at interfaces allowing free the shear movement between layers. However, eccentricity can not be reproduce using this analytical approach because the analytical solution is restricted to axisymmetric geometries, making

this type of analyses impossible to be done in the current development of such an analytical model.

To extend the analytical approach to analyze defects that are not axisymmetric, one should repeat the procedure presented in section 3 for each angular position, θ, being the superficial impedance matrix a function of the position angular, $G_n(\theta)$.

5.4 Results

The analytical model described in Chapter 3 was employed to study guided waves propagation in the wellbore for the configurations discussed in the preceding section, namely the non-defective one and those labelled as CH, CQ, SC and CR. Only subsonic waves, those that propagate with phase velocities below that of the S-wave in the surrounding rock formation, were investigated. These subsonic waves propagate unattenuated along the axial direction of wellbore. In a broad sense, they may be considered as generalized Stoneley waves, traveling along the wellbore with radially decaying amplitude away from the cement/rock interface, thus not penetrating deeply into the rock formation [55]. But there are also subsonic waves that propagate in the wellbore, particularly for the through-tubing configuration, carrying most of the acoustic intensity through the fluid, weakly interacting with the cement layer and therefore not well suited for the through-tubing cement logging. Other relevant class of waves are the so-called "leaky" waves, which have their amplitude attenuated in the axial direction while leaking energy into the surrounding rock formation.

It is essential to highlight that the analytical approach used here does not comprise the source excitation signal as input parameters. There is no modeling of the source, the program finds as solution the modes of the guided-waves that are able to propagate in this scenario and thus that can be generated by sources. In the current analytical approach, it is, however, possible to vary the circumferential order mode, v, presented in Chapter 3, which can be interpreted as the polarization of the excitation source.

5.4.1 Case 1: Non-Defective Cement

5.4.1.1 Single Casing (No Tubing)

Figure 5.16 presents the exact – as obtained from the theory of elasticity – dispersion spectrum for the subsonic waves propagating in the wellbore without the tubing. In Figure 5.16 (a), the representation is in terms of the axial wavenumber *vs*. frequency (k_z *vs*. f). The blue straight line in the plot corresponds to the bulk S-wave in the rock formation, whose wave speed is $c_S = 2\pi f/k_z = 2{,}650$ m/s (see Figure 5.11). Another possible representation is shown in Figure 5.16 (b) in the form of a plot of the wavelength ($\lambda = 2\pi/k_z$) of each mode *vs*. the frequency.

Phase velocity of the wave modes vary with the frequency, and are obtained by dividing the angular frequency ($\omega = 2\pi f$) by the axial wavenumber (k_z). The plot of the phase speed *vs*. frequency for each wave mode of the spectrum is presented in Figure 5.16(c). In this plot, the horizontal red line represents the S-wave speed of the rock formation, while the blue line corresponds to the sound speed of the fluid in the wellbore, water in this case.

Alternatively, the dispersion spectrum may be also represented in plots of slowness vs*. frequency*, slowness being the inverse of the phase velocity, $s = 1/c_{phase} = k_z/2\pi f$. For the case in study, the slowness diagram is presented in Figure 5.16 (d).

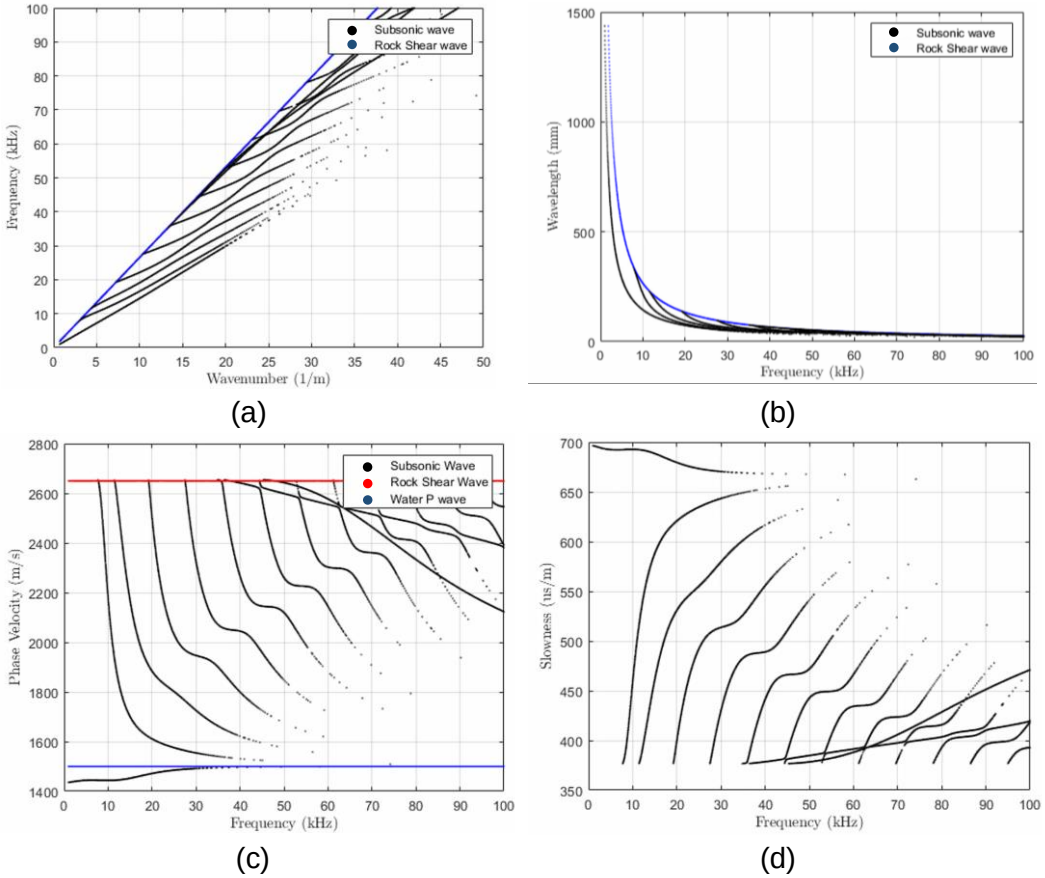

Figure 5.16 - Dispersion spectrum of subsonic waves for the single-casing well (no tubing) with non-defective cement: (a) frequency vs. wavenumber; (b) wavelength vs. frequency; (c) phase velocity vs. frequency; and (d) slowness vs. frequency. The blue line represents the P wave velocity in water while the red line represents the shear wave velocity in the outer solid media.

5.4.1.2 Through-Tubing

The dispersion spectrum for the through-tubing case with non-defective cement layer is shown in its different representations in Figure 5.17. Comparison with Figure 5.16 shows that the tubing in the wellbore substantively changes the dispersion spectrum. Waves with zero or negative group velocities are now present in the subsonic spectrum. This zone is indicated in Figure 5.17(a).

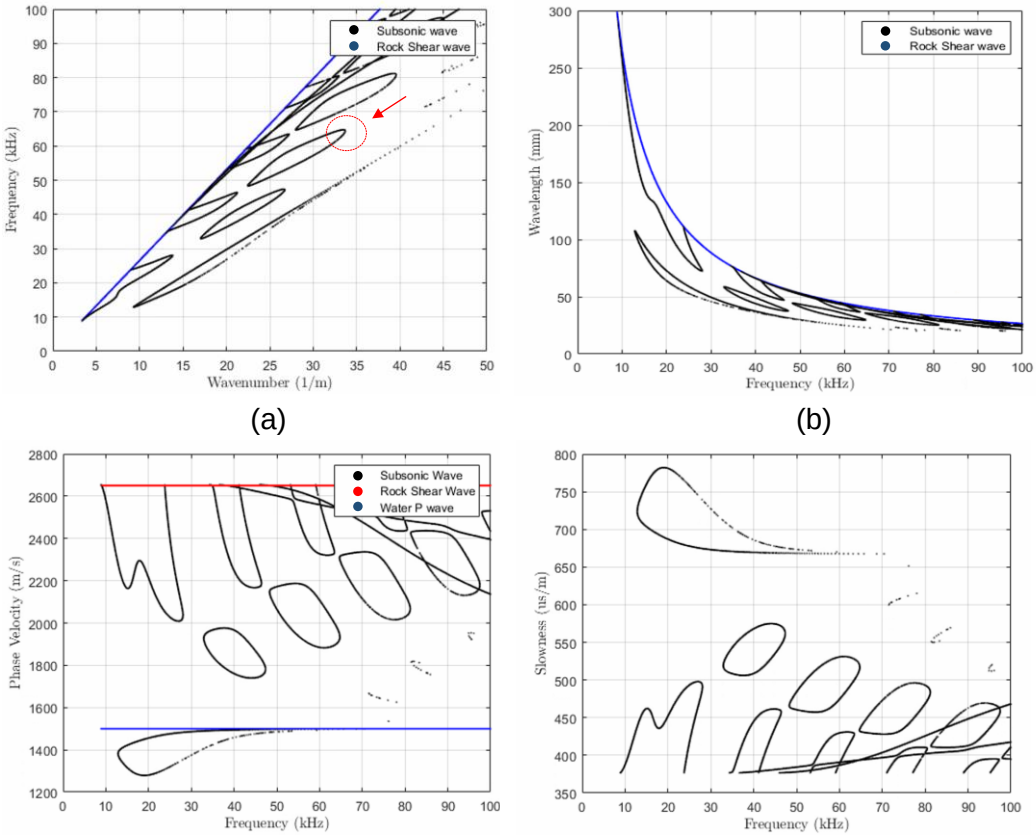

Figure 5.17 - Dispersion spectrum of subsonic waves for the through-tubing configuration with non-defective cement: (a) frequency vs. wavenumber; (b) wavelength vs. frequency; (c) phase velocity vs. frequency; and (d) slowness vs. frequency.

5.4.2 Case 2: Channeling (CH)

5.4.2.1 CH - Single Casing (No Tubing)

The exact dispersion spectra for the subsonic guided waves in the case of single-casing wellbore and with defective cement, channeling (CH) with three different thicknesses, are shown in Figure 5.18, where the plot frequency *vs*. wavenumber is presented. In this plot, only channeling defects of thickness 0.005" (0.127 mm), 0.025" (0.635 mm) and 0.050" (1.27 mm) respectively corresponding to 1%, 5% and 10% of the original cement layer thickness, are presented. The set of branches for these three different spectra may be compared to the one in Figure 5.16(a). The slowness diagrams for these same cases are presented in Figure 5.19(a), while results for thicker channeling layers, 0.1" (2.54 mm), 0.2" (5.08 mm) and 0.3" (7.62 mm) respectively corresponding to 20%, 40% and 60% of the original cement layer thickness, are found in Figure 5.19(b). These plots may be compared with the ones in Figure 5.16(d) for the well without the tubing and with a perfect cement layer. In slowness plot, we observe that the presence of the channel in the center of cement layer introduces changes in dispersion curves. Most curves

vary with the introduction of channeling but do not vary significantly with the channeling variation. The dispersion curve that vary with the presence of defect and its variation is indicated in figures with a red arrow. The reason for some of the modes being more sensitive to the defects in the cement layer is discussed in Section 5.4.6.

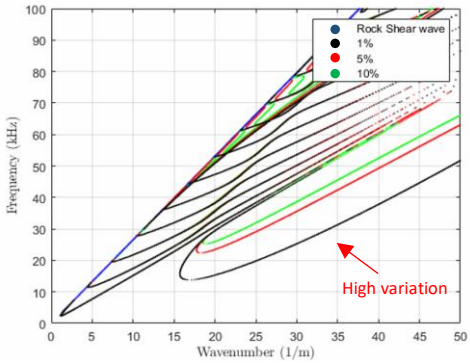

Figure 5.18 - Subsonic, frequency vs. wave number plot obtained by the analytical model for the channeling case (CH) without the tubing. The blue straight line corresponds to the S-wave in the rock formation. The red arrow indicates the curve or region where the variation is high.

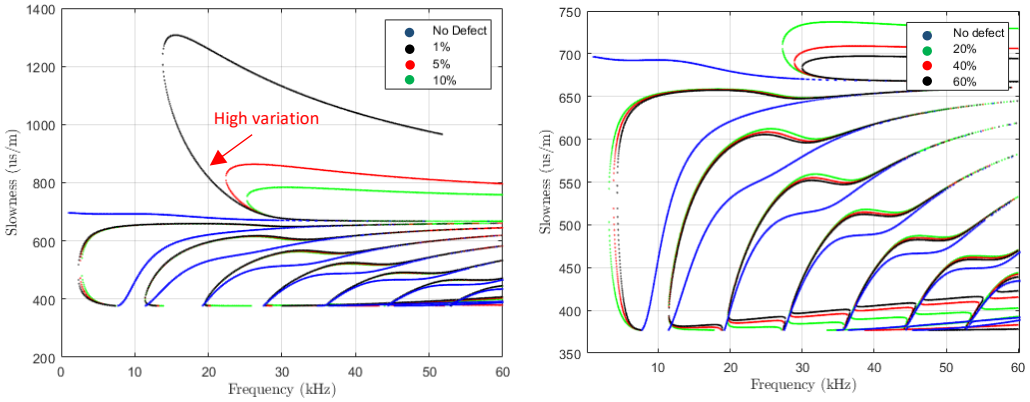

(a) *(b)*

Figure 5.19 - Slowness plots obtained by for the channeling case (CH) without the tubing. (a) Slowness vs. frequency for the channeling defect of thickness 1%, 5% and 10% of the original cement layer. (b) Slowness vs. frequency for the channeling defect of thickness 20%, 40% and 60% of the original cement layer. The red arrow indicates the curve or region where the variation is high. The blue line corresponds to the non-defective case.

5.4.2.2 CH – Through-Tubing

The dispersion spectra for the subsonic waves in the through-tubing configuration with different thickness of channeling (Figure 5.13) in the cement are shown in Figure 5.20 and Figure 5.21, the latter depicting the change of slowness with frequency. The more significant variations occur for the modes with slowness higher than that of the acoustic wave in the fluid, which is 666 µs/m for water (independent of the frequency). Again, one observes that not all modes are affected significantly by the defect variation in the cement layer, the changes occur in some curves of the dispersion spectrum and in some specific regions, as can be seen in each figure, but changes in dispersion curves due to the channeling defect occur in the majority of curves. This is discussed again in Section 5.4.6.

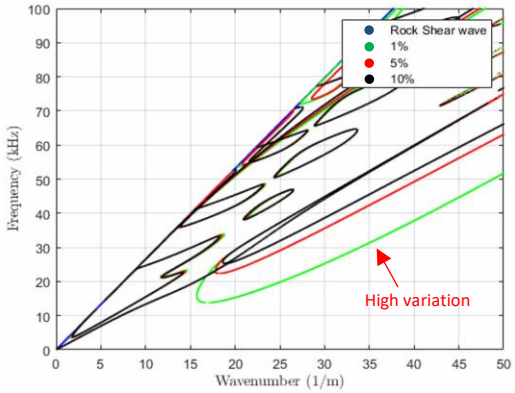

Figure 5.20 - Subsonic, frequency vs. wave number plot obtained for the channeling case (CH) in the through-tubing configuration. The blue straight line corresponds to the S-wave in the rock formation. The red arrow indicates the curve or region where the variation is significant.

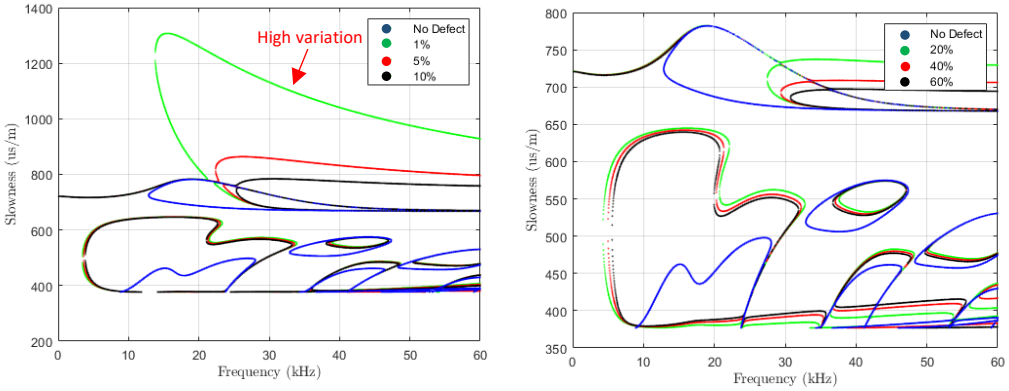

(a) (b)

Figure 5.21 - Slowness plots obtained for the channeling case (CH) with the tubing. (a) Slowness vs. frequency for the channeling defect of thickness 1%, 5% and 10% of the original cement layer. (b) Slowness vs. frequency for the channeling defect of thickness 20%, 40% and 60% of the original cement layer. The red arrow indicates the curve or region where the variation is significant. The blue line corresponds to the non-defective case.

5.4.3
Case 3: Low Quality (Degraded) Cement (CQ)

5.4.3.1
CQ – Single-Casing (No Tubing)

Dispersion spectra for the degraded cement, simulated here by decreasing its P-wave impedance, are presented for the single-casing configuration in Figure 5.22. The impedance for the non-defective cement is 5.4 MRayl. Again, not all modes are affected by the defect in the cement layer, the changes occur in some curves of the dispersion spectrum and in some specific regions, indicated in each figure. This is discussed again in Section 5.4.6.

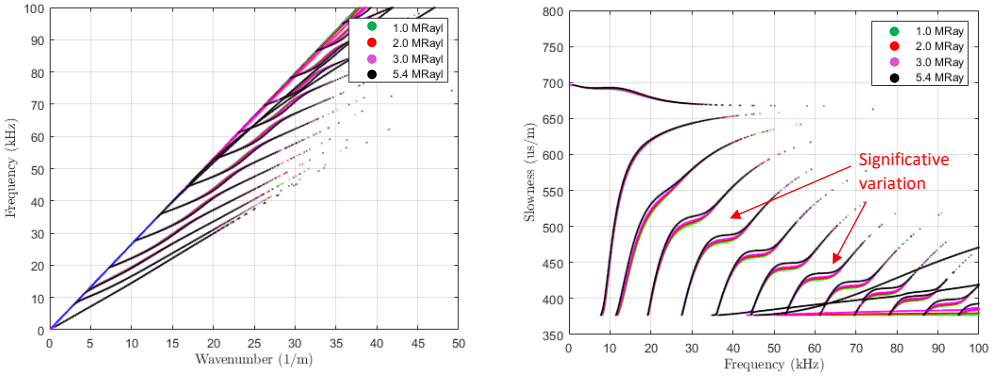

(a) (b)

Figure 5.22 - Dispersion spectra obtained by the analytical model for the degraded cement case (CQ) in the single-casing (no tubing) configuration: (a) frequency vs. wavenumber; and (b) slowness vs. frequency. The red arrow indicates the curve or region where the variation is significant. The black line corresponds to the non-defective case

5.4.3.2
CQ – Through-Tubing

Dispersion spectra for the trough-tubing configuration with degraded cement are presented in Figure 5.23 (a). The effect of the decrease of the cement's P-wave impedance is more evident in the slowness plots of Figure 5.23(b), particularly for those modes with slowness lower than that of the acoustic wave in water, which is 666 μs/m, at the frequency range from 10 to 25 kHz.

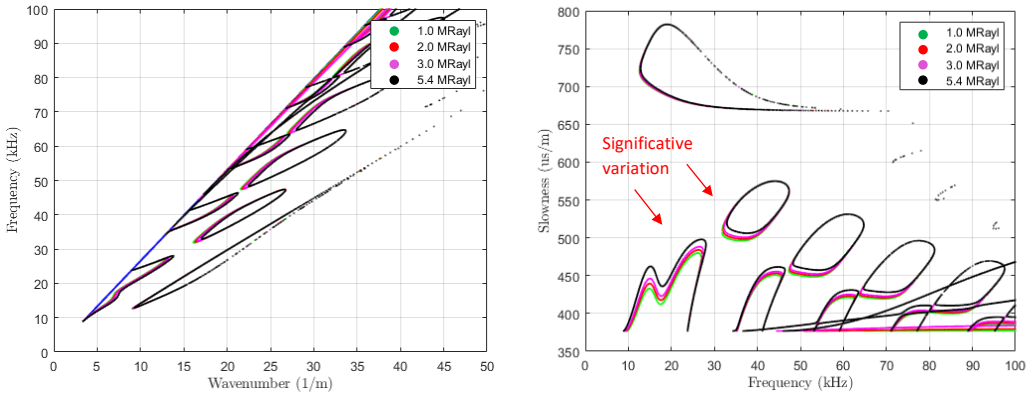

(a) (b)

Figure 5.23 - Dispersion spectra obtained by the analytical model for the degraded cement case (CQ) in the through-tubing configuration: (a) frequency vs. wavenumber; and (b) slowness vs. frequency. The red arrow indicates the curve or region where the variation is significant. The black line corresponds to the non-defective case

5.4.4
Case 4a: Inner Debonding (SC)

5.4.4.1
SC – Single-Casing (No Tubing)

Figure 5.24 presents the dispersion spectra for the single-casing well with a defect at the casing/cement interface. Results are for different thicknesses of a fluid layer between the casing and cement sheath simulating the so-called inner debonding defect. From Figure 5.24(b) the mode with slowness higher than that of the acoustic wave in the fluid (666 μs/m) and the cross mode indicated by an arrow in Figure 5.24(b) are the ones that present more significant variations due to defect variation. The other modes present variation only due to the presence of defect, not varying with changes in defect thickness.

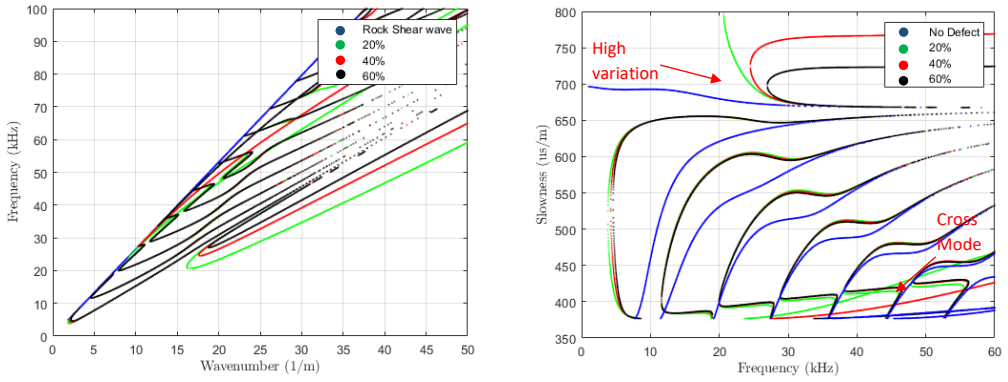

(a) (b)

Figure 5.24 - Dispersion spectra obtained by the analytical model for the inner debonding (SC) in the single-casing (no tubing) configuration: (a) frequency vs. wavenumber; and (b) slowness vs. frequency. The blue line corresponds to the non-defective case.

5.4.4.2
SC – Through-Tubing

The dispersion spectra for the well in the through-tubing configuration with a defect at the casing/cement interface are presented in Figure 5.25. Similar to the Single-Casing case, the most significant variation due to the defect variation occurs in the mode with slowness higher than 666 μs/m and in the cross mode indicated in Figure 5.25 (b). The other modes are sensitive to the defect present but not vary significatively with changes in defect thickness.

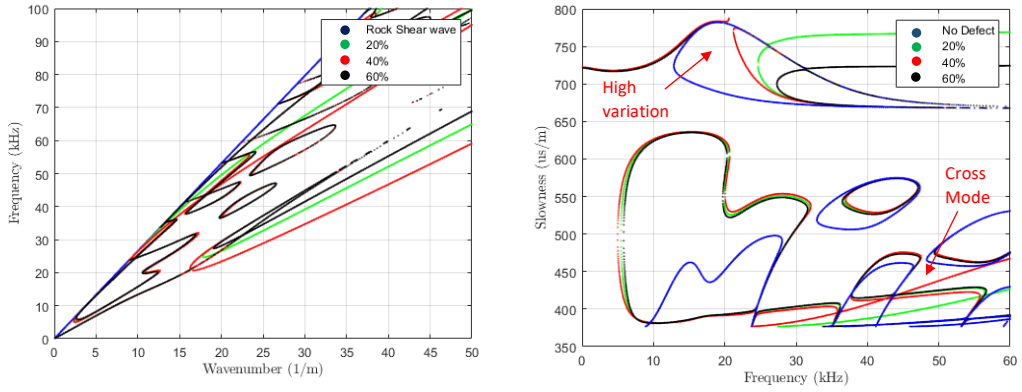

(a) (b)

Figure 5.25 - Dispersion spectra obtained by the analytical model for the inner debonding (SC) in the through-tubing configuration: (a) frequency vs. wavenumber; and (b) slowness vs. frequency. The blue line corresponds to the non-defective case

5.4.5
Case 4b: Outer Debonding (CR)

5.4.5.1
CR – Single-Casing (No Tubing)

Figure 5.26 presents the dispersion spectra for the single-casing well with a defect at the cement/rock interface. Results are for different thicknesses of a fluid layer between the cement sheath and the rock formation, simulating an outer debonding defect. From Figure 5.26(b), it can be seen that the most significant variations occurs next to inflection points of curves for the defect presence and its thickness variation. An important observation is that with the present of defect the mode with slowness higher than 666 us/m disappear.

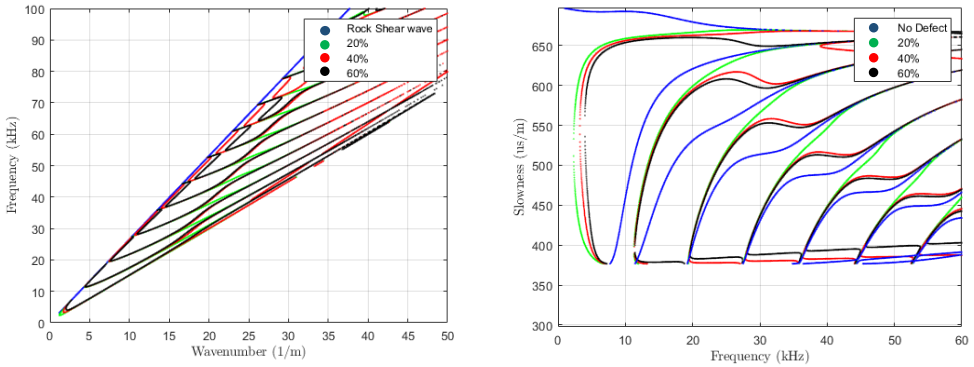

(a) (b)

Figure 5.26 - Dispersion spectra obtained by the analytical model for the outer debonding (CR) in the single-casing (no tubing) configuration: (a) frequency vs. wavenumber; and (b) slowness vs. frequency.

5.4.5.2
CR – Through-Tubing

The dispersion spectra for the well in the through-tubing configuration with a defect at the cement/rock interface are presented in Figure 5.27. In this case, it can be seen in Figure 5.27(b) that for a defect thickness of 40% and 60% the closed loops appear, unlike for 20% thickness.

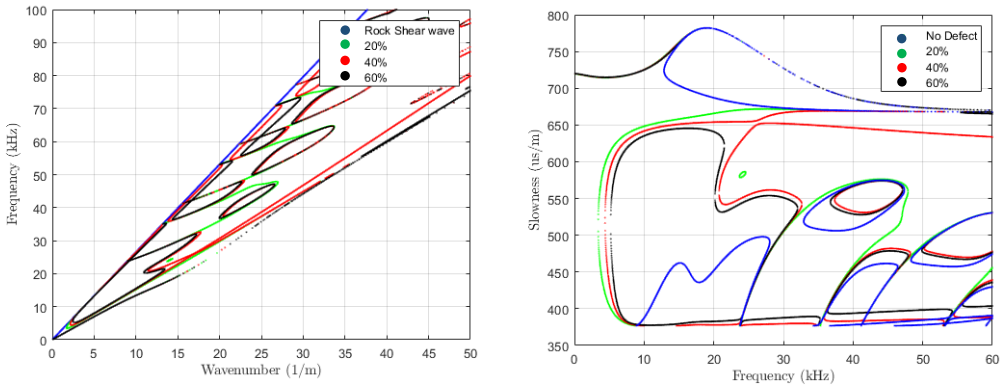

(a) (b)

Figure 5.27 - Dispersion spectra obtained by the analytical model for the outer debonding (CR) in the through-tubing configuration: (a) frequency vs. wavenumber; and (b) slowness vs. frequency. The blue line corresponds to the non-defective case

5.4.6
Axial Power Flow Density Distribution

5.4.6.1
Power Flow – Single-Casing (No Tubing)

As explained in Chapter 3, once the elastic and acoustic fields are calculated for a given mode, at a particular pair of (angular) frequency and wavenumber that satisfies the dispersion equation, the period-averaged power flow radial distribution in the axial direction, or the intensity of the mode, may be evaluated through Equations 3.191 or 3.192. In this section, we present results for different subsonic wave modes in the case of the well, both in single-casing and through-tubing configurations, with non-defective cement. We observe that some of the modes carry most of the energy at the casing, and therefore they should be more sensitive to defects in the cement sheath. Those modes which have high power densities inside the tubing and in the casing should be more suitable for inspecting the cement sheath.

The slowness curves of Figure 5.16(d) are reproduced below in Figure 5.28, which, through the colored dots, indicate the modes for which the axial power flow distribution is analyzed in the sequence.

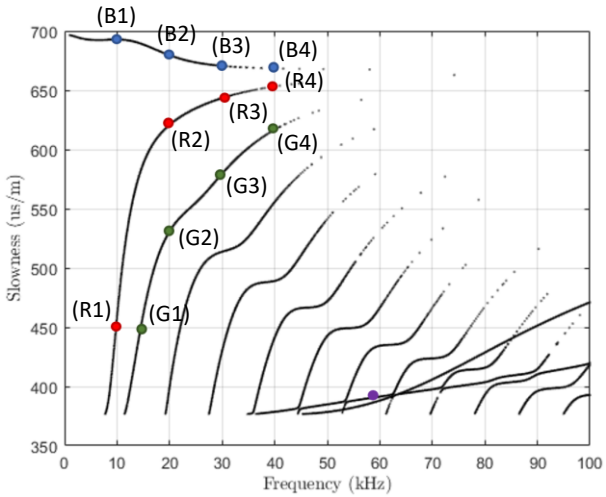

Figure 5.28 - Slowness curves for the single-casing configuration and non-defective cement. The blue, red, and green dots are the guided wave modes for which the radial power flow is presented in the sequence.

The axial power flow density distribution along the radial direction for some of the frequencies of the mode with higher slowness (blue dots), the mode with red dots and the mode with green dots for the single-casing configuration of the well with non-defective cement, are plotted in Figure 5.29, Figure 5.30 and Figure 5.31, respectively.

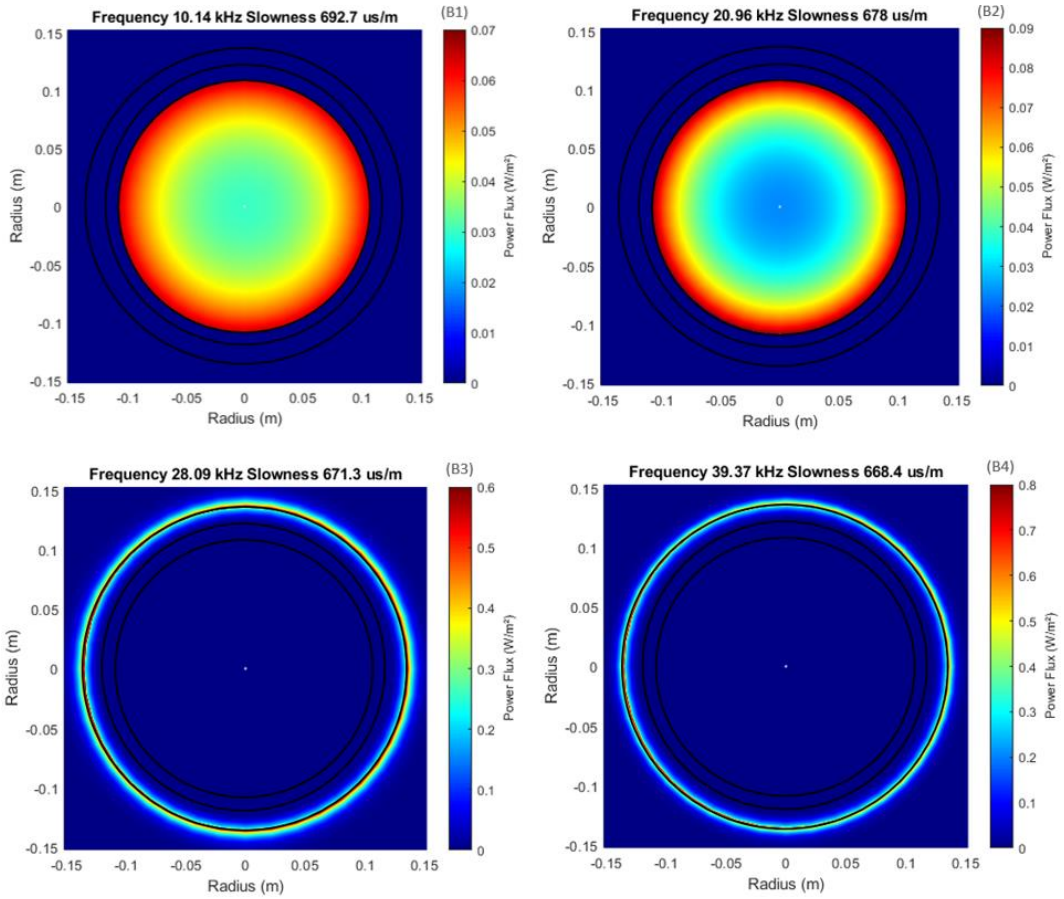

Figure 5.29 - Axial power flow density for the modes indicated by the blue dots in the slowness diagram for the single-casing well with non-defective cement (see Figure 5.28).

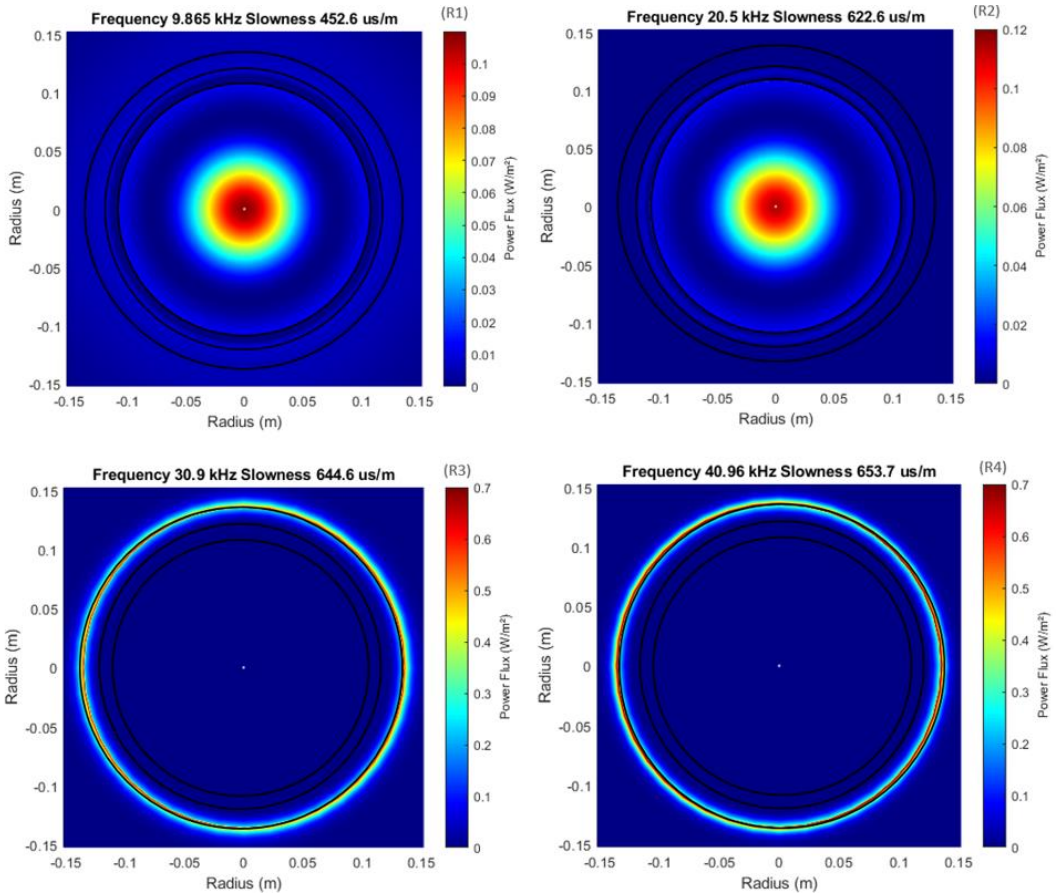

Figure 5.30 - Axial power flow density for the modes indicated by the red dots in the slowness diagram for the single-casing well with non-defective cement (see Figure 5.28).

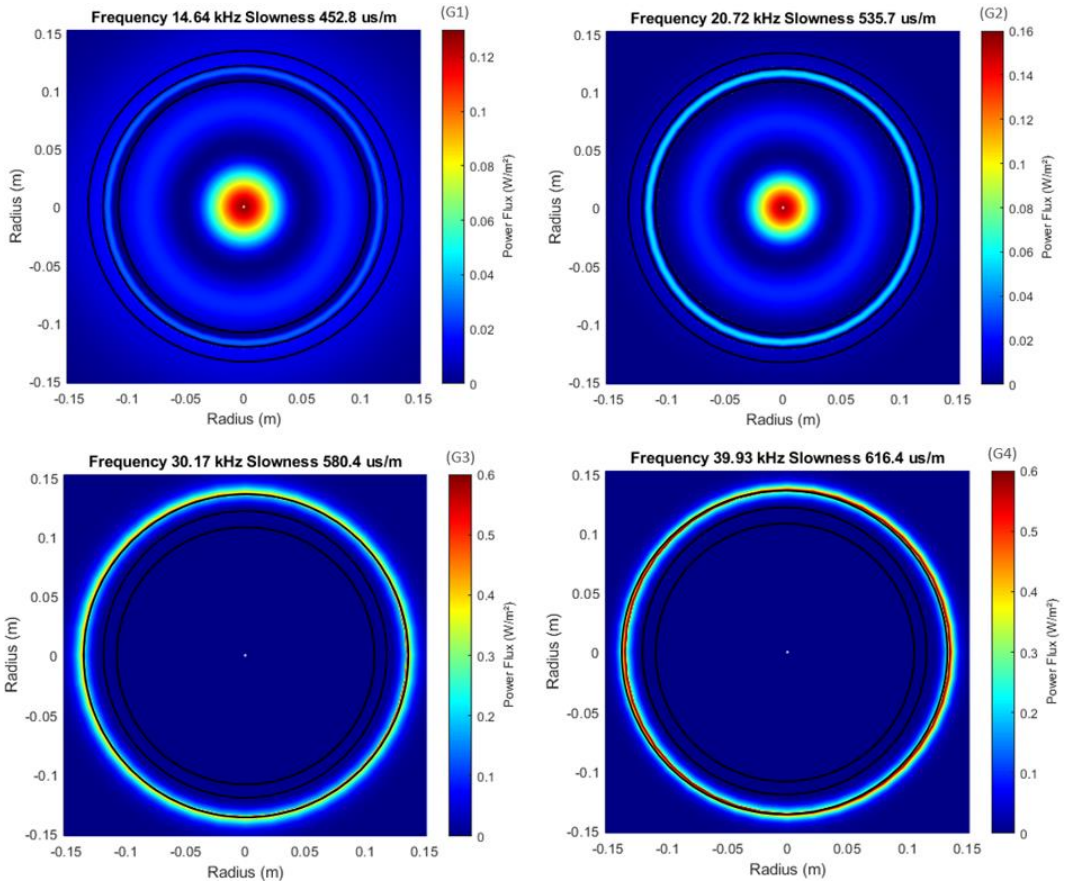

Figure 5.31 - Axial power flow density for the modes indicated by the green dots in the slowness diagram for the single-casing well with non-defective cement (see Figure 5.28).

At the lower frequency range, around 10 and 20 kHz, most of the energy carried by the wave is in the fluid filling the wellbore. As the frequency increases, close to 28 and 40 kHz, the flow moves into the cement layer and the rock formation which are now carrying most of the energy transported by these wave modes. The same pattern is noticed in Figure 5.30 and Figure 5.31, where, at higher frequencies, the energy of the guided wave modes tends to concentrate in the casing and cement.

For each dot, the power flow distribution through the well was analyzed and indicated in which layer the energy is more concentrated. The results of this analysis are presented in Table 5.5 and one can conclude that in points B3, B4, R3, R4, G3 and G4 the energy is concentrated in the cement/formation interface.

When the energy is concentrated in the cement layer, the influence of defects in the dispersion curves is expected to become greater and can be identified more easily. As can be seen in Figure 5.29, Figure 5.30 and Figure 5.31, the concentration of energy in cement layer occur for high frequencies, so aiming to optimize the defects identification, the high frequency values have to be considered. The modes where the energy concentrates in cement layer were highlighted in Table 5.5.

Table 5.5 – The axial Power flow distribution for each dot.

Modes	Frequency (kHz)	Slowness (us/m)	Predominance of Power Distribution	Cement/Rock Interface Energy $(W/m2)$
B1	10.14	692.7	Borehole	1.349×10^{-4}
B2	20.96	678	Borehole	1.525×10^{-5}
B3	28.09	671.3	Cement/Rock Interface	2.400×10^{-1}
B4	39.37	668.4	Cement/ Rock Interface	3.196×10^{-1}
R1	9.86	452.6	Well Center	5.036×10^{-3}
R2	20.50	622.6	Well Center	3.428×10^{-4}
R3	30.90	644.6	Cement/ Rock Interface	2.464×10^{-1}
R4	40.96	653.7	Cement/ Rock Interface	3.199×10^{-1}
G1	14.64	452.8	Well Center	1.116×10^{-2}
G2	20.72	535.7	Well Center and Casing	5.592×10^{-3}
G3	30.17	580.4	Cement/ Rock Interface	2.055×10^{-1}
G4	39.93	616.4	Cement/ Rock Interface	2.863×10^{-1}

Observing Figures 5.19, 5.22, 5.24 and 5.26 presented in Chapter 5 to the Single-casing configuration, the variation of the dispersion curves at each locus represented by the colored dots are analyzed. This is performed in order to determine a promise mode for logging, which would be a mode that carries significant energy at the cement layer whilst present variations in the dispersion curves. Table 5.6 present the intensity of defect variation, i.e., high, small or negligible. If the locus represented by a colored dot disappear with the defect variation, the intensity cannot be determined. The yellow highlight indicates the modes that energy is concentrated next to cement/rock interface.

Table 5.6 – The variation of the predefined modes with presence of each defect. The green color means high variations, while grey and white means small and negligible, respectively. The dash indicates inconclusive. Yellow highlights indicate the modes that have the energy concentrated next to cement layer.

Modes	CH Variation (us/m)			CQ Variation (MRayl)			SC Variation (us/m)			CR Variation (us/m)		
	1%	5%	10%	1.0	2.0	3.0	20%	40%	60%	20%	40%	60%
B1	-	-	-	0	0	0	-	-	-	-	-	-
B2	586	-	-	0	0	0	-	-	-	-	-	-
B3	472	188	112	0	0	0	-	-	-	-	91	47
B4	374	164	106	0	0	0	-	-	-	-	97	54
R1	200	200	200	0	0	0	206	203	201	196	196	196
R2	36	36	36	0	0	0	44	40	37	33	33	33
R3	0	5	5	0	0	0	26	25	5	3	3	3
R4	0	0	0	0	0	0	15	15	0	0	0	0
G1	83	83	83	13	13	13	81	81	81	78	78	78
G2	66	66	66	69	69	69	64	60	57	55	55	55
G3	30	30	30	0	0	0	63	27	17	17	17	17
G4	0	0	0	0	0	0	37	0	0	0	0	0

The frequency from which the energy becomes concentrated in cement layer is not necessary the same for all modes. In Figure 5.29, 5.30 and 5.31, one can see that for frequency values greater than the ones of B3, R3 an G3 the energy is concentrated in cement layer.

Even the energy remaining concentrated in cement layers, the variation is not be the same for other types of defect. For channeling defect (CH) the variation of dispersion curves is negligible in G4 but occurs in B4 however for outer debonding (SC), for example, the variation occurs in G3, but it is negligible in G4.

The reason why there are modes that do not vary significantly with the extension of the defect can possibly find an explanation if one argues that those waves are more influenced by the interface condition between defect and the well

layer. That is, the presence of a deboning defect of any thickness implies already in the lack of full contact between layers, heavily changing the propagation condition, and the effect of increasing the thickness of the defects is minor.

One can conclude that the most promising modes and frequencies to detect each defect are the ones that combine good energy concentration in the cement layer as well as dispersion curves variation. From Table 5.6 these are B3 and B4 for CH; G3 for SC and CR; for CQ. Nevertheless, there is no analyzed mode that shows a high variation and energy concentration for defect CQ, even though G1 and G2 show a slightly better performance.

5.4.6.2
Power Flow – Through-Tubing

Figure 5.32 reproduces the slowness curves previously presented in Figure 5.17(d) for the through-tubing well configuration and non-defective cement. The colored dots indicate the subsonic guided wave modes for which the radial distributions of the axial power flow densities will be presented.

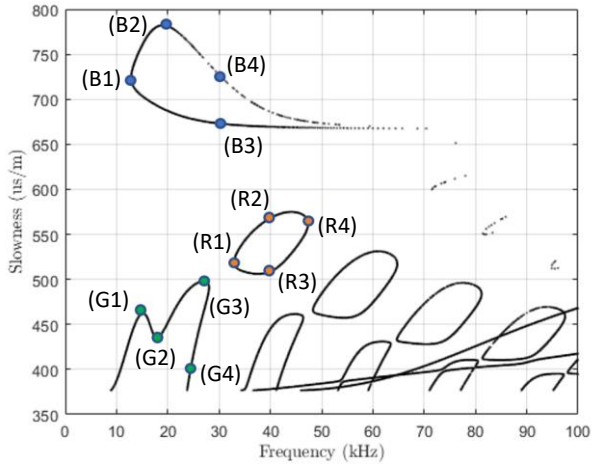

Figure 5.32 - Slowness curves for the through-tubing configuration and non-defective cement. The blue, red, and green dots are the guided wave modes for which the radial power flow is presented in the sequence.

Results presented in Figure 5.33, Figure 5.34 and Figure 5.35 show the axial, averaged power flow densities for the modes indicated by the blue, red and green dots in Figure 5.32. As for the single-casing configuration, one observes that not all modes carry energy in the casing and cement layer. For instance, the subsonic mode at the lower right-hand side of Figure 5.34, with frequency of 39.2 kHz and slowness of 507 μs/m, which carries energy both in the tubing and in the cement layer, seems to be a good candidate to be used to inspect the cement layer in the through-tubing configuration. However, if the interest is only to identify the defects present in the cement layer, the mode at the upper right-hand side of Figure 5.25, with frequency of 30.13 kHz and slowness of 726.5 μs/m, seems a better candidate because the energy is fully concentrated in cement layer.

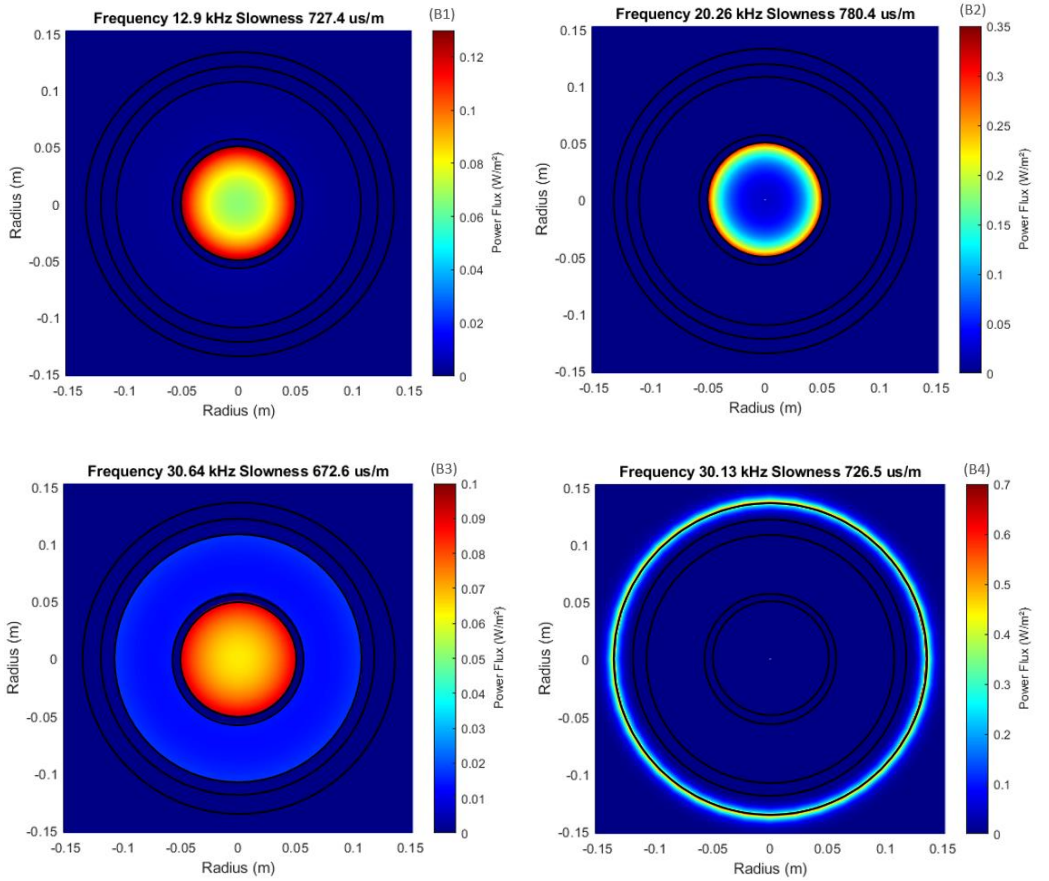

Figure 5.33 - Axial power flow density for the modes indicated by the blue dots in the slowness diagram for the through-tubing well configuration with non-defective cement (see Figure 5.32).

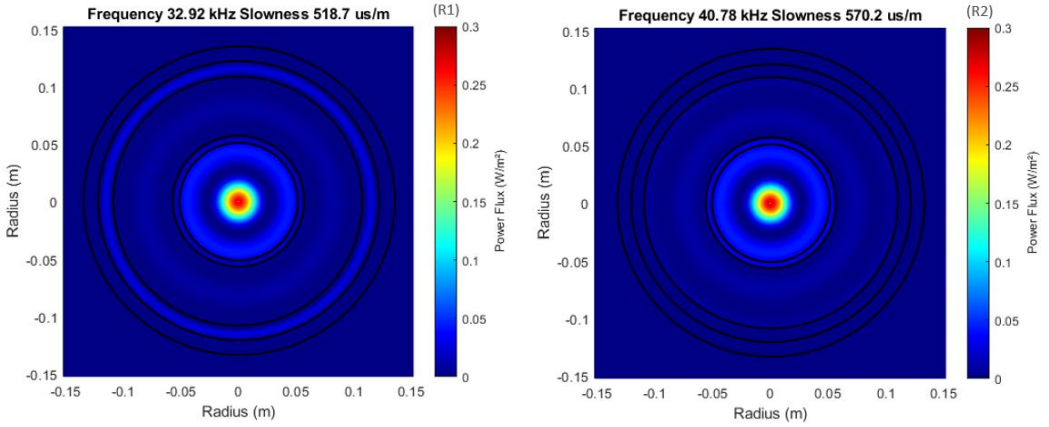

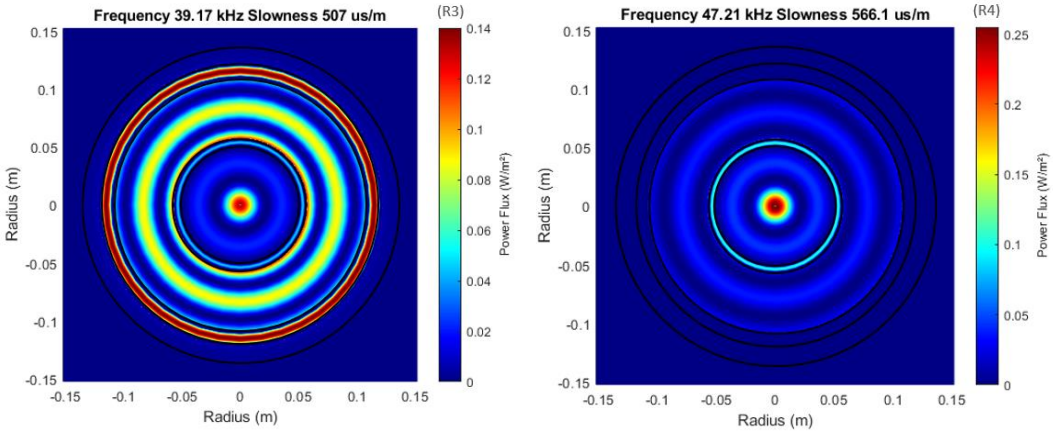

Figure 5.34 - Axial power flow density for the modes indicated by the red dots in the slowness diagram for the through-tubing well configuration with non-defective cement (see Figure 5.32).

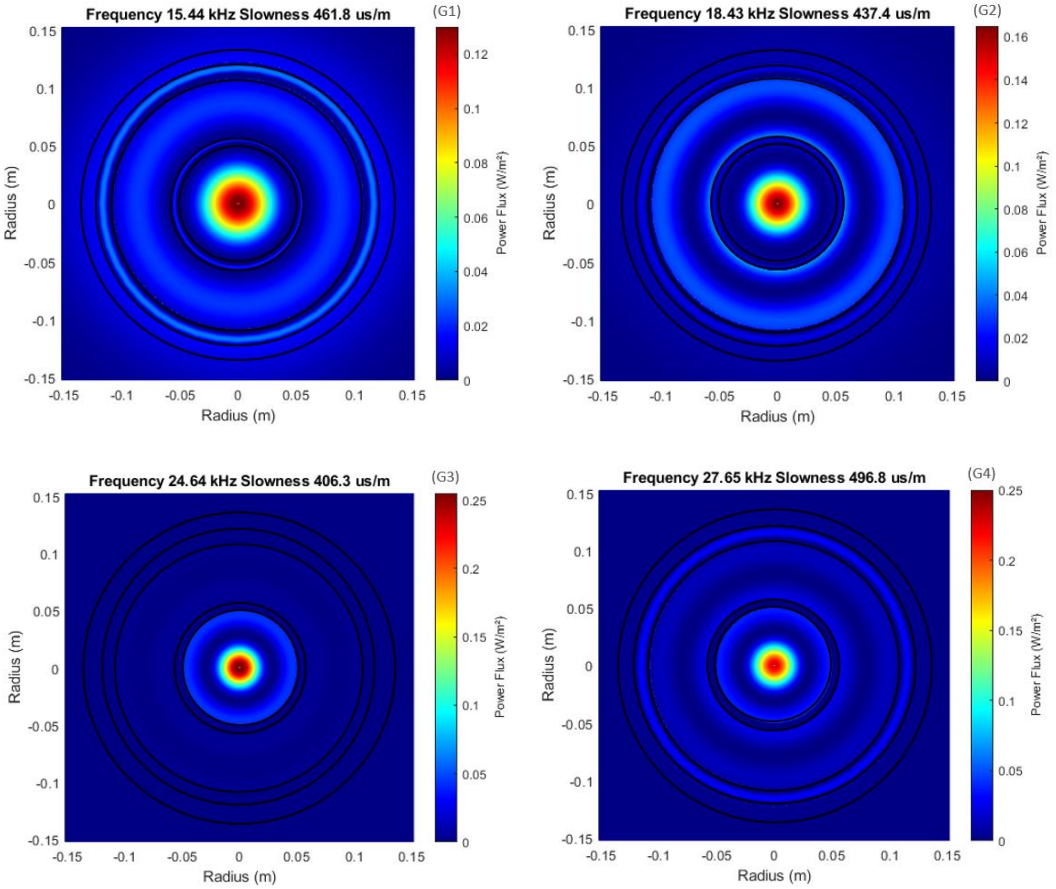

Figure 5.35 - Axial power flow density for the modes indicated by the green dots in the slowness diagram for the through-tubing well configuration with non-defective cement (see Figure 5.32).

As for the single-casing, Table 5.7 identify in which modes the energy remains concentrated in cement layer. One can observe that in B4 the energy is concentrated in Cement/Rock interface.

Table 5.7 – Energy distribution for each point.

Modes	Frequency (kHz)	Slowness (us/m)	Predominance of Energy Distribution	Cement/Rock interface energy $(W/m2)$
B1	12.9	727.4	Inside Tubing	4.038×10^{-5}
B2	20.26	780.4	Inside Tubing	4.341×10^{-8}
B3	30.64	672.6	Borehole	7.275×10^{-6}
B4	30.13	726.5	Cement/Formation Interface	2.838×10^{-1}
R1	32.92	518.7	Center of Well	7.525×10^{-4}
R2	40.78	570.2	Center of Well	1.543×10^{-5}
R3	39.17	507	Casing/A-annulus	2.508×10^{-3}
R4	47.21	566.1	Center of Well	8.951×10^{-6}
G1	15.44	461.8	Center of Well	1.071×10^{-2}
G2	18.43	437.4	Center of Well	4.812×10^{-3}
G3	24.64	496.8	Center of Well	1.296×10^{-4}
G4	27.65	406.3	Center of Well	1.924×10^{-3}

Table 5.8 present how each mode varies with the defects. Similarly, to the single-casing configuration, even when the energy remains concentrated in cement layers, the variation due to presence of defects depends on the nature of defect. For cement quality defect (CQ), for example, the variation of dispersion curves is negligible in B4 and R3 but it is intense in channeling (CH).

Table 5.8 – The variation of the predefined modes with presence of each defect. The green color means high variations, while grey and white means small and negligible, respectively. The dash indicates inconclusive. Yellow highlights indicate the modes that have the energy concentrated next to cement layer.

Modes	CH Variation (us/m)			CQ Variation (MRayl)			SC Variation (us/m)			CR Variation (us/m)		
	1%	5%	10%	1.0	2.0	3.0	20%	40%	60%	20%	40%	60%
B1	-	-	-	0	0	0	-	17	17	0	0	0
B2	449	-	-	0	0	0	-	0	0	0	0	0
B3	9	9	9	0	0	0	7	7	7	0	0	0
B4	403	291	218	0	0	0	36	-	6	0	0	0
R1	-	-	-	19	16	13	-	-	-	-	-	-
R2	0	0	0	0	0	0	0	0	0	0	0	0
R3	34	34	34	2	2	2	19	19	19	49	26	22
R4	0	0	0	0	0	0	0	0	0	42	0	0
G1	184	184	184	29	22	16	174	174	174	196	189	183
G2	208	208	208	25	20	17	192	192	192	225	215	207
G3	69	69	69	18	13	9	51	53	55	-	62	55
G4	160	160	160	0	0	0	0	0	0	0	0	0

In through-tubing case, the interpretation of results is not as simple as in single-casing case. The energy is not concentrated in the cement layer for high frequencies values but in specific zones that have to be previously investigated. Mode B4 seems to be a promising excitation mode because much energy is concentrated next to cement layer.

From Table 5.8, for channeling defect a high variation can be observed in B4, G1, G2 and G4; for inner and outer disbonded only G1 and G2 presented high variation, however, for cement quality defect, no mode presented high variation. In B4, even the energy being fully concentrated in cement layer, only the channeling present great variation in dispersion curves. In the other hand, G1 and G2 present high variation in CH, SC and CR and a meaningful variation for CQ but energy is not greatly concentrated in cement layer.

Interestingly, for both through-tubing and single-casing configuration the modes in which the energy is more concentrated in the cement layer were not the

ones that had the greatest variations with the presence of defect as expected. It is necessary further investigation about this non-intuitive finding in order to fully elucidate its reasons.

6
Conclusion

In Chapter 2, reviewed the main defects in wells and the different acoustic techniques used to evaluate the cement condition. Motivated by the promising results using guided waves presented in the literature, the main defects were investigated with the analytical code. From the equations derived in chapter 3 and the analytical code developed in chapter 4 to solve the dispersion equations, it was possible to model the case of an oil well with the tubing and to reproduce the main and most frequent defects of the oil layer found in the literature.

The defects analyzed here were Channeling (CH), Cement Quality (CQ) and inner/outer debonding (SC/CR). These types of defects were chosen because they can be represented with a 2D axisymmetric model, being thus good candidates for an initial investigation. The first consists of one or more thin layers of fluid located inside the cement, resulting from the continuous corrosion of the cement. Cement Quality (CQ), consists of the low impedance of the cement, reaching the impedance values for fluids or even air. This happens because some types of cement used in cementation can be naturally porous (Form Cement) due to the natural wear, being lighter the decreasing its impedance. The inner/outer debonding (SC/CR) consists of significantly reducing the thickness of the cement due to corrosions that can occur at the interface in contact with the casing (SC) or at the interface in contact with the formation.

The dispersion equations for the single-casing and through-tubing case were solved without the presence of any defects and with the presence of each of the aforementioned defects. The CH defect was modeled as a simple layer of axisymmetric water positioned in the middle radius of the cement, varying only its thickness. The SC and CR defects were modeled as a thick layer of water positioned at the cement interfaces, varying only in thickness. To reproduce the QC, only the acoustic impedance of the cement was varied.

In order to validate the developed algorithm, the code was used to obtain the dispersion curves of several cases in the literature, comparing both results. For all tested cases, the algorithm was successful in finding the same dispersion curves as those presented in the literature.

It was also seen that using the curves for slowness versus frequency instead of frequency versus wave number as dispersion curves, a better perception of possible variations in modes with the introduction of defects was achieved.

For the CH defect, it was found that one of the obtained curves, the ones that encompass the dot labels B1, B2, B3 and B4, was very sensitive to variations in the thickness of this defect. For some of other modes obtained, both for single-casing and through-tubing, the variations happened but not in the same intensity.

Some modes varied with the presence of defect but not with its variation as R1, R2, G1, G2, G3 for single-casing and R3, G1, G2, G3, G4 for through-tubing.

For the QC defect, the variations of the curves were more evident in specific regions for both the single-casing case, where the variations are more evident near the inflection points (G1, G2) while for the through-tubing case, it occurs more evident in certain regions of the obtained circular modes (R1, G2, G2, G3).

For the SC defect, the mode that was most sensitive to the variation of the defect was the one that has slowness greater than 666 μs/m; it also varied widely. This widely variation hindered the measurement of slowness variation becoming inconclusive. This is true for both the single-casing case and the through-tubing case.

Energy distribution in the well was obtained for a non-defective well. It was verified that for the case of single-casing that for low frequency values the energy is distributed throughout the interior of the casing, causing little energy to propagate through the cement, which, in turn, causes the defects presented in the cement to have very little influence on the variations of the dispersion curves, making them difficult to be identified. For high frequencies modes (B3, B4, R3, R4, G3, G4) the energy is basically concentrated in the cement layer, the curves being totally influenced by changes in this medium.

For the case of through-tubing, the concentration of energy in the cement layer occurs in specific regions in some ways. It was seen that for the frequency of 30.13 kHz and the slow speed of 726.5 μs / m, represented by B4, the energy is totally concentrated in the cement layer, which indicates a good candidate as a source excitation mode. However even B4 concentrating energy in cement layer the variation of dispersion curves is not the same for all defects.

It also seen for the though-tubing configuration that in CQ and CR the variance of dispersion curves is negligible in B4 but it is great in CH. Even the energy in cement layer not being so high, G1 and G2 are possible alternative solutions because there is a high variation in dispersion curves to CH, SC, CR and a significant variation for CQ.

Similarly, in a single-casing configuration, for example, the spectrum variation in cement quality defect (CQ) is negligible in B4 but occurs significant for G2 to all analyzed defects.

6.1
Future works

As a continuation of this work it is suggested the following:

- Analyze the influence that other defects present in the literature, such as the microannulus, promotes in the dispersion curves. To reproduce the microannulus, the boundary conditions at the respective interface must be modified in order to allow only the radial coupling, decoupling the shear effect.

- Introduce small variation in the thickness of layers since it is very usual in real situation, in order to observe how it can affect the dispersion curves. As this procedure would not be axisymmetric, as well as the eccentricity defect, it would be necessary to alter the analytical approach.

- Investigate supersonic modes, such as Leak mode, to find out if they are also sensitive to the presence of defects. For this, it is necessary to carry out an analysis of the roots obtained for supersonic values, verifying if they have a physical sense of existing.

- Obtain the time-domain signal from the dispersion curves, so that it is possible to validate this model against other kinds of simulations. This will be very useful for future comparisons.

- Create new variables in modeling the defects present in this report, such as introducing two or more layers of channeling. This would make it possible to investigate and analyze more realistic conditions of the problem.

- Investigate other circumferential excitation modes of the source (dipole, quadrupole, hexapole), in order to optimize the propagation of the guided wave, minimizing energy losses and optimizing the identification of defect since in this work only the monopole source was considered in the analysis.

- Verify with numerical models, such as finite elements, if the modes and frequencies deemed here as the most promising, really produce clearly identifiable signals in the presence of defects.

- Verify with acoustic experiments if the dispersion spectrum found using the analytical solution agrees with one obtained experimentally. For this analysis it is necessary to build an experimental setup capable to reproduce the acoustic guided waves propagation in this scenario.

7. Bibliography

[1] LIU, H. Principles and Applications of Well Logging. Springer Berlin Heidelberg, p. 237-269, 2017.

[2] SAXENA, V.; KRIEF, M.; ADAM, L. Handbook of Borehole Acoustics and Rock Physics for Reservoir Characterization. Elsevier, 2018.

[3] ØSTERBO, K. Cement Bond Evaluation. 2014.

[4] ØIA, T. M.; MATTS, M. A.; TORBJØRN, V. Innovative Approaches for Full Subsea P&A Create New Opportunities and Cost Benefits. In: **SPE Norway One Day Seminar**. Society of Petroleum Engineers, 2018.

[5] **Resolução ANP No. 46 de 2016**. Avaliable at: http://legislação.anp.gov.br/?path=legislacao-anp/resolanp/2016/novembro&item=ranp-46--2016. Access in 21 March 2019

[6] **Completação - Série Concursos Públicos Curso Prático & Objetivo**. Avaliable at: https://docplayer.com.br/3680200-Completacao-serie-concursos-publicos-curso-pratico-objetivo-completacao.html. Access in 06 March 2020.

[7] WANG, H.; TAO, G.; SHANG, X. Understanding acoustic methods for cement bond logging. **The Journal of the Acoustical Society of America**; v.139, n. 5,p. 2407-2416, 2016.

[8] HAVIRA, R. M. Ultrasonic cement bond evaluation. In: **SPWLA 23rd Annual Logging Symposium**. Society of Petrophysicists and Well-Log Analysts, 1982.

[9] JUTTEN, J. J.; PARCEVAUX, P. Relationship Between Cement Bond Log Output and Borehole Geometrical Parameters. In: **SPE/IADC Drilling Conference**. Society of Petroleum Engineers, 1987.

[10] ZHANG, J.; MAHBOD, P.; SHAFER, R.; MULLER, D.; ANDERSON, C. Multi-String Isolation Logging - A Cost Effective Solution for P&A. In: **SPE Norway One Day Seminar.** Society of Petroleum Enginners, 2019.

[11] HE, X.; CHEN, H.; WANG, X. Ultrasonic leaky flexural waves in multilayered media: Cement bond detection for cased wellbores. Cement bond detection for cased wellbores. **Geophysics**, v. 79, n. 2, p. A7-A11, 2014

[12] VIGGEN, E. M.; JOHANSEN, T. F.; MERCIU, I. Simulation and modeling of ultrasonic pitch-catch through tubing logging. **Geophysics**, v. 81, n. 4, p. D383-D393, 2016.

[13] QUINTERO, Luis F.; ZHENG, Yibing; KIRKWOOD, Andrew. **CHARACTERIZATION OF WELLBORE MATERIALS IN**

MULTIPLE CASING STRINGS. International Patent Application n. 62/218,542, 23 mar. 2017.

[14] FAN, Bo; SKATARIC, Maja; BOSE, Sandip; AERON, Shuchin; ZEROUG, Smaine. **Method of analizing cement integrity in annuli of a multiple-cased well using machine learning.** International Patent Application n. 62/577,945, 02 may 2019

[15] ESPE, Eirik; NYHAVN, Fridtjof; JOHANSEN, Tonni Franke. **Tool, system and a method for determining barrier and material quality behind multiple tubulars in a hydrocarbon wellbore**. U.S. Patent Application n. 16/258,070, 25 jul. 2019.

[16] LIU, Y. et al. Teoretical and Experimental investigations of acoustic waves in embedded fluid-solid multi-string structures. **Applied Physics Letters**, v. 110, n. 10, p. 101906, 2017.

[17] LIU, Y. et al. Experimental investigation of acoustic features associated with cement damages in double cased-wellbores. In: **AIP Conference Proceedings.** AIP Publishing LLC, 2019. p. 050024.

[18] VIGGEN, E. M.; JOHANSEN, T. F.; MERCIU, I. Analysis of outer-casing echoes in simulations of ultrasonic pulse-echo through-tubing logging. **Geophysics**, v. 81, n. 6, p. D679-D685, 2016.

[19] TALBERG, A. S.; JOHANSEN, T. F.; LARSEN, I. Laboratory Experiments on UltrasonicLogging Through Casing for Barrier Integrity Validation. In: **ASME 2017 36th International Conference on Ocean, Offshore and Arctic Engineering**. American Society of Mechanical Engineers Digital Collection, 2017.

[20] BRAGA, A. M. B. et al. High-frequency response of isotropic-laminated cylindrical shells modeled by a layer-wise theory. **International journal of solids and structures**, v. 42, n. 14, p. 4278-4294, 2005.

[21] BRAGA, A. M. B.; BARBONE, P. E.; HERRMANN, G. Wave propagation in fluid-loaded laminated cylindrical shells. **Applied Mechanics Reviews,** v. 45, n. 5, p. S359-S365, 1990.

[22] STANDARD, NORSOK. Well Integrity in Drilling and Well Operations. **D-010, rev**, v. 3, 2004.

[23] **CAMERON, I. SPE Back to Basics - Bond Log Theory and Interpretation,** 2013. Avaliable at: https://higherlogicdownload.s3.amazonasws.com/SPE/5fc0079d-67s5-4dd9-a56f-190534ef5d3d/UploadedImages/April16_BtoB.pdf. Access in: 21 March 2019.

[24] KHALIFEH, M. et al. Technology Trends in Cement Job Evaluation Using Logging Tools. In: **Abu Dhabi International Petroleum Exhibition & Conference**. Society of Petroleum Engineers, 2017.

[25] IZUHARA, W. et al. Full-Range Quantitative Cement Bond Evaluation with LWD Sonic: The Right Way of Approach Using a Hybrid of Amplitude and Attenuation. In: **SPE Annual Technical Conference and Exhibition**. Society of Petroleum Engineers, 2017.

[26] QI, Z. B. et al. A Novel and Efficient Method for Quantitative Cement Logging using a Logging-While-Drilling Acoustic Tool. In: **SPE Kuwait Oil & Gas Show and Conference**. Society of Petroleum Engineers, 2017.

[27] THIERRY, S. et al. Ultrasonic Cement Logging: Expanding the Operating Envelope and Efficiency. In: **SPWLA 58th Annual Logging Symposium**. Society of Petrophysicists and Well-Log Analysts, 2017.

[28] HE, X.; CHEN, H.; WANG, X. Numerical simulations of ultrasonic flexural waves in cased wellbores and evaluations of the cement bond quality. In: **2015 IEEE International Ultrasonics Symposium (IUS)**. IEEE, 2015. p. 1-4.

[29] PARDUE, G. H. et al. Cement Bond Log - A Study of Cement and casing variables. **Journal of Petroleum Technology**, v. 15, n. 05, p. 545-555, 1963.

[30] WALKER, T. et al. A full-wave display of acoustic signal in cased holes. **Journal of Petroleum Technology**, v. 20, n. 08, p. 811-824, 1968.

[31] ZEMANEK, Joseph et al. The borehole televiewer - A new logging concept for fracture location and other types of borehole inspection. **Journal of Petroleum Technology**, v. 21, n. 06, p. 762-774, 1969.

[32] JUTTEN, J. J. et al. Studies with narrow cement thickness lead to improved CBL in concentric casing. **Journal of petroleum technology**, v. 41, n. 11, p. 1,158-1,192, 1989.

[33] KINOSHITA, T. et al. LWD Sonic tool design for high-quality logs. In: **SEG Technical Program Expanded Abstracts 2010**. Society of Exploration Geophysicists, 2010. p. 513-517.

[34] KHALIFEH, M. et al. Technology Trends in Cement Job Evaluation Using Logging Tools. In: **Abu Dhabi International Petroleum Exhibition & Conference**. Society of Petroleum Engineers, 2017.

[35] **Schlumberger**, 2005. Avaliable at: https://www.slb.com/-/media/files/fe/brochure/memory-slim-cblt-br. Access in 21 March 2019.

[36] **Schlumberger**, 2007. Avaliable at: https://www.slb.com/-/media/files/production/product-sheet/cement-bond-logging-tools-ps. Access in 21 March 2019.

[37] QI, Z. B. et al. A Novel and Efficient Method for Quantitative Cement Logging using a Logging-While-Drilling Acoustic Tool. In: **SPE Kuwait**

Oil & Gas Show and Conference. Society of Petroleum Engineers, 2017.

[38] HALDORSEN, Jakob BU et al. Borehole acoustic waves. **Oilfield review**, v. 18, n. 1, p. 34-43, 2006.

[39] ZHANG, Yuanzhong et al. Review of well logs and petrophysical approaches for shale gas in Sichuan Basin, China. **The Open Petroleum Engineering Journal**, v. 8, n. 1, 2015.

[40] CLOSE, D. et al. The sound of sonic: A historical perspective and introduction to acoustic logging. **CSEG Recorder**, v. 34, n. 5, p. 34-43, 2009.

[41] SAKIYAMA, Naoki et al. Dipole sonic dispersion in poorly cemented and well-cemented cased holes. In: **SEG Technical Program Expanded Abstracts 2017**. Society of Exploration Geophysicists, 2017. p. 880-884.

[42] HAMIDZADEH, H. R.; SAWAYA, N. N. Free vibration of thick multilayer cylinders. **Shock and Vibration**, v. 2, n. 5, p. 393-401, 1995.

[43] PUTMAN, Lloyd et al. A Progress Report on Cement Bond Logging. **Journal of Petroleum Technology**, v. 16, n. 10, p. 1,117-1,120, 1964.

[44] HAYDEN, R. et al. Case studies in evaluation of cement with wireline logs in a deep water environment. In: **SPWLA 52nd Annual Logging Symposium**. Society of Petrophysicists and Well-Log Analysts, 2011.

[45] WANG, Hua; FEHLER, Mike. A cement-bond evaluation method based on the full waveform from a monopole tool. In: **SEG Technical Program Expanded Abstracts 2017**. Society of Exploration Geophysicists, 2017. p. 875-879.

[46] LONGO, Joe et al. Logging-While-Drilling Cement Evaluation, A Case Study from the North Slope Alaska. In: **SPE Annual Technical Conference and Exhibition**. Society of Petroleum Engineers, 2012.

[47] KINOSHITA, Toshihiro et al. Feasibility and challenge of quantitative cement evaluation with LWD sonic. In: **SPE Annual Technical Conference and Exhibition**. Society of Petroleum Engineers, 2013.

[48] BLYTH, Matthew et al. LWD Sonic Cement Logging: Benefits, Applicability, and Novel Uses for Assessing Well Integrity. In: **SPE/IADC Drilling Conference**. Society of Petroleum Engineers, 2013.

[49] LIU, Yang et al. Acoustic guided waves in cylindrical solid-fluid structures: Modeling with a sweeping frequency finite element method and experimental validation. In: **AIP Conference Proceedings**. AIP Publishing LLC, 2017. p. 030004.

[50] GARDNER, D. J. et al. An Experimental Facility for Evaluating Well Barrier Verification Technology. In: **SPE Norway One Day Seminar**. Society of Petroleum Engineers, 2018.

[51] HALDORSEN, Jakob BU et al. Decomposing full-waveform borehole acoustic data with application to data from a North Sea well. **Geophysics**, v. 81, n. 4, p. IM71-IM95, 2016.

[52] ZEROUG, Smaine et al. Sonic and ultrasonic measurement applications for cased oil wells. **Insight-Non-Destructive Testing and Condition Monitoring**, v. 58, n. 8, p. 423-430, 2016.

[53] ZEROUG, Smaine; BOSE, Sandip. Recent advances in the use of acoustics across the frequency spectrum in the oil and gas industry. In: **AIP Conference Proceedings**. AIP Publishing LLC, 2018. p. 020014.

[54] LIU, Yang et al. Understanding acoustic physics in oil and gas wellbores with the presence of ubiquitous geometric eccentricity. In: **AIP Conference Proceedings**. AIP Publishing LLC, 2018. p. 020018.

[55] LEI, Ting; SINHA, Bikash Kumar; ZEROUG, Smaine. **Method for analyzing cement quality in multi-string cased wells using sonic logging.** International Patent Application n. 62/163,336, 24 nov 2016.

[56] LEI, Ting; SINHA, Bikash Kumar; ZEROUG, Smaine. **Method for analyzing cement integrity in cased wells using sonic logging.** International Patent Application n. 62/163,336, 24 nov 2016.

[57] BOSE, Sandip et al. **Method for analyzing cement integrity in casing strings using machine learning**. U.S. Patent Application n. 15/575,024, 31 may 2018.

[58] KHALIFEH, Mahmoud et al. Technology Trends in Cement Job Evaluation Using Logging Tools. In: **Abu Dhabi International Petroleum Exhibition & Conference**. Society of Petroleum Engineers, 2017.

[59] MURRAY, Doug et al. Advanced Logging-While-Drilling Cased Hole Sonic for Real-Time Cement Evaluation and Formation Slowness-Case Studies from West Africa. In: **Abu Dhabi International Petroleum Exhibition & Conference**. Society of Petroleum Engineers, 2018.

[60] GARDNER, D. J. et al. An Experimental Facility for Evaluating Well Barrier Verification Technology. In: **SPE Norway One Day Seminar**. Society of Petroleum Engineers, 2018.

[61] FRISCH, Gary et al. A novel and economical processing technique using conventional bond logs and ultrasonic tools for enhanced cement evaluation. In: **SPWLA 41st Annual Logging Symposium**. Society of Petrophysicists and Well-Log Analysts, 2000.

[62] PISTRE, Vivian et al. Attenuation-Based Quantitative Cement Bond Index with LWD Sonic: A Novel Approach Applicable to all Casing and

Cement Cases. In: **SPE Annual Technical Conference and Exhibition**. Society of Petroleum Engineers, 2014.

[63] QI, Zhang Bin et al. A Novel and Efficient Method for Quantitative Cement Logging using a Logging-While-Drilling Acoustic Tool. In: **SPE Kuwait Oil & Gas Show and Conference**. Society of Petroleum Engineers, 2017.

[64] IZUHARA, W. et al. Full-range quantitative cement bond evaluation with LWD sonic: The right way of approach using a hybrid of amplitude and attenuation. In: **SPE Annual Technical Conference and Exhibition**. Society of Petroleum Engineers, 2017.

[65] KALYANRAMAN, Ram Sunder et al. Making sense of why sometimes logs do not see cement in the annulus. In: **SPE Western Regional Meeting**. Society of Petroleum Engineers, 2017.

[66] JUN, T. A. N. G. et al. Cement bond quality evaluation based on acoustic variable density logging. **Petroleum Exploration and Development**, v. 43, n. 3, p. 514-521, 2016.

[67] **Schlumberger Oilfield Glossary**. Avaliable at: https://www.glossary.oilfield.slb.com/en/Terms/s/stoneley_wave.aspx. Access in 06 fev. 2020

[68] FLORES-MENDEZ, Esteban et al. Rayleigh's, Stoneley's, and Scholte's interface waves in elastic models using a boundary element method. **Journal of applied mathematics**, v. 2012, 2012.

[69] ROSE, Joseph L. **Ultrasonic guided waves in solid media**. Cambridge university press, 2014.

[70] MIKLOWITZ, Julius. **The theory of elastic waves and waveguides**. Elsevier, 2012.

[71] BOERBOOM, A. J. H.; STAUFFER, Douglas B.; MCLAFFERTY, F. W. Ion optics of multipole devices. I. Theory of the dodecapole. **International journal of mass spectrometry and ion processes**, v. 63, n. 1, p. 17-28, 1985.

[72] ACHENBACH, Jan. **Wave propagation in elastic solids**. Elsevier, 2012.

[73] AULD, Bertram Alexander. **Acoustic fields and waves in solids**. Рипол Классик, 1973.

[74] GORDON, John R.; SERWAY, Raymond A. **Study guide with computer exercises to accompany physics for scientists & engineers with modern physics**. Saunders College, 1990.

[75] MATHWORKS. **The MathWorks, Inc**. https: //www.mathworks.com, access in 03 fev. 2020. Avaliable at: <https://www.mathworks.com/help/matlab/ref/fzero.html>.

[76] LI, Zhao; JING, Liwen; MURCH, Ross. Propagation of monopole source excited acoustic waves in a cylindrical high-density polyethylene pipeline. **The Journal of the Acoustical Society of America**, v. 142, n. 6, p. 3564-3579, 2017.

[77] WANG, Hua; FEHLER, Michael. The wavefield of acoustic logging in a cased-hole with a single casing–Part I: a monopole tool. **Geophysical Journal International**, v. 212, n. 1, p. 612-626, 2018.

[78] KINOSHITA, Toshihiro et al. LWD sonic tool design for high-quality logs. In: **SEG Technical Program Expanded Abstracts 2010**. Society of Exploration Geophysicists, 2010. p. 513-517.

[79] **Guided Ultrasonics LTD**. Disponivel em: <https://www.guided-ultrasonics.com/technology/>. Acesso em: 23 fev. 2020.

[80] KINOSHITA, Toshihiro et al. Next generation LWD sonic tool. In: **14th SPWLA Formation Evaluation Symposium of Japan**. 2008.

[81] CORREIA, T. M. et al. Analytical and numerical modeling of through-tubing acoustic logging. **Rio Oil & Gas.** Brazilian Petroleum, Gas and Biofuels Institute - IBP. 2020.

8. Appendix A

Derivative of Hankel and Bessel functions:

The derivations in relation to the radial position, r, of the Bessel and Hankel functions, J_v, $H_v^{(1)}$ and $H_v^{(2)}$ used in the equations in Chapter 3 can be seen in equations A.1, A.2 e A.3.

$$\frac{dH_v^{(1)}(k_j r)}{dr} = k_j \left[H_{v-1}^{(1)}(k_j r) - \frac{v}{k_j r} H_v^{(1)}(k_j r) \right] = k_j e^{ik_j r} \left[h_{v-1}^{(1)}(k_j r) - \frac{v}{k_j r} h_v^{(1)}(k_j r) \right] \quad \text{(A.1)}$$

$$\frac{dH_v^{(2)}(k_j r)}{dr} = k_j \left[H_{v-1}^{(2)}(k_j r) - \frac{v}{k_j r} H_v^{(2)}(k_j r) \right] = k_j e^{-ik_j r} \left[h_{v-1}^{(2)}(k_j r) - \frac{v}{k_j r} h_v^{(2)}(k_j r) \right] \quad \text{(A.2)}$$

$$\frac{dJ_v(k_f r)}{dr} = j_{v-1}(k_f r) - \frac{v}{k_f r} j_v(k_f r) \quad \text{(A.3)}$$

9. Appendix B

Amplitude Matrices $A_\alpha(r)$, $L_\alpha(r)$ e $S_\alpha(r)$

The amplitude matrices $A_\alpha(r)$, $L_\alpha(r)$ e $S_\alpha(r)$ presented and deduced in Chapter 3 has the form presented in equations B.1 to B.6.

$$A_\alpha(r) = \begin{bmatrix} k_L\left(h_{\nu-1}^{(\alpha)}(x) - \frac{\nu}{y}h_\nu^{(\alpha)}(x)\right) & ik_T\frac{\nu}{y}h_\nu^{(\alpha)}(y) & ik_zk_T\left(h_{\nu-1}^{(\alpha)}(y) - \frac{\nu}{y}h_\nu^{(\alpha)}(y)\right) \\ ik_L\frac{\nu}{x}h_\nu^{(\alpha)}(x) & -k_T\left(h_{\nu-1}^{(\alpha)}(y) - \frac{\nu}{y}h_\nu^{(\alpha)}(y)\right) & -k_zk_T\frac{\nu}{y}h_\nu^{(\alpha)}(y) \\ ik_zh_\nu^{(\alpha)}(x) & 0 & k_T^2h_\nu^{(\alpha)}(y) \end{bmatrix} \quad \text{(B.1)}$$

$$L_\alpha(r) = \begin{bmatrix} -2\mu k_L^2 f_\nu^{(\alpha)}(x) - \lambda\frac{\omega^2}{c_L^2}h_\nu^{(\alpha)}(x) & i2\mu k_T^2\frac{\nu}{y}g_\nu^{(\alpha)}(y) & -i2\mu k_zk_T^2f_\nu^{(\alpha)}(y) \\ i2\mu k_L^2\frac{\nu}{x}g_\nu^{(\alpha)}(x) & 2\mu k_T^2\left(f_\nu^{(\alpha)}(y) - \frac{1}{2}h_\nu^{(\alpha)}(y)\right) & -2\mu k_zk_T^2\frac{\nu}{y}g_\nu^{(\alpha)}(y) \\ i2\mu k_zk_L\left(h_{\nu-1}^{(\alpha)}(x) - \frac{\nu}{x}h_\nu^{(\alpha)}(x)\right) & -\mu k_zk_T\frac{\nu}{y}h_\nu^{(\alpha)}(y) & \mu k_T(k_T^2 - k_z^2)\left(h_{\nu-1}^{(\alpha)}(y) - \frac{\nu}{y}h_\nu^{(\alpha)}(y)\right) \end{bmatrix} \quad \text{(B.2)}$$

$$S_\alpha(r) = \begin{bmatrix} i2\mu k_zk_L\left(h_{\nu-1}^{(\alpha)}(x) - \frac{\nu}{x}h_\nu^{(\alpha)}(x)\right) & -\mu k_zk_T\frac{\nu}{y}h_\nu^{(\alpha)}(y) & \mu k_T(k_T^2 - k_z^2)\left(h_{\nu-1}^{(\alpha)}(y) - \frac{\nu}{y}h_\nu^{(\alpha)}(y)\right) \\ -2\mu k_zk_L\frac{\nu}{x}h_\nu^{(\alpha)}(x) & -i\mu k_zk_T(h_{\nu-1}^{(\alpha)}(y) - \frac{\nu}{y}h_\nu^{(\alpha)}(y)) & \mu k_T(k_T^2 - k_z^2)\frac{\nu}{y}h_\nu^{(\alpha)}(y) \\ -(2\mu k_z^2 + \lambda\frac{\omega^2}{c_L^2})h_\nu^{(\alpha)}(x) & -i\lambda\frac{\nu}{r}\left(h_{\nu-1}^{(\alpha)}(y) - \frac{\nu}{y}h_\nu^{(\alpha)}(y)\right) & (i2\mu k_zk_T^2)h_\nu^{(\alpha)}(y) \end{bmatrix} \quad \text{(B.3)}$$

Where x e y are defined by:

$$x = k_Lr \quad e \quad y = k_Tr \quad \text{(B.4)}$$

and the functions f e g are described as:

$$f_\nu^{(\alpha)}(\xi) = \frac{1}{\xi}h_{\nu-1}^{(\alpha)}(\xi) + \left(1 - \frac{\nu(1+\nu)}{\xi^2}\right)h_\nu^{(\alpha)}(\xi) \quad \text{(B.5)}$$

$$g_\nu^{(\alpha)}(\xi) = h_{\nu-1}^{(\alpha)}(\xi) - \frac{1+\nu}{\xi}h_\nu^{(\alpha)}(\xi) \quad \text{(B.6)}$$